

# Helfrich-Hurault elastic instabilities driven by geometrical frustration

Christophe Blanc 

*UMR CNRS 5221, Laboratoire Charles Coulomb, Université Montpellier, place Eugène Bataillon, 34095 Montpellier, Cedex 5, France*

Guillaume Durey

*School of Engineering, Brown University, Providence, Rhode Island 02912, USA and UMR CNRS 7083 Gulliver, ESPCI Paris, Université PSL, 75005 Paris, France*

Randall D. Kamien 

*Department of Physics and Astronomy, University of Pennsylvania, Philadelphia, Pennsylvania 19104, USA*

Teresa Lopez-Leon 

*UMR CNRS 7083 Gulliver, ESPCI Paris, Université PSL, 75005 Paris, France*

Maxim O. Lavrentovich\*

*Department of Physics and Astronomy, University of Tennessee, Knoxville, Tennessee 37996-1200, USA*

Lisa Tran †

*Department of Physics, Soft Condensed Matter and Biophysics, Debye Institute for Nanomaterials Science, Utrecht University, Utrecht 3584 CC, Netherlands*

 (published 31 March 2023)

The Helfrich-Hurault (HH) elastic instability is a well-known mechanism behind patterns that form as a result of strain upon liquid crystal systems with periodic ground states. In the HH model, layered structures undulate and buckle in response to local, geometric incompatibilities in order to maintain the preferred layer spacing. Classic HH systems include cholesteric liquid crystals under electromagnetic field distortions and smectic liquid crystals under mechanical strains, where both materials are confined between rigid substrates. However, richer phenomena are observed when undulation instabilities occur in the presence of deformable interfaces and variable boundary conditions. Understanding how the HH instability is affected by deformable surfaces is imperative for applying the instability to a broader range of materials. In this review, the HH mechanism is reexamined and special focus is given to how the boundary conditions influence the response of lamellar systems to geometrical frustration. Lamellar liquid crystals confined within a spherical shell geometry are used as the model system. Made possible by the relatively recent advances in microfluidics within the past 15 years, liquid crystal shells are composed entirely of fluid interfaces and have boundary conditions that can be dynamically controlled at will. Past and recent work that exemplifies how topological constraints, molecular anchoring conditions, and boundary curvature can trigger the HH mechanism in liquid crystals with periodic ground states is examined. The review ends by identifying similar phenomena across a wide variety of materials, both biological and synthetic. The fact that the HH mechanism is a generic and often overlooked response of periodic materials to geometrical frustration is highlighted.

DOI: [10.1103/RevModPhys.95.015004](https://doi.org/10.1103/RevModPhys.95.015004)

\*mlavrent@utk.edu

†l.tran@uu.nl

## CONTENTS

I. Introduction	2
II. The Dramatis Personae	4
III. The Classic Helfrich-Hurault Instability	5
A. Cholesteric layer distortions from electric and magnetic fields	5
1. Original model	6
2. Further theoretical refinements and experiments	6
B. Mechanical layer strain in smectics	7
1. Mechanically induced Helfrich-Hurault effect	8
2. The role of dislocations and disclinations	8
IV. Liquid Crystal Shells	9
V. Cholesteric Shells	10
A. Planar cholesteric shells	10
B. Homeotropic cholesteric shells	13
C. Anchoring transitions	15
VI. Smectic Shells	17
A. Planar smectic shells in experiments	17
B. Strain from boundary curvature	18
C. Cylindrical smectic shells	20
D. Spherical smectic shells	21
VII. Other Causes of the HH Mechanism	23
VIII. Helfrich-Hurault Mechanism:	
Here, There, and Everywhere	24
A. Twist-bend nematic phases	24
B. Lyotropic liquid crystals	26
C. Diblock copolymers, polymer bundles, and sheets	27
D. Columnar liquid crystals	29
E. Biological materials	30
F. Magnetic systems	31
IX. Conclusion	32
Acknowledgments	33
Appendix: Spherical Smectic Shells: Further Details	33
1. Construction of the layers	33
2. Extension of the smectic texture along the azimuthal direction	33
References	35

## I. INTRODUCTION

Subjected to shear, solids strain but fluids flow: what else can happen? Between solid and liquid lie the liquid crystalline phases of matter: like a crystal, they transmit torque and shear stresses but only in some directions and geometries. For instance, the long-range orientational order of a nematic liquid crystal, a phase where the rodlike constituents tend to point in the same direction (the director), implies that if a rod is rotated away from its preferred direction in one region, its surroundings will rotate with it. Nematics do not have translational order, so they do not support shear stresses. However, smectic and cholesteric liquid crystals do. Smectics break translational symmetry by having the rodlike molecules sort into layers, resulting in a density modulation in one direction. Cholesterics form “pseudolayers,” maintaining a constant density throughout the material, but break translational symmetry due to a helical twisting of the director. The thickness of a cholesteric pseudolayer is defined by a rotation of the molecules by  $\pi$ , as represented in Fig. 1(a). Both smectics and cholesterics have one-dimensional periodicity in three-dimensional samples, like a messy stack of cards. When extensional shear is applied to a structure with a preferred

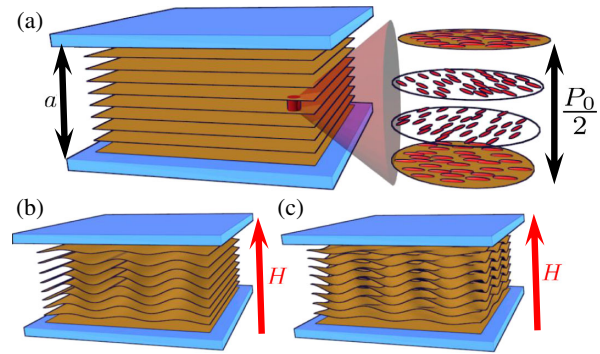


FIG. 1. (a) Schematic of the classic Helfrich-Hurault instability in a cholesteric liquid crystal. The mesophase is confined between solid substrates with planar anchoring and can be described as a lamellar system of period  $P_0/2$ . Undulation in the periodic layers of the cholesteric along (b) a single or (c) two perpendicular directions develops under an applied magnetic field ( $H$ ) of sufficient magnitude.

layer spacing, the layers can undulate in order to maintain their preferred distance. This sort of response was studied by Helfrich and Hurault in the early 1970s within the context of electromagnetic instabilities, depicted in Figs. 1(b) and 1(c) for a cholesteric (Helfrich, 1971; Hurault, 1973). Today we refer to all of these undulating responses in layered systems as the Helfrich-Hurault (HH) mechanism.

The undulatory deformations of the HH instability are similar in spirit to the martensitic patterns seen in crystals, where changes in a crystal structure require accompanying volumetric changes (Ball, James, and Smith, 1992). Indeed, smectic liquid crystals have even been described as the “weirdest martensite” (Liarte *et al.*, 2016). Within a smectic, layers can break and rejoin, creating topological defects (localized regions of disorder) such as dislocations and disclinations. In general, topological defects result from system *frustration* that can arise from either local or global geometrical effects.

For example, Frank-Kasper phases, which catalog the numerous possible arrangements of atoms in complex alloys, are a renowned, historical illustration of structure from geometrical frustration (Frank and Kasper, 1958; Kleman and Sadoc, 1979; Sadoc and Mosseri, 1999; Mosseri, 2008). The most locally compact packing of four rigid, identical spheres is tetrahedral, in which each corner of the tetrahedron represents the center of each sphere. However, imperfections, i.e., defects, occur when the tetrahedron is the unit structure for tiling space. Geometrical frustration in Frank-Kasper phases arises because tetrahedrons cannot fill space completely without distortion. Their symmetry conflicts with a translation symmetric tessellation since the dihedral angle of a tetrahedron is not commensurable with  $2\pi$  (Kleman and Sadoc, 1979; Kleman, 1989; Sadoc and Mosseri, 1999). Defects are necessarily present in the system because the packing is “limited” by the shape of the packing unit. Although tetrahedrons are unable to fill space, the tetrahedral packing actually has higher local densities and greater vibrational entropy than face-centered-cubic or hexagonal close packings do. This enables a wide array of possible configurations that gives the packings of Frank-Kasper phases freedom to deform in order to accommodate neighboring atoms

(Kleman and Sadoc, 1979; Kleman, 1989). Frank-Kasper phases demonstrate not only that defects are often necessary to stabilize systems but that phases can also be constructed from geometrical incompatibilities. The regular network of disclinations in Frank-Kasper phases requires only the tiling of polytetrahedra to be constructed.

It is not a coincidence that Sir F. Charles Frank is the same “Frank” of both Frank-Kasper phases and the Frank free energy density of a liquid crystal: underlying both formulations is the importance of geometry in the description of material properties. Classic examples of geometrical frustration in liquid crystals are blue phases: states that emerge when it is favorable to introduce defects to minimize the chiral elastic energy of the bulk (Saupe, 1969; Marcus, 1981). As is the case for the network of defects in Frank-Kasper phases, the defect networks in blue phases emerge from geometrical frustration (Mosseri, 2008). Similar to how the imperfect packing of pentagons on a plane can be made perfect when the plane is curved into a spherical topology, the disclination line networks of blue phases are removed from blue phases in the curved space of  $S^3$  (the three-sphere). The defects in blue phases can be thought of as the consequence of “folding out” the three-sphere onto Euclidean space (Sethna, Wright, and Mermin, 1983). The conflict between local and global order, as demonstrated by Frank-Kasper and blue phases, is a signature of geometrical frustration. For a thorough review of blue phases, see Wright and Mermin (1989).

In these and countless other systems, local geometrical frustration is often accompanied by global geometrical, i.e., topological, frustration, depending on the global structure of the phase. Using the Gauss-Bonnet theorem, it is possible to locally measure the Gaussian curvature of a patch of surface simply by studying the curvature of closed loops. If you can measure the curvature everywhere, it is then possible to deduce the global topology of the surface, but only if the boundary conditions are precisely defined. In some cases, the boundary can be interpreted as yet another defect at infinity. Setting aside considerations of the boundaries for now, the important issue here is that local geometrical frustration causes problems in your neighborhood: even if Earth were a hemisphere that ended with a precipice at the equator, we would still not be able to draw perfect polygons on it. One of the following situations would have to occur: the angles would not be quite right, the edge lengths would be unequal, or they would not lie directly against Earth’s surface. This is geometrical frustration: a fundamental incompatibility between one set of shapes (the polygons) and the others (Earth’s surface). Topological frustration needs to be solved somewhere; geometrical frustration has to be solved everywhere.

Liquid crystals are the ideal systems to differentiate local from global geometrical frustration. Most liquid crystal systems have open boundaries and the notion of global topology is moot: defects can end on the interfaces between phases or at the sample wall, and they can transform from bulk defects to boundary defects. The frustration can come about because the geometric parameters do not match, the shapes do not match (square peg, round hole), or, as in the blue phase, there is a local geometry (double twist) that cannot be extended into the entire volume. The softness of liquid

crystals, the ability to control and monitor their boundary conditions, and the relatively straightforward method of real-space detection of defects allow us to explore both local and global geometrical frustration.

As pointed out by Anderson, there are many possible ordered phases associated with the symmetry breaking of an isotropic fluid phase, inducing a particular rigidity in the material as characterized by an elastic energy that is written in terms of gradients of an order parameter. The smectic and cholesteric considered here are particularly complex ordered phases (Anderson, 2005), as they contain both a nematic order and a rigidity associated with the bending and compression of layers or pseudolayers (but are otherwise free to slide among themselves). The corresponding elastic energies are discussed in detail in Sec. II. We also consider these lamellar liquid crystals in complex confinements, where geometrical frustration is often relieved through the HH mechanism. This mechanism is specific to layered systems, as it involves a trade-off between the bending and compression of the layers under some applied perturbation. This phenomenon is not possible in a conventional crystal, which would always involve the breaking of bonds. To apply the HH instability beyond the classical systems, we also give additional scrutiny to boundary conditions.

In the first studies by Helfrich and Hurault in the 1970s, the HH instability was examined in lamellar liquid crystals confined between two solid substrates, with undulation in the layers of liquid crystal induced by electromagnetic fields (Helfrich, 1971; Hurault, 1973). In the 1990s, the development of polymer dispersed liquid crystals (Doane, 1990, 1991), with applications in displays and privacy windows, accelerated fundamental investigations of static configurations in more complex geometries, such as within droplets and pores (Crawford and Zumer, 1996; O. D. Lavrentovich, 1998). With the advance of lithographic techniques in the late 1990s and early 2000s (Xia and Whitesides, 1998), the confining surfaces of liquid crystals could be further shaped into more elaborate, three-dimensional architectures, thereby advancing alignment patterning (Gupta and Abbott, 1997; Lee and Clark, 2001) and responsive liquid crystal technologies (Bukusoglu *et al.*, 2016). Emerging sensing applications also require exposure of the liquid crystal to other fluid phases, resulting in systems with deformable interfaces, further increasing the complexity of boundary conditions (Carlton *et al.*, 2013). The investigation of liquid crystals in more intricate geometries in recent decades has led to a resurgence of interest in the HH instability as more researchers have applied these confinements to lamellar liquid crystal systems.

Many contemporary liquid crystal studies explore the ordering of living matter as well. These include systems beyond those of the classic HH instability that undulate to relieve geometrical frustration, including in the morphogenesis of biological liquid crystals. Living liquid crystals that exhibit undulating layers are pervasive in nature, seen within a wide array of biological materials ranging from plant cell walls to arthropod cuticles (Bouligand, 1972b; Roland, Reis, and Vian, 1992; Giraud-Guille, 1998; Sharma *et al.*, 2009; Rey, 2010; Mitov, 2017; Beliaev *et al.*, 2021). These systems not only are dynamic but also typically have deformable boundaries at fluid interfaces. Elucidating the coupling between deformable boundaries and bulk deformations is

then necessary to apply the HH mechanism to a broader class of materials.

To isolate the effects of a fluid boundary on liquid crystals within the laboratory, a synthetic system must have both deformable interfaces and tunable thicknesses to control the balance between bulk and surface forces. An experimental system ideal for this purpose is a liquid crystal shell, which was made possible in 2005 by the seminal work of [Utada \*et al.\* \(2005\)](#) on microfluidics. As first demonstrated by [Fernandez-Nieves \*et al.\* \(2007\)](#), who used a liquid crystal as the middle phase in the production of water-in-liquid-crystal-in-water double emulsions, the liquid crystal can be shaped into a spherical shell, making the system freestanding and stable. With simple adjustments of flow rates and/or the addition of solutes in the surrounding aqueous phases, both the thickness of the liquid crystal shell and the molecular anchoring at the shell interfaces can be dynamically varied at will. Liquid crystal shells are then model systems for probing the role of curved, deformable boundaries in both triggering the HH instability and stabilizing the resultant defect structures.

The purpose of this review is twofold. First, the HH instability is detailed as a mechanism of pattern formation that results from frustration in lamellar liquid crystals, taking special care to distinguish local versus global (topological) geometrical frustration. Second, not only is the HH instability historically reviewed, but recent work on cholesteric and smectic liquid crystal shells is presented to illustrate the mechanisms through which deformable boundaries can influence and trigger layer undulations.

In Sec. II, we review the elasticity of liquid crystals. In Sec. III, we examine the history of the HH instability and detail the classic HH systems, where lamellar liquid crystals are confined between solid substrates. In Sec. IV, we consider liquid crystals with deformable interfaces and describe our model system: the liquid crystal shell. We then characterize the HH instability in cholesteric shells in Sec. V, where undulations can arise due to global geometrical (i.e., topological) frustration and surface anchoring. We then progress to smectic shells in Sec. VI, where the HH instability is triggered by local geometrical frustration due to boundary curvature. We end by identifying the HH instability across a wide range of elastic materials, both synthetic and biological.

## II. THE DRAMATIS PERSONAE

Before plunging in, we pause to outline liquid crystal elasticity. [de Gennes and Prost \(1993\)](#), [Chaikin and Lubensky \(1995\)](#), and [Kleman and O. D. Lavrentovich \(2004\)](#) thoroughly covered this, but here we offer a highly abridged review. The simplest of the liquid crystalline phases is the nematic one. In this phase, a preferred, “long” axis of the molecules aligns along a local direction, represented by a unit vector  $\mathbf{n}$ . At first glance this would appear to be equivalent to a magnet where  $\mathbf{n}$  would take the place of the local spin  $\mathbf{m}$ , but the nematic phase has an additional symmetry:  $\mathbf{n}$  and  $-\mathbf{n}$  represent the same structure (the nematic is a line field, not a vector field). According to [Frank \(1958\)](#), distortions away from the uniform nematic phase are measured through four geometric quantities that are invariant under the nematic

symmetry:  $\vec{S} = \mathbf{n}(\nabla \cdot \mathbf{n})$ ,  $T = \mathbf{n} \cdot (\nabla \times \mathbf{n})$ ,  $\vec{B} = (\mathbf{n} \cdot \nabla) \mathbf{n}$ , and  $G = \nabla \cdot (\vec{B} - \vec{S})$ : splay, twist, bend, and saddle splay, respectively. The Frank free energy density is a rotationally invariant expression in terms of these two vectors ( $\vec{S}$  and  $\vec{B}$ ), the pseudoscalar ( $T$ ), and the scalar ( $G$ ):

$$f = \frac{1}{2}K_1\vec{S}^2 + \frac{1}{2}K_2(T + q_0)^2 + \frac{1}{2}K_3\vec{B}^2 + K_24G. \quad (1)$$

We note that  $\vec{S} \cdot \vec{B} = 0$ , so there are no cross terms. This free energy exhausts all the rotationally invariant groupings of terms up to quadratic order in single gradients of  $\mathbf{n}$ . The four elastic constants inherit their names from the expressions they multiply; for instance,  $K_2$  is the “twist” elastic constant. Stability implies that  $K_1$ ,  $K_2$ , and  $K_3$  are positive. Finally, because  $T$  is a pseudoscalar,  $q_0$  must be as well, and the existence of a pseudoscalar quantity would imply that the material is chiral. To rationalize the names of these distortions, one can evaluate the splay for the two-dimensional texture  $\mathbf{n} = \hat{\rho} (\vec{S} = \hat{\rho}/\rho)$  and evaluate the bend for the two-dimensional texture  $\mathbf{n} = \hat{\theta} (\vec{B} = -\hat{\theta}/\rho)$ , where  $\rho$  and  $\theta$  are the standard polar coordinates. Both twist and saddle splay measure three-dimensional textures: if  $\mathbf{n} = [\cos(qz), \sin(qz), 0]$ , then  $T = -q$ , while if  $\mathbf{n} = [x, -y, 1]/\sqrt{1+x^2+y^2}$ , then  $G = 2/(1+x^2+y^2)^2$ . The result for  $G$  can be understood by viewing  $\mathbf{n}$  as the unit normal to the saddle surfaces of the surface family  $z = (1/2)(y^2 - x^2)$ , and then  $G$  is the negative of the Gaussian curvature at each point ([Kamien, 2002](#)).

In the absence of boundaries, the saddle splay does not contribute to the energy (via Stokes’s theorem). When  $q_0 = 0$ , a ground state is  $\mathbf{n} = [0, 0, 1]$ , while if  $q_0 \neq 0$ , then it is straightforward to verify that  $\mathbf{n}_c = [\cos(q_0z), \sin(q_0z), 0]$  is a ground state. We call this helically twisting ground state the *cholesteric* or the chiral nematic, and in this case it has a pitch axis along  $\hat{z}$ . By rotational invariance, these ground states can be rotated in space, leading to an entire manifold of degenerate ground states. The cholesteric ground state can then be viewed in terms of pseudolayers of constant orientation. Moreover, since a global rotation of  $\mathbf{n}$  around the  $z$  axis by an angle  $\phi$  cannot change the energy, we know that at long length scales this global symmetry is promoted to a Goldstone mode so that small ground-state fluctuations can be viewed as deformations of the pseudolayers. The HH effect distorts these pseudolayers when the preferred spacing  $\pi/q_0$  differs from a spacing imposed by fields or boundary conditions.

In the following, we also discuss smectic phases. In the smectic phase, translational symmetry is broken and the molecules arrange themselves into actual layers, creating a one-dimensional density wave with the ground state consisting of a set of uniformly spaced, flat layers. These layers generate a field of unit layer normals  $\mathbf{N}$ . Since the normals are defined only up to sign, the symmetry of  $\mathbf{N}$  is precisely that of the previously discussed nematic director. We can thus create an energy in complete analogy with the Frank free energy, where we substitute  $\mathbf{n}$  with  $\mathbf{N}$  in the just-completed discussion. However, note that twist necessarily vanishes if  $\mathbf{N}$  is normal to a surface from the Frobenius integrability condition ([Capasso, 2018](#)). Yet there must also be an energy

penalty for deformations away from the preferred spacing. To measure this, we introduce a phonon field  $u(x, y, z)$  that measures the deviation from uniformly spaced layers.<sup>1</sup> Because the sign of  $u$  has the same  $u \rightarrow -u$  ambiguity as the vector  $\mathbf{n}$ , we measure deviations of  $u$  here along  $N$  and define the strain as  $e = N \cdot \nabla u$ , which is invariant under  $(N, u) \rightarrow -(N, u)$ . The free energy density is

$$f = \frac{1}{2} B e^2 + \frac{1}{2} \bar{K}_1 \bar{S}_{sm}^2 + \frac{1}{2} \bar{K}_3 \bar{B}_{sm}^2 + \bar{K}_{24} G_{sm}, \quad (2)$$

where the subscript  $sm$  refers to the quantities with  $\mathbf{n}$  replaced by  $N$  and where  $B$  is known as the bulk modulus (and should not be confused with the bend vector  $\vec{B}$ ). Since we can parametrize the smectic layers as level sets of  $\phi = z - u(x, y, z)$ ,  $N = \nabla \phi / |\nabla \phi|$  can be calculated from  $u$ . For instance,  $N \approx (-\partial_x u, -\partial_y u, 1)$  to lowest order in gradients of  $u$ . Because the phase is composed of nematogenic molecules, we must also include the Frank free energy for the nematic director and note that there is a coupling between  $N$  and  $\mathbf{n}$ . In the smectic-*A* phase,  $\mathbf{n}$  prefers to align with  $N$ , while in the smectic-*C* phase the layer normal and director prefer a fixed, nonzero angle between them. This leads to yet another directorlike field, which is the component of  $\mathbf{n}$  perpendicular to  $N$ : the  $\mathbf{c}$  director.

An examination of Eqs. (1) and (2) reveals that the deformations of the smectic-*A* layers and the cholesteric pseudolayers are controlled by the same free energy density (Kleman and Parodi, 1975; Oswald and Pieranski, 2005),

$$f_e = \frac{B}{2} \left( 1 - \frac{1}{|\nabla \phi|} \right)^2 + \frac{K}{2} (\nabla \cdot N)^2, \quad (3)$$

where the first term accounts for relative dilation of the layers and the second term is the curvature energy of the layers. The values of the effective elastic moduli  $B$  and  $K$  will depend on the particular system, as discussed in more detail in Secs. III.A and III.B. In the long distance limit, several layers away from the boundary, where the bulk layers are nearly flat and planar, this free energy reduces to

$$f_e = \frac{B}{2} \left( \frac{\partial u}{\partial z} \right)^2 + \frac{K}{2} \left( \frac{\partial^2 u}{\partial x^2} + \frac{\partial^2 u}{\partial y^2} \right)^2, \quad (4)$$

where the average layer normal (or the pitch axis) is along  $\hat{z}$ . Note that in the smectic-*A* case the  $\bar{K}_3$  and  $\bar{K}_{24}$  contributions are of a higher degree in a gradient expansion and are, in this simplest case, neglected. In the case of the cholesteric, we would replace  $u$  with the deviation of the angle of the director field in the plane perpendicular to the pitch axis. This basic free energy is the starting point for this review. Note that this elastic free energy density applies to any system with one-dimensional, periodic ground states. Without loss of generality, the periodicity is along the  $\hat{z}$  direction, and we can write the density (or pseudodensity) as

$$\rho(\mathbf{x}) = \rho_0 + \rho_1 \cos\{q[z - u(\mathbf{x})]\}, \quad (5)$$

where  $q$  is the ground-state wave vector magnitude. The first term in Eq. (4) measures the energy penalty for changing the periodicity, while the second term measures the energy cost of bending the “layers.” We now dive into the history of the HH instability.

### III. THE CLASSIC HELFRICH-HURAUULT INSTABILITY

As evident from the success of liquid crystals in the display industry, liquid crystal technology relies upon the material’s interaction with external fields. Recall that the simplest liquid crystalline phase, the nematic, is characterized by long-range order of the orientation of anisotropic molecules with one long axis and two equivalent “short” axes.<sup>2</sup> These axes are geometric, dielectric, and optical, leading to birefringent optics. The dielectric anisotropy of liquid crystals enables their manipulation with electromagnetic fields, and their birefringence renders optically detectable responses. Systematic investigations of liquid crystals under these external fields were of special interest in the 1960s, the decade when liquid crystal displays were first conceptually conceived, and regular textures were soon experimentally observed and identified. Some patterns were related to flows or other dynamical aspects, such as electrohydrodynamic convection in nematics (Helfrich, 1969), but others, found especially in layered or quasilayered systems, remained static and exhibited well-defined wavelengths that resulted from direct competition between liquid crystal elasticity and its anisotropic, electromagnetic properties.

The possibility of such an instability with well-defined wavelength was predicted by Helfrich in the case of cholesterics, where the molecules have a tendency to twist in a helical fashion, with the pitch defined as the distance required for a  $2\pi$  rotation of the molecule along the pitch axis (Fig. 1) (Helfrich, 1970). Note again that cholesterics have a periodic ground state, with no density modulation but rather a modulation in orientation, and consequently one also in the dielectric tensor. Because of this, the periodicity in the system is often referred to as pseudolayers. Experimental data for the instability in cholesterics emerged almost simultaneously in the early 1970s (Helfrich, 1970) and were followed by two successive theoretical papers, first by Helfrich in 1971 and then a refinement by Hurault in 1973 (Helfrich, 1971; Hurault, 1973). Initially associated with the cholesteric phase, as depicted in Fig. 1, the HH buckling instability was rapidly identified as a generic mechanism to relieve stresses and strains due to external stimuli in lamellar, periodic systems.

#### A. Cholesteric layer distortions from electric and magnetic fields

The HH instability was first observed in cholesteric liquid crystal cells (Gerritsma and Van Zanten, 1971a, 1971b) with strong planar anchoring, where the director  $\mathbf{n}$  of the molecules

<sup>1</sup>Unlike a crystal, however,  $u(x, y, z)$  only has one component reflecting the one-dimensional density wave.

<sup>2</sup>These are the so-called calamitic nematics. Discotic phases are also nematic, though they have one short axis and two equivalent long axes.

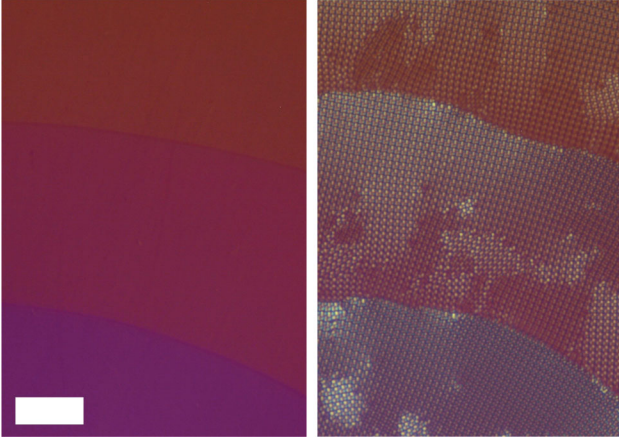


FIG. 2. Left image: planar texture of a cholesteric phase obtained from mixing 4'-pentyl-4-biphenyl-carbonitrile (5CB) and cholesteryl oleate in a planar-aligned cell. Grandjean zones correspond to a slight gradient of thickness resulting in a discrete change in the number of  $\pi$  rotations of the director. Right image: under large enough ac voltages ( $\sim 1$  kHz), typical square-grid patterns are observed. Here a 9 V electric field is applied across a 20- $\mu\text{m}$ -thick cell. Images are captured with polarizing optical microscopy under slightly uncrossed polarizers. The scale bar is 50  $\mu\text{m}$ .

is aligned tangent to the top and bottom walls. In this geometry, the cholesteric pitch axis perpendicular to the nematic director  $\mathbf{n}$  and along which the director twists has a uniform orientation perpendicular to the parallel walls. The application of an electric field (Gerritsma and Van Zanten, 1971b; Rondelez and Arnould, 1971) or a magnetic field (Rondelez and Hulin, 1972; Scheffer, 1972) parallel to this helix gives rise to square-grid patterns above a certain threshold value (Fig. 2). Here the driving force of the instability is a gain in dielectric or diamagnetic energy when the cholesteric helix begins to distort. In this geometry, the HH instability occurs only in materials with positive (nematic) diamagnetic susceptibility anisotropy  $\chi_a$  or dielectric anisotropy  $\epsilon_a$ , so the director aligns along the field, antagonizing the helix. The case of ac electric fields is, however, more complex since the presence of conductivity and space charges can also lead to frequency-dependent instabilities for both signs of dielectric anisotropy  $\epsilon_a$  (Rondelez, Arnould, and Gerritsma, 1972; Hurault, 1973).

### 1. Original model

In the magnetic case, the threshold and the wavelength of the patterns can be easily computed at the onset of undulations with two assumptions: (1) the distortions are small and (2) the instability wavelength is much larger than the cell thickness  $a$ , which is itself much larger than the cholesteric pitch  $P_0 = 2\pi/q_0$  (Ishikawa and O. D. Lavrentovich, 2001a). Recall that the continuous twist of the director field is described as a pseudolayered structure of  $P_0/2$  periodicity [Fig. 1(a)]. In the Lubensky–de Gennes coarse-grained approach, the elastic free energy density  $f_e$  of a distortion from the planar texture is related to the displacement  $u(\mathbf{x})$  of the pseudolayers along the  $z$  axis corresponding to the direction of the initial helix

(Brand and Pleiner, 1981; de Gennes and Prost, 1993), yielding a free energy density of the same form as Eq. (4), but now with  $K$  rewritten as  $\bar{K} = 3K_3/8$  and  $B$  rewritten as  $\bar{B} = K_2q_0^2$ .  $\bar{K}$  and  $\bar{B}$  are the effective elastic moduli related to the Frank-Oseen elastic constants of twist  $K_2$  and bend  $K_3$  of Eq. (1). In the cholesteric, a distortion  $u(\mathbf{x})$  leads to a tilt of the pitch axis  $\mathbf{N}$  from  $\hat{z}$ . To lowest order we get  $\tan^2\theta = (\nabla_{\perp}u)^2$ , where  $\nabla_{\perp} = \hat{x}\partial_x + \hat{y}\partial_y$ . For small distortions we have

$$\theta \approx \sqrt{\left(\frac{\partial u}{\partial x}\right)^2 + \left(\frac{\partial u}{\partial y}\right)^2}, \quad (6)$$

with a concomitant change in the magnetic energy density of

$$f_m = -\frac{1}{2}\mu_0\bar{\chi}_a H^2\theta^2, \quad (7)$$

where  $\mu_0$  is the vacuum permeability and  $\bar{\chi}_a = \chi_a/2$  accounts for the continuous twist of the director over a pitch.

The HH model considers a simple undulation pattern along one direction ( $\hat{x}$  here) and is compatible with infinitely strong anchoring at the bounding surfaces  $z = \pm a/2$  [Fig. 1(b)]:

$$u(\mathbf{x}) = u_0 \cos\left(\frac{\pi z}{a}\right) \sin(qx). \quad (8)$$

The total free energy of such an undulation in a cell of volume  $V$  can be computed from Eqs. (4) and (6)–(8),

$$F_t = \left(\frac{\bar{B}\pi^2}{a^2} + \bar{K}q^4 - \mu_0\bar{\chi}_a H^2 q^2\right) \frac{V}{8} u_0^2. \quad (9)$$

At low fields, undulations are unfavored. An instability occurs for a critical field  $H_c$  when the sign of the minimum of  $F_t$  (with respect to  $q$ ) changes from positive to negative:

$$H_c^2 = \frac{2\sqrt{\bar{K}\bar{B}}\pi}{a\mu_0\bar{\chi}_a} = \frac{\sqrt{6K_2K_3}\pi q_0}{a\mu_0\chi_a}. \quad (10)$$

This first-order approach also allows us to compute the wave vector amplitude  $q_c$  at the threshold:

$$q_c^2 = \frac{\pi}{a} \sqrt{\frac{\bar{B}}{\bar{K}}} = \frac{2\pi q_0}{a} \sqrt{\frac{2K_2}{3K_3}}. \quad (11)$$

The main predictions of the wavelengths and the threshold of the HH model were satisfactorily checked experimentally soon after the development of the theory. However, the original model was found to be limited for some experimental situations, and thus was amended incrementally over time. In the following, we show that this basic free energy balance is recapitulated in layered systems subject to stresses that are both internal and external. In so doing, we gather all of these effects under the Helfrich-Hurault umbrella.

### 2. Further theoretical refinements and experiments

For simplicity, we have reported the initial approach of Helfrich and Hurault, which was based on a simple one-dimensional distortion of the layers. Even if this theory gave

the correct threshold field and instability wavelength, it did not describe the geometry of the instability. The early experimental examinations of the HH phenomenon showed that undulations along a single direction were rarely observed at the threshold, except in large pitch systems, where  $a \sim P_0$  (Hervet, Hurault, and Rondelez, 1973). In most cases (large  $a/P_0$  ratios) square-grid patterns are observed at the onset; see Fig. 2. Delrieu (1974) generalized the HH theory and considered a 2D Fourier expansion of the displacement  $u$  of the layers. They showed that the square lattice sketched in Fig. 1(c) was indeed the periodic 2D structure of lowest energy at the onset for a field perpendicular to the layers. They nevertheless also showed that the formation of one-dimensional stripe patterns at the onset was possible in other geometries. For instance, when the applied field is tilted, one direction of the plane can be energetically favored over the other. In this case, the square lattices appear above a second threshold field.

The model outlined in Sec. III.A.1 is also too rough to describe the evolution of the patterns above  $H_c$ . The total free energy scales as the square of the undulation amplitude  $u_0^2$  in Eq. (9). Therefore, it is necessary to compute  $F_t$  with higher-order terms included in the strain to get a consistent undulation amplitude. These terms provide a better description of the compression term in Eq. (4), accounting for the tilt of the pseudolayers. In terms of the phase field, a rotationally invariant strain is  $e = [1 - (\nabla\phi)^2]/2$  (Kamien *et al.*, 2009). In two dimensions this gives to next-to-leading order

$$f_e = \frac{\bar{B}}{2} \left[ \frac{\partial u}{\partial z} - \frac{1}{2} \left( \frac{\partial u}{\partial x} \right)^2 \right]^2 + \frac{\bar{K}}{2} \left( \frac{\partial^2 u}{\partial x^2} \right)^2, \quad (12)$$

which yields, after minimization of the free energy  $F_t$ ,

$$u_0 = \frac{8}{3} \sqrt{\frac{\bar{K}}{\bar{B}} \left( \frac{H^2}{H_c^2} - 1 \right)}. \quad (13)$$

The exact shape of the experimental patterns was not scrutinized in the 1970s because of a lack of appropriate experimental techniques. It was only later, in a different cell geometry, that Ishikawa and O. D. Lavrentovich (2001b) closely examined an undulation pattern developing along a single direction. The two-dimensional system consisted of cholesteric stripes formed in a cell with homeotropic (perpendicular) anchoring of the liquid crystal director, generating a fingerprint texture. The periodic stripes were horizontally sandwiched between parallel spacers in the cell, and a magnetic field was applied in the plane of the cell, perpendicular to the stripes, allowing direct examination of the patterns above  $H_c$ . They emphasized the neglected role of anchoring on the bounding substrates, where distortions could still be observed. A finite anchoring yields amplitude undulations much larger than the value predicted by Eq. (13), as well as a reduced threshold value. This result was later confirmed for the square lattice of the original geometry by Senyuk, Smalyukh, and O. D. Lavrentovich (2006), who used fluorescence confocal polarizing microscopy (FCPM) to image in three-dimensions the distorted pseudolayers under

an electric field. We expound upon the influence of anchoring and other surface energies on the HH mechanism when we discuss liquid crystal shells.

The powerful FCPM technique was also employed to analyze the evolution of the patterns generated by the HH instability in detail and with increasing fields. It confirmed that the hypothesis of a single Fourier mode in the plane was valid only in a small range above the threshold. When the field increased, the sinusoidal profile of the square-grid pattern gradually changed to a sawtooth one, as predicted by Singer (1993, 2000). Senyuk, Smalyukh, and O. D. Lavrentovich (2006) also showed that other thresholds were present at higher fields. For instance, the two-dimensional, square-grid pattern was destabilized in favor of a 1D structure of parallel walls at about twice the first threshold.

The cholesteric mesophase is the system in which the HH effect was first discovered and theorized. Later, cholesteric systems also enabled subtle experiments for further fundamental studies of the instability. Indeed, the resulting patterns have the advantages of being easily controlled with an external field and of being regular and stable. The last point even suggested possible applications of these systems, such as the design of switchable two-dimensional, diffractive gratings (Senyuk, Smalyukh, and O. D. Lavrentovich, 2005; Ryabchun and Bobrovsky, 2018). However, a cholesteric phase strained by a magnetic field is not the only scenario leading to a HH instability. Any layered systems, such as smectic phases, are expected to show HH instabilities under fields. Electric fields are often easier to apply than magnetic fields, but their effects are more complex to analyze; see Bevilacqua and Napoli (2005). More importantly for this review, HH patterns can also be observed even in the absence of external fields. In the first studies, it was already noted that cholesterics exhibit square-grid patterns transiently under temperature changes or mechanical deformation (Gerritsma and Van Zanten, 1971b). This mechanical-strain-induced HH instability is observed in many other lamellar or columnar systems, including smectic liquid crystals.

## B. Mechanical layer strain in smectics

In smectics, molecules align and arrange into equally spaced parallel planes, creating molecule-thick layers measurable as a one-dimensional density modulation. The buckling instability of smectic phases was identified shortly after the HH effect was observed in cholesteric phases, but with pseudolayers now replaced by actual layers. Unexpected laser light scattering was observed in a smectic-A system, in which the nematic director is parallel to the smectic layer normal. The system was presumed to be well oriented, with the smectic layers parallel to the bounding, homeotropic glass substrates, where the molecules are anchored perpendicularly to the bounding surfaces. Yet the scattered pattern observed was well defined, indicating the presence of periodic structures in the cell. The intensity of the scattered light was shown to be extremely sensitive to the strain of the sample, strongly increasing with dilation but decreasing under compression (Clark and Pershan, 1973; Delaye, Ribotta, and Durand, 1973).

## 1. Mechanically induced Helfrich-Hurault effect

The presence of a periodic pattern in strained smectic-*A* samples was explained by considering displacements of layers with ground-state spacing  $a$  of the form

$$u(x, z) = \alpha z + u_0 \cos\left(\frac{\pi z}{a}\right) \sin(qx), \quad (14)$$

where  $\alpha = \delta a/a \ll 1$  is the global applied strain (Clark and Meyer, 1973). Equation (12) still describes the elastic free energy density of the smectic-*A* phase, where the modulus  $\bar{K} = K$  is now the splay modulus of the director and  $\bar{B} = B$  is the bulk compression modulus. Together they traditionally define the smectic penetration depth  $\lambda = \sqrt{K/B}$ , a length usually comparable to the molecular size. Expanding in  $\alpha$  gives an expression similar to Eq. (9) for the total elastic energy,

$$F_t = \left(\frac{B\pi^2}{a^2} + Kq^4 - B\alpha q^2\right) \frac{V}{8} u_0^2, \quad (15)$$

showing the formal analogy between a uniform strain in a layered system and the application of an external field. Following the analysis in Sec. III.A,  $\alpha$  plays the role of  $H^2$ , so the threshold strain is  $\alpha_c = 2\pi\lambda/a$ , above which undulations ensue (Clark and Meyer, 1973; Singer, 1993, 2000; Napoli and Nobili, 2009). Note that  $\alpha > 0$  for the analogy to hold: compression does not lead to buckling in this system. Since  $\lambda$  is a molecular length scale, the instability appears for small changes of spacing  $\delta a \approx 2\pi\lambda$  and with a wave vector amplitude  $q_c^2 = \pi/\alpha\lambda$ , in concert with Eq. (11).

This analysis holds for lamellar phases under dilation, including cholesterics, but a quantitative difference may be present. A thermotropic smectic-*A* phase or a short-period, lyotropic lamellar phase is a much stiffer material than large pitched cholesteric phases, such as the ones studied by Senyuk, Smalyukh, and O. D. Lavrentovich (2006) with FCPM. This implies that, for sample cells of comparable thicknesses, the pattern wavelengths are much smaller in a short-period, lamellar phase, but also that the sinusoidal profile of the undulation is rapidly destabilized above the HH threshold. Indeed, smectic-*A* layers are often considered to be almost incompressible ( $B \rightarrow \infty$ ), as shown by the ubiquitous presence of topological defects called focal conic domains in disordered samples (Friedel, 1922). These macroscopic structures consist of curved but parallel layers whose common focal surfaces have degenerated into three-dimensional curves, an ellipse and a conjugate hyperbola (Bouligand, 1972a). Therefore, in experiments the dilation of layers is expected to be confined to curves or, eventually, surface discontinuities (Bidaux *et al.*, 1973; Blanc and Kleman, 1999).

Because of this, in smectic-*A* samples the simple undulation pattern can be optically observed only just above  $\alpha_c$ , provided that thick enough samples are used. Increasing the strain slightly above  $\approx 1.7\alpha_c$  induces focal lines (Rosenblatt *et al.*, 1977; Clark and Hurd, 1982). Rosenblatt *et al.* described an ideal fourfold grid pattern in terms of ordered assemblies of geometrical stacks of parallel layers, introducing parabolic

focal conic defects and their corresponding domains (Rosenblatt *et al.*, 1977). Such a structure almost satisfies the homeotropic anchoring at the bounding plates, while the distortions from dilation remain confined to the line defects. While the ideal square-grid pattern is rarely obtained in smectics with a simple strain (a polygonal structure is often observed) (Rosenblatt *et al.*, 1977), it should be noted that the simultaneous application of a shear flow may promote the formation of long-range, ordered square lattices of parabolic, focal conic domains (Oswald and Ben-Abraham, 1982; Chatterjee and Anna, 2012).

## 2. The role of dislocations and disclinations

Although these results all support the analogy between electromagnetic-field-induced and mechanically induced HH effects, a major difference exists in the temporal evolution of the textures. Field-induced patterns are caused by a gain in energy accompanying the reorientation of the layers and are stable. On the contrary, after a uniform strain, the planar texture remains most favorable and can be achieved if layers can be added to the slab. Mechanically induced textures are therefore transient or metastable, as emphasized by Clark and Meyer (1973) and Delaye, Ribotta, and Durand (1973). An efficient mechanism to relax the strain was expected to be the climb of edge dislocations, which are unavoidably present in a smectic slab (Bartolino and Durand, 1977b; Ribotta and Durand, 1977). Note that a smectic-*A* wedge cell with a small angle on the order of  $10^{-3}$  rad already gives rise to a linear density of about one dislocation per micron. This mechanism is difficult to observe directly in smectic-*A* systems. It can, however, be studied in the vicinity of the smectic-*A* to smectic-*C* transition (Blanc *et al.*, 2004) and is easily observed in cholesteric phases due to their larger, micron-scale periodicities, as shown in Fig. 3. We note that cholesterics technically do not have dislocations but instead have  $\chi$  disclinations since they do not have a density modulation (de Gennes and Prost, 1993). We discuss cholesteric defects in greater detail in Sec. V.

Finally, we point out that buckling instabilities are found not only in lamellar systems but also in other modulated phases, such as columnar phases (Livolant and Bouligand,

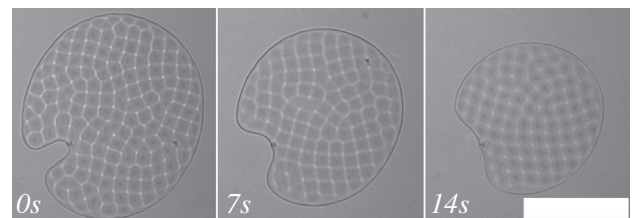


FIG. 3. Relaxation of a dilated region displaying the square-grid pattern through the climb of an edge dislocation loop during a compression-dilation sequence. The cholesteric phase was obtained from mixing 5CB with the chiral dopant (S)-4-cyano-4'-(2-methylbutyl)biphenyl (CB15; 2.8 wt %). The images were obtained from bright-field optical microscopy. The scale bar is 200  $\mu\text{m}$ .

1986; Oswald *et al.*, 1996). We expound more upon the HH instability in a broad range of materials in Sec. IX.

#### IV. LIQUID CRYSTAL SHELLS

In Sec. III, we reviewed the history of the HH instability in both cholesteric and smectic liquid crystals confined between glass plates. All of the previous examples have been in systems with solid boundaries. However, in sensing applications and in biomaterials, liquid crystal systems with periodic ground states are often in contact with fluid (liquid or gas) phases. The boundary conditions are then deformable, resulting in an interplay between bulk and surface energies that gives rise to more complex dynamics and ground states.

Liquid crystal shells are attractive systems for investigating the effect of fluid interfaces on the HH instability due to shell thickness tunability and fine control over the system's boundary conditions through a wide array of techniques, ranging from adjusting the system temperature to altering the system chemistry (Fernandez-Nieves *et al.*, 2007; Lopez-Leon and Fernandez-Nieves, 2009, 2011; Liang *et al.*, 2011, 2012, 2013; Lopez-Leon, Fernandez-Nieves *et al.*, 2011; Lopez-Leon, Koning *et al.*, 2011; Lopez-Leon, Bates, and

Fernandez-Nieves, 2012; Lopez-Leon *et al.*, 2012; Seč, Lopez-Leon *et al.*, 2012; Koning *et al.*, 2013; Darmon, Benzaquen, Čopar *et al.*, 2016; Darmon, Benzaquen, Seč *et al.*, 2016; Darmon, Dauchot *et al.*, 2016; Zhou *et al.*, 2016; Tran *et al.*, 2017; Noh *et al.*, 2020). Shells are water-in-liquid-crystal-in-water double emulsions, where a thin liquid crystal layer is confined between an inner water droplet and an outer continuous water phase, produced in microfluidic devices made of nested glass capillaries [Fig. 4(a)]. In these devices, a water-in-liquid-crystal compound jet is sheared by an outer aqueous solution [Fig. 4(c)], leading to its breakup into water droplets that are encapsulated by liquid crystal [Fig. 4(b)] (Utada *et al.*, 2005; Fernandez-Nieves *et al.*, 2007). This technique enables both the production of highly monodisperse samples and independent control over the size of the inner and outer diameters. The thickness and curvature of the shells can be selected by adjusting flow rates during microfluidic production [Fig. 4(c)]. The shell thickness can also be varied through differences in density between the inner phase and the liquid crystal [Fig. 4(b), bottom right panel], as well as through osmotic swelling or deswelling, postproduction. Tuning the shell thickness with osmotic pressure is accomplished by changing the concentration of a solute, such as salt

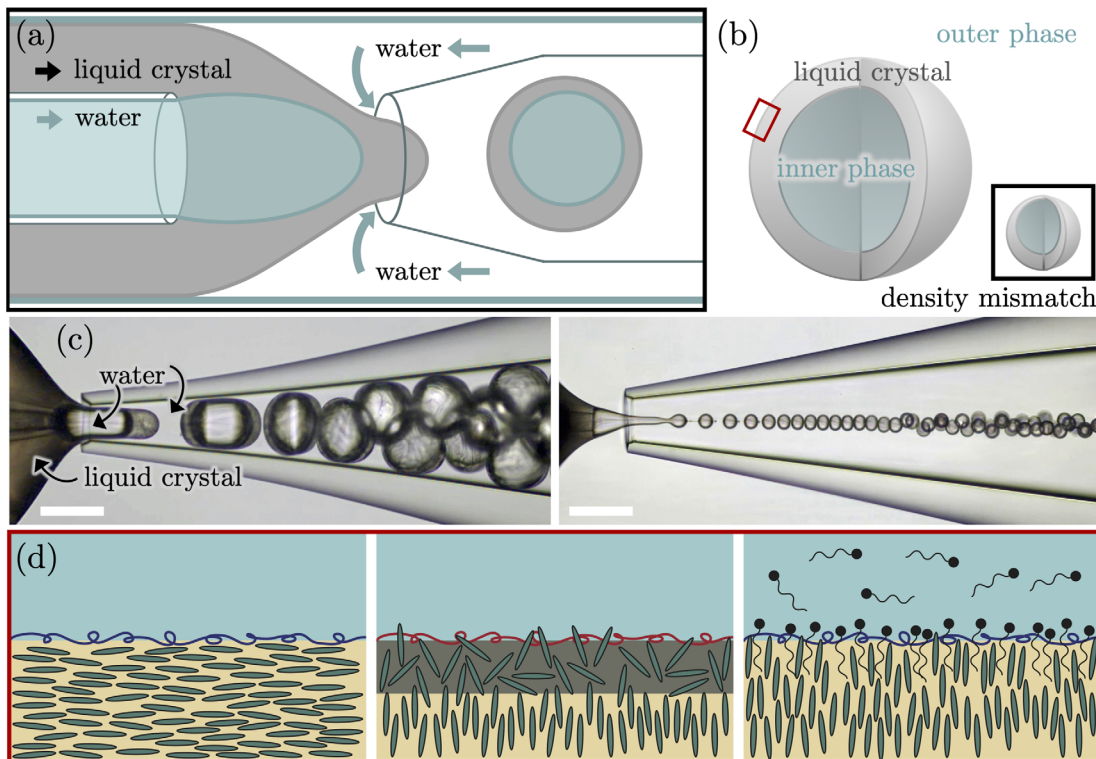


FIG. 4. (a) Schematic of a microfluidic device for nested glass capillaries used for producing liquid crystal shells. (b) Schematic of a liquid crystal shell. If there is a density mismatch between the inner phase and the liquid crystal, then one side of the shell will be thin from buoyancy effects. The scenario for a denser liquid crystal phase is shown at the bottom right. (c) Microphotographs of capillary devices used to produce shells. The two photographs show the typical (left) maximal and (right) minimal sizes that one can attain with a given device geometry. Scale bar, 200  $\mu\text{m}$ . (d) Schematics for techniques used to change the anchoring at a water/liquid crystal interface [enlargement of the shell schematic in (b)]. Left panel: in the presence of PVA, the anchoring is strongly planar. Center panel: the system transitions to a perpendicular (homeotropic) orientation when its temperature is brought a couple tenths of a degree celsius below the clearing point of the bulk 5CB resulting from the presence of an interfacial melted layer of 5CB and PVA. Right panel: homeotropic anchoring can also be regulated by adding surfactants to the aqueous phase. The amount of adsorbed surfactant to the water-liquid crystal interface determines the homeotropic anchoring strength.

or sugar, in the surrounding aqueous solutions (Lopez-Leon, Koning *et al.*, 2011; Seč, Lopez-Leon *et al.*, 2012; Tu and Lee, 2012; Darmon, Benzaquen, Seč *et al.*, 2016; Tran *et al.*, 2017). Osmotically swelling the liquid crystal shells is useful for observing the temporal evolution of thickness- or curvature-dependent phenomena (Lopez-Leon, Koning *et al.*, 2011; Darmon, Benzaquen, Seč *et al.*, 2016; Urbanski *et al.*, 2017; Durey *et al.*, 2020; Tran and Bishop, 2020).

Furthermore, the anchoring at the inner and outer water-liquid crystal interfaces of the shell can be set independently. In the simplest case, shells of 4'-pentyl-4-biphenyl-carbonitrile (5CB) in contact with pure water have matching planar boundary conditions on both the inner and outer shell surfaces. The planar anchoring is degenerate, which means that the director is free to rotate on the surfaces. The planar anchoring strength can be increased with the introduction of polyvinyl alcohol (PVA) in the aqueous phases. This polymer surfactant also increases the shell stability by decreasing the water-liquid crystal interfacial tension and inducing a repulsive force (a disjoining pressure) when the inner and outer interfaces get closer together [Fig. 4(d), left panel]. The increased shell stability allows for the shell anchoring conditions to be dynamically and gradually tuned with simple modifications to the system, mainly through two mechanisms.

The first method involves quasistatically bringing the system temperature a few tenths of a degree celsius below the clearing point of the bulk 5CB. With slow ramps in the temperature, the shells can undergo a series of anchoring transitions where the alignment of mesogens with respect to the interface changes, either from planar to homeotropic for increasing temperature or vice versa for decreasing temperature. In a shell where the temperature is slowly increased, the anchoring shifts from matching planar anchoring on the inner and outer shell surfaces, to hybrid anchoring, and then to matching homeotropic anchoring before fully transitioning to the isotropic phase (Durey, Ishii, and Lopez-Leon, 2020). This behavior has been linked to the PVA polymer at the shell interfaces, which renders the liquid crystal more disordered near the interfaces than in the bulk. The shell interfaces then favor the nucleation of the isotropic phase. The melted layer and the bulk nematic create a new, low-anchoring-strength interface accounting for the changes in anchoring observed in the shell with increasing temperature [Fig. 4(d), middle panel].

The second technique relies on the dissolution of surfactants in the water phases. As small amphiphilic molecules adsorb on the shells' interfaces, their aliphatic tails force the liquid crystal molecules to reorient perpendicular to the boundary, as illustrated in the rightmost panel of Fig. 4(d) (Drzaic and Scheffer, 1997; Poulin and Weitz, 1998; Noh, Reguengo De Sousa, and Lagerwall, 2016; Sharma and Lagerwall, 2018). This yields homeotropic boundary conditions with a tunable anchoring strength that increases with the surfactant surface coverage (Brake and Abbott, 2002; Brake, Mezera, and Abbott, 2003a, 2003b; Lockwood, Gupta, and Abbott, 2008; Carlton *et al.*, 2012; Ramezani-Dakhel *et al.*, 2018). For a cholesteric twisting along a water-liquid crystal interface, it has been shown that surfactants localize in the homeotropic regions and are excluded from planar regions (Fig. 5) (Tran *et al.*, 2018). This cross communication between the bulk and the surface results in patterned chemical

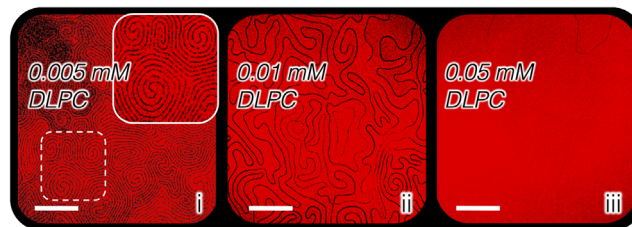


FIG. 5. Laser scanning confocal micrographs of the lipid surfactant 1,2-dilauroyl-sn-glycero-3-phosphocholin (DLPC), labeled with 1 mol % Texas Red 1,2-dihexadecanoyl-sn-glycero-3-phosphoethanolamine, triethylammonium salt demonstrates the cross communication of the liquid crystal and the adsorbed surfactant on a cholesteric-water interface of a flat film within a TEM grid. The surfactant causes homeotropic anchoring, which induces stripe patterns in the cholesteric. The cholesteric subsequently patterns the surfactant, causing it to segregate into stripes at the cholesteric-water interface. As the surfactant concentration increases from (i) to (iii), (ii) surface stripes become wider and more disordered (iii) until regions where the cholesteric twist violates the homeotropic anchoring condition are forced away from the surface as a result of the lipids saturating the interface. Adapted from Tran *et al.*, 2018.

heterogeneity at the cholesteric interface and could manifest in other liquid crystal phases in which the bulk competes with the surface anchoring. Responsive surfactants enable further control of surfactant adsorption and conformation at the interface with means beyond the surfactant concentration, such as through temperature, pH, and UV light intensity (Kwon, Khan, and Park, 2016; Dogishi *et al.*, 2018; Sakai, Sohn, and Katayama, 2019; Sharma, Jampani, and Lagerwall, 2019).

The flexibility of the shell system thus lends itself to helping study the role of surface tension, anchoring, and boundary curvature on the HH instability. In Secs. V and VI, the outlined techniques are employed to investigate undulating instabilities in cholesteric and smectic shells.

## V. CHOLESTERIC SHELLS

Since the classic HH instability was first discovered in cholesterics, we begin by examining cholesteric shells made of 5CB doped with a chiral dopant, (S)-4-cyano-4'-(2-methylbutyl)biphenyl (CB15). In the following, we review how undulations can develop in the cholesteric pseudolayers in response to global geometrical, i.e., topological, frustration, as well as changes in the mesogen anchoring. We also review how undulations occur not only within the bulk but also at the interface itself. Cholesteric shells demonstrate how fluid boundaries play a significant role in the HH instability while also illustrating that the instability is, at its core, a response to local geometrical frustration.

### A. Planar cholesteric shells

Planar anchoring in cholesteric shells frustrates the bulk ordering and induces structures that can be seen as a manifestation of the HH instability, broadly construed. Why is there frustration when the pitch axis does not lie in

the tangent plane of the shell? The answer is the global geometry (the topology) of the system. Since it is the director that lies in the planar shell's tangent plane, the Poincaré-Brouwer-Hopf theorem requires the sum of the indices of the zeros of a line field to be equal to the Euler character of the shell (Poincaré, 1885; Brouwer, 1911; Hopf, 1927). Zeros of the line field are topological defects (places where the local orientation is undefined), while the index of the zero is its signed winding. For a sphere, the Euler character is 2, so the net winding of the defects on the shell surface must be  $2 \times 2\pi$ , manifesting as four  $+1/2$  defects, two  $+1$  defects or one  $+2$  defect; two  $+1/2$  defects and a  $+1$  defect, three  $+1$  defects and one  $-1$  defect, etc. Although the necessity of a minimum number of defects can be thought of as topological frustration that arises from the system's global curvature, the defects can also be viewed as manifesting from local incompatibilities, i.e., as local geometrical frustration.

We begin by considering the simplest case of nematic defects, i.e., defects in the director field. Moving inward from the shell surface along its normal is equivalent to moving along the cholesteric pitch axis, by definition. Thus, there is a slightly smaller sphere just below the outer surface, which also has planar anchoring and thereby must also have these defects (note that the global rotation of the director field does not contribute to the defect charge). If the pitch axis remains radial from the outer to the inner surface of the shell, then the shell would consist of a series of concentric spheres, each with two-dimensional defects.

From the three-dimensional perspective, these defects are not independent and would connect up into line defects with net winding  $4\pi$ . This is seen in planar nematic shells, where the shell thickness controls the amount and winding number of defects (Vitelli and Nelson, 2006; Fernandez-Nieves *et al.*, 2007; Lopez-Leon, Koning *et al.*, 2011; Koning *et al.*, 2013, 2016). Recall, however, that for a nematic in three dimensions, integer-winding defect lines are not topologically stable: they can “escape into the third dimension” (Meyer, 1973). This deformation has an associated bend energy (and possibly twist), so for thin nematic shells this does not happen. However, as the shells thicken, the director goes smoothly from being horizontal (parallel to the tangent plane of the sphere) in the periphery of the defect to vertical at the core. The only singularities left in the system after this escape are point defects, or “boojums,” that have been pushed away to the shell surfaces (Volovik and O. D. Lavrentovich, 1983; O. D. Lavrentovich, 1998).

However, cholesteric defects are considerably more complex than nematic defects. While a nematic is characterized by a single director field  $\mathbf{n}$ , an unfrustrated cholesteric is properly described at large scales by three mutually orthogonal line fields: the director  $\mathbf{n}$ , the pitch axis  $\hat{\mathbf{P}}$ , and their cross product  $\mathbf{\hat{n}} \equiv \mathbf{n} \times \hat{\mathbf{P}}$ . Winding defects are now characterized by both their strength and the axis around which they rotate. When one adopts the notation of Friedel and Kleman (1970), defects where the pitch axis and  $\mathbf{\hat{n}}$  rotate around the director are labeled  $\lambda$ . On the other hand, defects where  $\mathbf{\hat{n}}$  and the director axis rotate around the pitch axis are labeled  $\chi$ . Finally, defects in both the director and the pitch axis, where the two rotate about  $\mathbf{\hat{n}}$ , are labeled  $\tau$ . Examples of each of

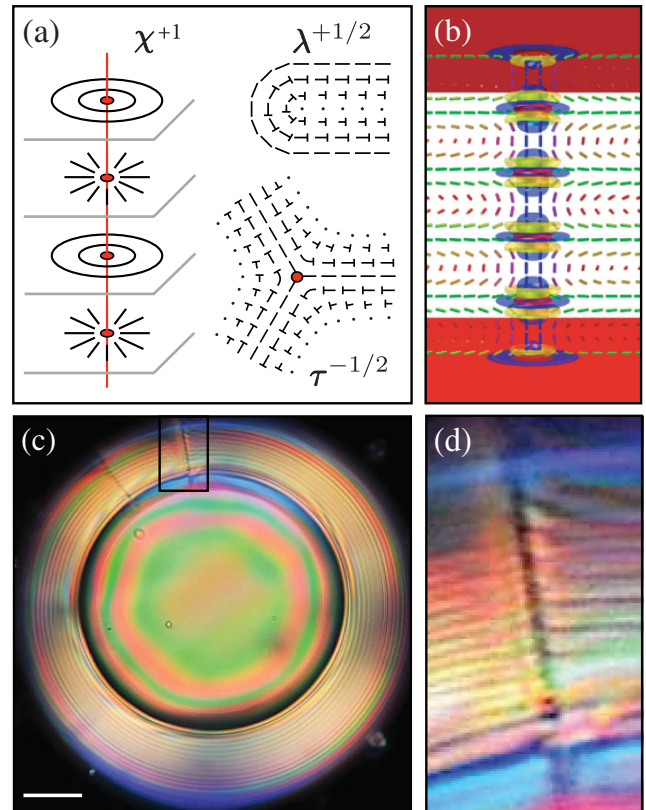


FIG. 6. The  $\chi^{+1}$  disclination line in a planar cholesteric shell: experiment and simulation. (a) Schematics of  $\chi^{+1}$ ,  $\tau^{-1/2}$ , and  $\lambda^{+1/2}$  disclinations in cholesterics. (b) Simulated cross section of an  $m = +1$  defect. The blue and yellow regions, respectively, indicate zones of high splay and bend distortion; red indicates director singularities. (c) Micrographs showing a side view of a shell with two  $m = +1$  defects between crossed polarizers revealing a visible nonuniform structure of the defect core, which is enlarged in (d). Scale bar is  $20 \mu\text{m}$ . Adapted from Darmon, Benzaquen, Čopar *et al.*, 2016.

these defects are illustrated in Fig. 6(a). Although these defects are similar in their algebra to defects in biaxial nematics (Mermin, 1979), the existence of pseudolayers spoils a precise correspondence (Beller *et al.*, 2014). However, as in biaxial nematics, defects cannot escape into the third dimension: as a defect in the director attempts to escape, a new defect in either  $\hat{\mathbf{P}}$  or  $\mathbf{\hat{n}}$  appears. In the naive mapping between cholesteric pseudolayers and smectics, the  $\chi$  defects correspond to dislocations, while the  $\lambda$  and  $\tau$  defects are the standard disclinations. Note that while the  $\lambda$  defects do not have a singularity in the director field, they have one in the cholesteric structure since the pitch axis is undefined.

To illustrate a  $\chi$  defect, it is useful to view them as line disclinations within a three-dimensional nematic, but with an added modulation along their length due to the cholesteric twist. Consider any point defect with  $m \neq 1$  in a two-dimensional nematic: locally rotating the director by a constant angle at every point of the plane will simply induce a global rotation of the defect. Thus, a  $\chi$  line disclination with  $m \neq 1$  in a cholesteric can be pictured as a two-dimensional

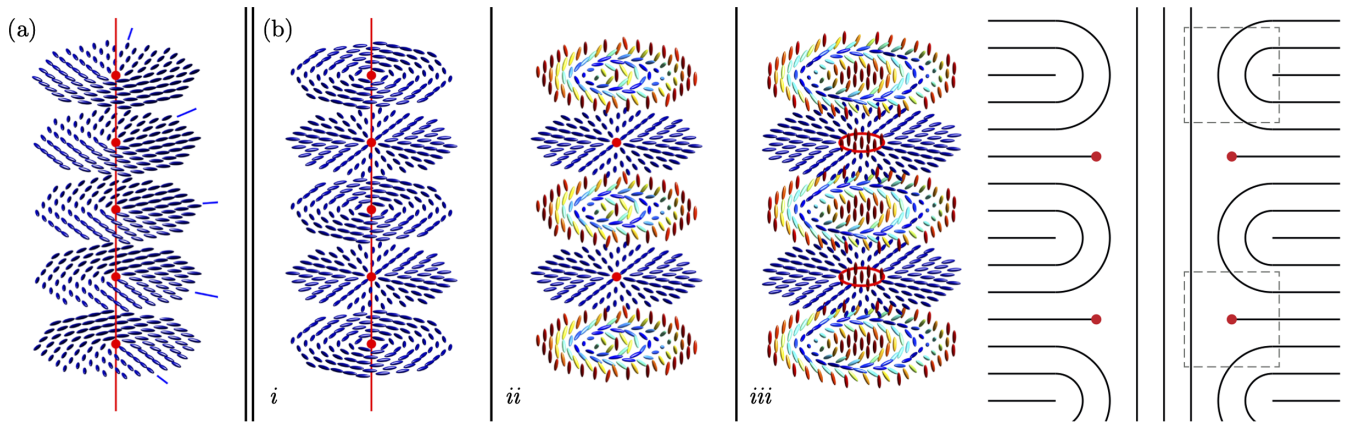


FIG. 7. (a) Schematic of the structure of a  $\chi^{+1/2}$  line that consists of a smoothly twisted  $m = +1/2$  defect line. The red line denotes the singularity, and the red dots mark the intersection of that line with the represented cross sections of the director field. The blue lines at the right edge of the cross sections are drawn as a guide for the eye toward the rotation of the  $m = +1/2$  defects. (b) Schematics of the  $\chi^{+1}$  line. (i) “Textbook” version of the  $\chi^{+1}$  line seen as alternating bend and splay  $m = +1$  director defects along a vertical singular line. (ii) Semiescaped version of (i) in which the line singularity “escapes” in between the splay defects, transforming regions of high bend into  $\lambda^{+1}$  defects. (iii) The line in (ii) is further relaxed. Left panel: the  $m = +1$  splay point defects are relaxed into  $m = +1/2$  loops, and the core of the  $\lambda^{+1}$  defects also expand. This relaxation creates a column of vertically aligned nematic in the center of the defect. This is apparent in the right panel. Right panel: depiction of the director as black lines within a vertical cross section. Connecting the horizontal layers of the far field with the vertical layers in the center frustrates the system, generating undulations reminiscent of the Helfrich-Hurault instability. The undulations produce periodic defects, which are highlighted by dashed boxes (top box,  $\lambda^{+1/2}$ ; bottom box,  $\tau^{-1/2}$ ).

point defect extended in the third direction, which is then smoothly twisted [Fig. 7(a)].

However, we see the possibility of a more complex  $\chi$  defect within a cholesteric shell that has degenerate planar anchoring on the inner and outer boundaries. A cross-polarized micrograph of a shell with this morphology is shown in Fig. 6(c). The pseudolayers form concentric spheres, with the smallest and largest corresponding to the shell boundaries. The signature of the pseudolayers is visible as a series of concentric dark rings, spaced apart by half of the pitch [Fig. 6(d)]. The twist axis lies along the radial direction since it is perpendicular to those layers. One can posit that defects in cholesteric shells are radially oriented, singular lines spanning the shell thickness. Structures that seem to be radial lines are visible in Fig. 6(c). However, at higher resolution, the defects appear to be more complex than a simple line, with periodic distortions along their length. We can see the defect within the shell as a charge  $\chi^{+1}$  disclination running from the inner to the outer surface [locally depicted in Figs. 7(b)(i)]. Compared to  $\chi$  disclinations with  $m \neq 1$ , rotating the director of a  $\chi^{+1}$  disclination produces an alternating pattern of pure splay and pure bend defects separated by a quarter pitch. Were we to trace out a surface of constant director orientation, we would find something with the topology of a helicoid, a dislocation in the pseudolayers, as promised. However, the defects deform: in the plane perpendicular to the disclination, the director field attempts to unwind.

Although in the nematic escaping into the third dimension could lower the amount of elastic distortion in the system and remove any singularities in the director, this is not possible in a cholesteric. The cholesteric’s triad of line fields prevents a full

escape of the line singularity. The singularity can escape only in alternating regions with a periodicity set by the pitch. Regions of high splay retain director discontinuities at their centers, while the regions of high bend in between are escaped. By escaping, these bend regions become  $\lambda^{+1}$  defects. At the core of a  $\lambda^{+1}$  defect, the director is vertical (i.e., radial in the reference frame of the shell), and moving away from the core the director twists smoothly in all directions, becoming points of double twist. On both interfaces of the shell, the semiescaped  $\chi^{+1}$  line terminates with a boojum as in the nematic. This semiescaped  $\chi^{+1}$  line is shown in Fig. 7(b)(ii).

Moreover, the singularity in Fig. 7(b)(ii) can relax further into the structure in Fig. 7(b)(iii) to reduce the overall amount of elastic distortion.  $+1$  splay defects can open up into looped  $+1/2$  disclinations. Inside those defect rings, the director field is uniformly vertical. The vertically oriented director field at the core of the  $\lambda^{+1}$  defects similarly expands. The line singularity in Fig. 7(b)(i) is replaced by a vertically aligned director field (i.e., radially aligned in the reference frame of the shell), as depicted in Fig. 6(b) (Seč, Porenta *et al.*, 2012; Darmon, Benzaquen, Čopar *et al.*, 2016; Darmon, Benzaquen, Seč *et al.*, 2016).

With the singularity in Fig. 7(b)(iii) being the most energetically favorable, we can see how the defects form in experimental systems. Looking at a vertical cross section of the relaxed, semiescaped  $\chi^{+1}$  line, there is an incompatibility in the director orientation between the center of the singularity and the director field far away from it. To connect the vertical director lines at the center of the relaxed, semiescaped  $\chi^{+1}$  line with the concentric planar layers that constitute the rest of the shell, undulations along the singularity can result

[Fig. 7(b)(iii), right panel]. The “crests” of the undulations can generate  $\lambda^{+1/2}$  disclinations, while the “valleys” can create  $\tau^{-1/2}$  disclinations, which is reminiscent of alternating  $\lambda^{\pm 1/2}$  defects often seen in cholesterics (Beller *et al.*, 2014). As this system has rotational invariance around the axis of the original  $\chi^{+1}$  line,  $\tau^{-1/2}$  and  $\lambda^{+1/2}$  are looped defects, as illustrated in the left panels of Fig. 7(b) (Seč, Porenta *et al.*, 2012; Darmon, Benzaquen, Čopar *et al.*, 2016; Darmon, Benzaquen, Seč *et al.*, 2016).

The semiescaped singularities in cholesteric shells can be viewed through the lens of the HH mechanism: The mismatch between the vertical director field lines and the far-field, horizontal layers embodies geometrical frustration that is topologically induced by the global curvature of the shell. As in the classical HH systems, the frustration is relieved through periodic elastic distortions that can generate a regular array of defects. However, unlike the original HH analysis, the undulation wavelength in planar cholesteric shells is set by the pitch: the pseudolayer periodicity. This difference arises from how the geometrical frustration in planar cholesteric shells is induced by the system’s global curvature, rather than by an external field. Defects in planar cholesteric shells reveal how topology, i.e., global curvature, can give rise to local geometrical frustration in layered liquid crystal systems. That the frustration in planar cholesteric shells is relieved through periodic distortions demonstrates the ubiquity of the HH instability, interpreted in this broad sense of relieving layer strain through an undulation with its own periodicity. In this case, the “undulation” is a periodic array of defects.

## B. Homeotropic cholesteric shells

Beyond applied external fields and topological frustration, the competition between the interface and the bulk can also trigger the HH instability, exemplified by cholesteric shells with homeotropic anchoring, shown in Fig. 8. Homeotropic anchoring conditions are particularly frustrating for cholesterics, as the anchoring always favors an untwisted configuration of molecules and is incompatible with the pseudolayer structure preferred by the bulk. This incompatibility induces defect structures (arrays of disclination lines), much like the

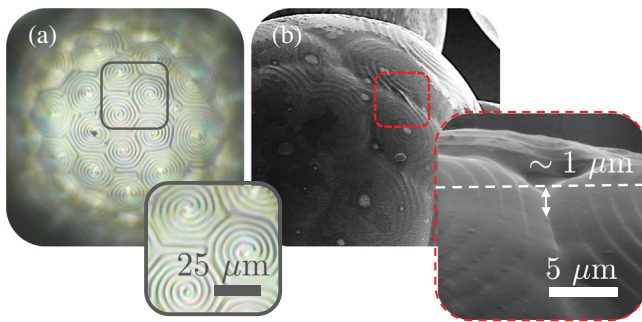


FIG. 8. (a) Polarizing micrograph of a cholesteric shell with homeotropic anchoring due to the presence of a surfactant in the surrounding aqueous solution. (b) A polymerized and dried cholesteric shell with homeotropic anchoring accentuates interfacial deformations due to the underlying focal conic domains. The scanning electron micrographs are courtesy of Daeseok Kim.

ones shown in Fig. 7. However, unlike the case of planar anchoring discussed in Sec. V.A, the homeotropic cholesteric shell typically has defects tiling the entire surface, not at just a few topologically required points, evidenced by the micrograph in Fig. 8(a). Indeed, the anchoring incompatibility is an example of local frustration. Additionally, the interface itself may locally undulate and deform in response to these defects to further accommodate the anchoring conditions, which are shown in the scanning electron micrograph in Fig. 8(b). In this case, the surface tension  $\sigma$  must necessarily play a role in establishing the shape of the fluid interface.

Consider the energy contributions of the boundary. A fluid interface introduces both an anchoring energy and a surface tension  $\sigma$  that will generally compete with the bulk free energy. These boundary effects may be significant, distorting the interface and modulating the ordering within the layered system (Meister, Dumoulin *et al.*, 1996). If one assumes a simple model of the interface as a height field<sup>3</sup>  $h \equiv h(x, y)$ , a general surface energy at a fluid interface would have the form

$$f_s = \int d^2\mathbf{x} \sqrt{1 + (\nabla h)^2} [\sigma + A(\hat{\mathbf{v}}, \mathbf{n})], \quad (16)$$

where  $\sigma$  is the surface tension and  $A(\hat{\mathbf{v}}, \mathbf{n})$  is an anchoring strength that will depend on the orientation between the interface normal  $\hat{\mathbf{v}}$  and the nematic director  $\mathbf{n}$  at the surface. The director  $\mathbf{n}$  is perpendicular to the pseudolayer normal  $\mathbf{N}$  in cholesteric phases, but Eq. (16) generally holds for all lamellar liquid crystals ( $\mathbf{n}$  can be parallel or at an angle to  $\mathbf{N}$  for smectic-A or other smectic phases, respectively).

The anchoring term must be invariant under  $\mathbf{n} \rightarrow -\mathbf{n}$ , so we can write  $A(\hat{\mathbf{v}}, \mathbf{n}) = W[1 - (\hat{\mathbf{v}} \cdot \mathbf{n})^2]/2$ , with an anchoring strength  $W > 0$  for homeotropic alignment and  $W < 0$  for degenerate planar alignment (Rapini and Papoular, 1969). Note that this anchoring energy can compete with the periodic ordering of the bulk. This is necessarily the case for cholesterics (Meister, Dumoulin *et al.*, 1996): if the cholesteric pitch axis is oriented in any direction away from the surface normal, the twist of the cholesteric competes with the boundary condition of that surface, whether it is planar or homeotropic. Indeed, when  $W > 0$ , there is no configuration that is compatible with a periodic cholesteric and the surface would tend to unwind the cholesteric, competing against the ground-state pitch. The anchoring therefore takes the role of an applied electromagnetic field, but the reorientation of the director occurs only at the surface, not throughout the entire system. As in the classic system presented in Sec. III, anchoring can also trigger the HH instability, inducing undulations in the cholesteric pseudolayers. These reorientations undulate the layers just underneath the cholesteric surface, as indicated by the orange line in Fig. 9.

The onset of undulations is not surprising when the magnitudes of anchoring, surface tension, and bulk elastic

<sup>3</sup>Note that  $h(x, y)$  is a Lagrangian displacement variable of the surface, while  $u(x, y, z)$  is the Eulerian displacement of the layers. The difference matters at nonlinear order, in principle (Kamien and Lubensky, 1999).

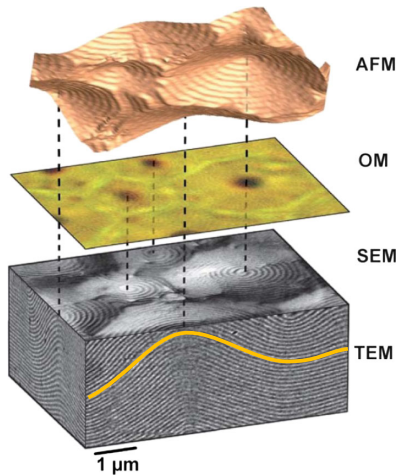


FIG. 9. An undulated cholesteric fluid interface imaged via atomic force microscopy (AFM), optical microscopy (OM), scanning electron microscopy (SEM), and transmission electron microscopy (TEM). The incompatible homeotropic anchoring at the surface forces the bulk layers to undulate (orange line) and turn upward, forming focal conic domain “hills.” From Agez, Bitar, and Mitov, 2011.

energies of typical systems are considered. For example, in common cyanobiphenyl-type liquid crystals with chiral dopants that induce micron-scale pitches, the nematic-isotropic or aqueous interface has an anchoring strength  $W \sim (10^2\text{--}10^5)kT/\mu\text{m}^2$  (Faetti and Palleschi, 1984) and surface tension  $\sigma \sim (10^5\text{--}10^6)kT/\mu\text{m}^2$  (Kim *et al.*, 2004). The bulk elasticity terms have magnitudes  $K_{1,2,3} \sim 10^3kT/\mu\text{m}$  (Bradshaw *et al.*, 1985). Thus, when the liquid crystal is forced to have defects (with cores on the scale of 1–10 nm) to accommodate a frustrating boundary condition, the defects can contribute energy per unit area on the order of  $K_i/(10\text{ nm}) \sim 10^5kT/\mu\text{m}^2$ . Therefore, for the cholesterics considered here, all of these energetic contributions can compete with one another.

Note that these surface instabilities differ in some ways from the HH instability induced by a bulk field. In a nematic, a boundary condition may reorient the nematic order throughout the bulk, as in a liquid crystal display cell. Thus, boundary conditions serve to orient the nematic order just as in a bulk field. In a layered system, however, deformations may be confined to a region around the boundary with a characteristic size equal to the penetration depth  $\lambda \approx \sqrt{K/B}$  [see Eq. (3)], which was previously analyzed in detail for cholesterics with a free interface (Meister, Dumoulin *et al.*, 1996). These localized deformations are also observed in simulations, as shown in Fig. 10. Note that both a bulk field and a surface anchoring term will introduce a quadratic term proportional to  $(\hat{\mathbf{x}} \cdot \mathbf{n})^2$  or  $(\hat{\mathbf{x}} \cdot \mathbf{N})^2$ , with  $\hat{\mathbf{x}}$  the direction of either the surface normal or the applied field. For a cholesteric, note the similarity between the surface energy in Eq. (16) containing the term  $A(\hat{\nu}, \mathbf{n}) = W[1 - (\hat{\nu} \cdot \mathbf{n})^2]/2$  and an electric field contribution  $f_e = -(1/2)\Delta\epsilon\epsilon_0(\mathbf{E} \cdot \mathbf{n})^2$ , with  $\Delta\epsilon$  the dielectric anisotropy (Yu, Yang, and Yang, 2017). Both of these terms may reorient the layered structure and create the proper conditions for the HH

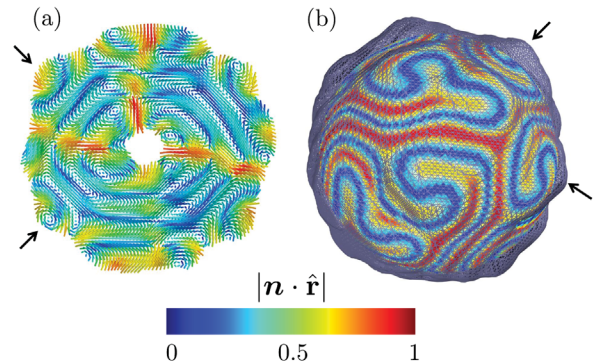


FIG. 10. (a) Cross section through a simulated cholesteric shell with an isotropic-cholesteric interface. The layers are distorted near the boundary and concentric in the bulk. Arrows indicate hills formed by focal conic domains. The color indicates the director  $\mathbf{n}$  orientation relative to the radial direction  $\hat{\mathbf{r}}$ . The pitch  $P_0$  to shell thickness  $t$  ratio is  $t/P_0 \approx 2$ . (b) The distorted outer interface is shown, with the director distribution just underneath the surface colored by  $|\mathbf{n} \cdot \hat{\mathbf{r}}|$ . From M. O. Lavrentovich and Tran, 2020.

mechanism. We explore the mechanism in the context of anchoring transitions in more detail in Sec. V.C.

In cholesterics, the ratio  $\sigma/W$  between the interface surface tension  $\sigma$  and the homeotropic anchoring strength  $W$  determines whether one finds a smooth ( $\sigma/W \gg 1$ ) or cusped ( $\sigma/W \ll 1$ ) interface shape (Meister, Dumoulin *et al.*, 1996). Moreover, depending on how the cholesteric rearranges near the interface, the interface shape will change to accommodate any defect structures. These considerations also come up near the interface between a cholesteric and an isotropic phase, which favors homeotropic alignment, as discussed in Sec. IV (Silvestre *et al.*, 2016; Durey, Ishii, and Lopez-Leon, 2020).

When bulk layer distortions become large and one is far above the threshold for undulations, more complex states emerge. Secondary instabilities, where undulations develop on top of the original undulations, are possible. For cholesterics, layers may undulate in two orthogonal directions, creating an array of focal conic domains (Meister, Hallé *et al.*, 1996; Senyuk, Smalyukh, and O. D. Lavrentovich, 2006) that is also seen in the classic smectic system detailed in Sec. III.B. In extreme cases, such as those with strong incompatible anchoring, the layer structure will strongly distort or break up entirely, yielding intricate defect structures (Yada, Yamamoto, and Yokoyama, 2003; Seč, Čopar, and Žumer, 2014).

Simulation methods are often employed to capture the interplay among the anchoring energy, the bulk elasticity, and the interfacial surface energy (Rofouie, Pasini, and Rey, 2015; Tran *et al.*, 2017; M. O. Lavrentovich and Tran, 2020). An example is shown in Fig. 10. We simulate a cholesteric liquid crystal near coexistence between a cholesteric phase (with a pitch  $P_0$ ) and an isotropic phase. By initializing a shell of the cholesteric inside a bulk isotropic phase, it is possible to generate isotropic-cholesteric fluid interfaces. As mentioned in Sec. IV, these interfaces have a weakly homeotropic anchoring for the cholesteric, creating an anchoring incompatible with the concentric spherical layer arrangement in the droplet bulk. We see in Fig. 10 that there is layer reorientation and formation of focal conic domain hills at the shell surface. The parameters and details of the simulation were described

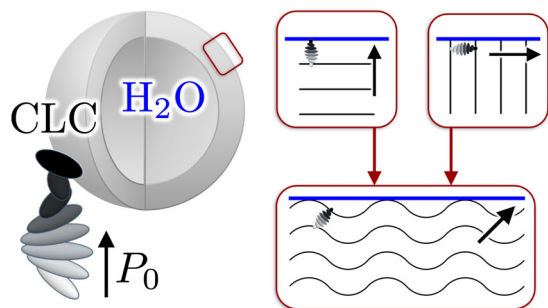


FIG. 11. Schematic of a cholesteric liquid crystal (CLC) shell. Right panels: insets illustrating how changing the anchoring at the shell interface alters the pitch axis orientation, which can lead to a HH-like instability in the bulk (bottom right panel). From M. O. Lavrentovich and Tran, 2020.

by M. O. Lavrentovich and Tran (2020). These focal conic domain hills are also visible in the cholesteric surface relief shown in Fig. 9. Accounting for a deformable boundary and surface tension in the HH instability allows us to capture the interfacial deformations seen in homeotropic cholesteric shells.

### C. Anchoring transitions

The HH instability can also describe transient states that arise from transitions between the planar and homeotropic structures detailed in Secs. V.A and V.B. The changing anchoring is analogous to the application of an external field but with molecular realignment occurring only at the confining surfaces. As in the classical HH instability, transitioning from one type of anchoring to another at an interface causes the cholesteric pseudolayers to reorganize in order to accommodate the new boundary condition, leading to frustration in the system. As described in Sec. V.B, the frustration in the layers can be relieved by a HH-like mechanism, as illustrated for a cholesteric shell in Fig. 11 (M. O. Lavrentovich and Tran, 2020). In this section, we focus on modeling the onset of the HH instability triggered by changes in anchoring conditions.

As detailed in Sec. IV, the anchoring on a cholesteric shell can be tuned experimentally by the addition or removal of surfactant in the surrounding aqueous phases. For the planar to homeotropic anchoring transition, in which surfactant is added to the outer aqueous solution, stripes with a  $2P_0$  periodicity cover the cholesteric shell surface without forming a distinguishable pattern (Fig. 12). Defects in the nematic director are still present in the system but do not influence the conformation of the stripes beyond their termination at said defects, as seen in Fig. 12(a)(ii). Similar stripe patterns are captured in Landau-de Gennes simulations of an initially planar cholesteric shell set to minimize under homeotropic anchoring conditions [Fig. 12(b)]. Large transient stripes are formed on the simulated shell surfaces at the beginning of the minimization, which is similar to experimental observations. Cross sections of the simulated shell reveal that the origin of the large stripes are undulations of the initially concentric, cholesteric pseudolayers [Fig. 12(b)(ii)]. Furthermore, layer undulations are greatest in cross sections that intersect with the

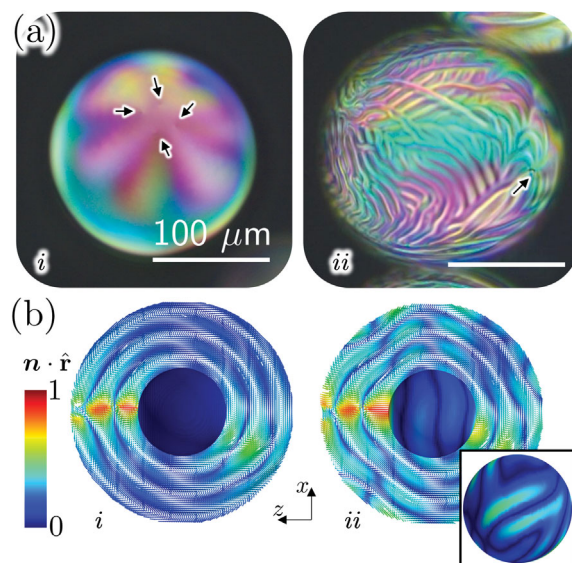


FIG. 12. (a) Cross-polarized images of an initially planar cholesteric shell (i) that has four topological defects with charges totaling  $+2$ . After the shell is introduced to a solution including 10 mM sodium dodecyl sulfate, the anchoring at the outer shell surface transitions from planar to homeotropic, tilting the pitch axis away from the radial direction. (ii) Large stripes are generated at the shell interface with a periodicity of around  $10 \mu\text{m}$ , which is twice the pitch. Arrows indicate defect locations. (b) Simulations of (i) an initially planar cholesteric shell with a  $1.2 \mu\text{m}$  pitch, a  $6.6 \mu\text{m}$  diameter, and a  $2.1 \mu\text{m}$  thickness is minimized under moderate homeotropic anchoring conditions ( $\sim 2 \times 10^{-4} \text{ J/m}^2$ ). (ii) After  $t = 5000$  minimization steps, the cholesteric pseudolayers undulate and generate stripes (shown in the inset). Adapted from M. O. Lavrentovich and Tran, 2020.

radial director defect, indicating that defects are energetically preferred sites for pitch axis and, consequently, cholesteric layer rearrangement.

The transition to planar anchoring similarly produces large surface stripes, where the surfactant is removed from the outer aqueous solution. However, unlike for the transition to homeotropic anchoring, the composition of stripe instabilities for planar transitions is dictated by the initial shell patterning shown in Fig. 13(a). As the surfactant leaves the interface, weakening the homeotropic anchoring, the planar stripes of the focal conic domain widen until they reach a width  $\sim 2P_0$ , after which the planar stripes are filled by orthogonal stripes that have a  $2P_0$  periodicity. The overall double spiraled structure of the initial focal conic domain is preserved [Fig. 13(a)(iv)].

Note that the curvature and composition of the orthogonal stripes in the planar transition is reminiscent of Bouligand arches [illustrated in Fig. 14(a)]. A work on the chromosomes of dinoflagellates by Bouligand, Soyer, and Puisieux-Dao (1968) attributed bands of bow-shaped lines found in thin sections of chromosomes to the chiral ordering of filaments in the chromosomes. The arches that fill in the striped texture of chromosomes are a result of viewing them on a surface that cuts the cholesteric at an angle from the pitch axis.

Indeed, anchoring transitions force the pitch axis to tilt at an angle to the interface, as illustrated in Fig. 11. It is therefore

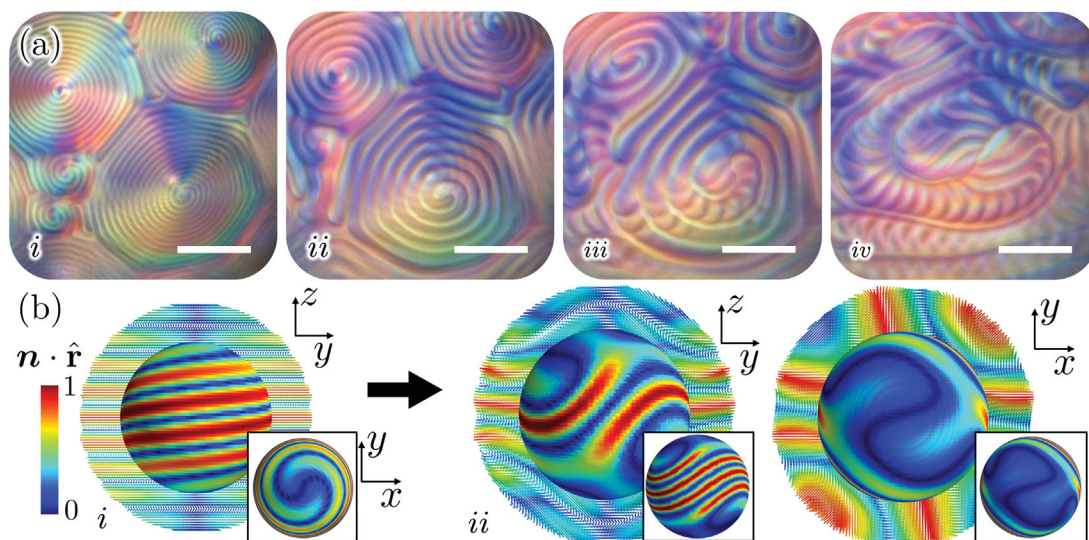


FIG. 13. (a) Cross-polarized micrographs of a thick cholesteric shell in an aqueous solution with 7 mM sodium dodecyl sulfate, 1 wt% polyvinyl alcohol, and 0.1 M sodium chloride that has a focal conic domain texture initially. The pitch is 5  $\mu\text{m}$ . (i)–(iv) The shell is transferred to another similar aqueous solution, but without sodium dodecyl sulfate, and the texture evolves over time. (i),(ii) As the outer interface loses homeotropic anchoring strength with surfactant removal to the surrounding solution, the planar anchoring stripes widen. When the stripes widen to the point of becoming greater than around twice the pitch ( $\sim 10 \mu\text{m}$ ), the planar stripes fill in with perpendicular stripes of a second periodicity that is also around twice the pitch. Scale bars are 25  $\mu\text{m}$ . (b)(i) Simulations of an initially homeotropic cholesteric shell with a 0.18  $\mu\text{m}$  pitch, a 0.84  $\mu\text{m}$  diameter, and a 0.18  $\mu\text{m}$  thickness that has a pitch axis oriented along the  $\hat{z}$  axis. (ii) The shell is minimized under planar anchoring conditions ( $\sim 2 \times 10^{-4} \text{ J/m}^2$ ), resulting in a local energy minimum in which the stripes are partially unwound, with a side view on the left and a top view on the right. Undulations are visible at the poles, where the stripes have unwound. Adapted from M. O. Lavrentovich and Tran, 2020.

plausible that the structure of the stripe instability is influenced by Bouligand’s geometrical arguments. Specifically, the micrograph of Fig. 13(a)(iv) is evocative of the 1984 study by Bouligand and Livolant of cholesteric spherulites (Bouligand and Livolant, 1984). Figure 14 reproduces their illustration describing the origin of double spiraled structures seen in their experiments. A cholesteric with a vertical, unfrustrated pitch axis is drawn with an angled view in Fig. 14(b) and is cut into the shape of a hill. Viewing this hill from the top [Fig. 14(b), top images] uncovers a double spiraled pattern that is filled in with Bouligand arches.

Although this geometrical model hints at the bulk cholesteric arrangement, this description does not account for the periodicity of the orthogonal stripes, which appear to follow an archlike pattern. As with the homeotropic transition, the organization of the cholesteric layers can also be examined through Landau–de Gennes simulations (M. O. Lavrentovich and Tran, 2020). Figure 13(b) depicts a cholesteric shell with a pitch axis oriented along the  $z$  axis. The focal conic domains are slightly stretched at the poles along the  $z$  axis, resulting in greater regions of planar anchoring that are marked in blue by the  $\mathbf{n} \cdot \hat{\mathbf{r}}$  color map. Minimizing this shell under planar anchoring conditions causes the stretched focal conic domains to unwind, generating undulating stripes [blue areas in Fig. 13(b)(ii)] in regions where the planar anchoring is increased, similar to experimental observations shown in Fig. 13(a). Cross sections of the shell after minimization [Fig. 13(b)(ii)] reveal that the orthogonal stripes arise from undulation of the underlying cholesteric layers.

We can build a HH-type model of the planar anchoring transition in cholesteric shells by estimating the energy scales associated with imposing an anchoring that induces a tilt in the existing cholesteric pseudolayers on a local patch of the emulsion surface. As detailed by M. O. Lavrentovich and Tran (2020), the free energy of the cholesteric pseudolayers in a small, flat area of the shell surface can be written in the form given by Eq. (12). Any antagonistic anchoring would tend to reorient the pseudolayers. The associated anchoring energy would have the form of Eq. (16). This anchoring energy induces an undulatory instability (a modulation of  $u$  in a direction perpendicular to the layers) whenever the anchoring strength  $|W| > \pi\sqrt{\bar{K}\bar{B}}$ ; see Eq. (12). Moreover, the wave vector associated with the modulation is  $q_c = (\bar{B}/\bar{K})^{1/4}(\pi/2\ell)^{1/2}$ , with  $\ell$  the size of the deformation region near the droplet surface (typically on the order of the pitch). For the cholesteric shells shown in Fig. 13(a), these heuristic arguments give reasonable estimates for both the critical anchoring strength ( $|W| \approx 10^{-5} \text{ J/m}^2$ ) and the modulation wavelengths ( $2\pi/q_c \sim 10 \mu\text{m}$ ) (M. O. Lavrentovich and Tran, 2020).

For both the planar and homeotropic transitions, the anchoring-induced HH instability arises from local geometrical frustration between the bulk layer arrangement and the prescribed molecular orientation at the interface. Yet the conformation of the resultant stripes differs between the two anchoring transitions. For the transition to homeotropic anchoring, the nucleation of undulated stripes gives a random patterning, with the topologically required nematic defects serving as favorable sites for the initial pitch axis

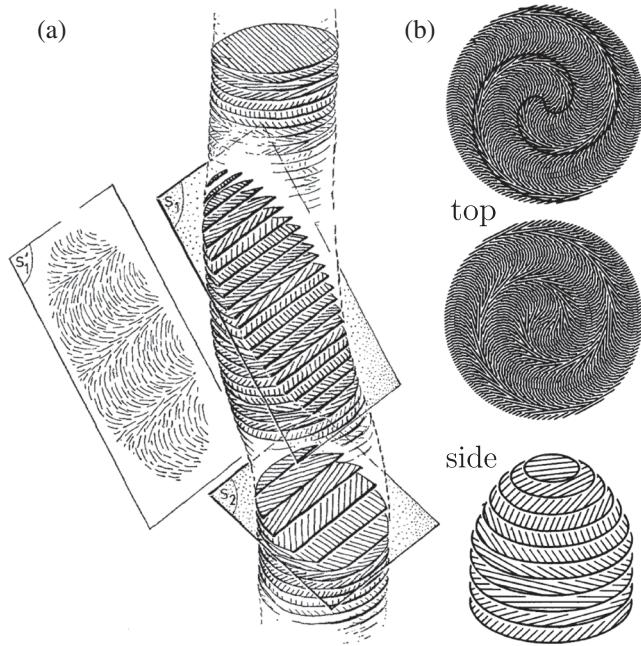


FIG. 14. (a) Schematic of a cholesteric liquid crystal, with its pitch axis oriented vertically. Planes  $S_1$  and  $S_2$  slice into the cholesteric at an angle to the pitch axis. A curving periodic texture, called Bouligand arches, is apparent on the surfaces of the planes. Plane  $S_1'$  simplifies the pattern on plane  $S_1$ , highlighting how Bouligand arches reveal cholesteric ordering of the sliced material. Adapted from Bouligand, Soyer, and Puiseux-Dao, 1968. (b) Schematic of a cholesteric with a vertical pitch axis is cut into a hill-like shape (side view). Viewing the hill from the top reveals Bouligand arches that follow a double spiraled pattern (top view). The double spiraled pattern is emphasized by black lines. Adapted from Bouligand and Livolant, 1984.

reorientation. Thus, for the homeotropic transition the pitch axis is initially radial and tilts to become tangent to the interface. Since all directions away from radial are equivalent, the onset of the stripe instability, i.e., the stripe nucleation, is disordered. For planar transitions, pitch axis reorientation occurs first at the pitch defects, evidenced by the unwinding of focal conic domains, where the pitch axis begins to tilt toward radial. Pitch axis reorientation here is more constrained than for the homeotropic transition. The shortest path for the initially tangent pitch axis to tilt is along the plane orthogonal to the interface that includes the pitch axis. This constraint results in the onset of stripes being perpendicular to, and thus ordered by, the starting stripe pattern set by the initially tangent pitch axis. Note that the presence of topological defects is not necessary for the anchoring-induced instability to occur. Although the defects generated by topological frustration influence the conformation of the stripe instability, the root cause of the stripe instability remains a local geometrical incompatibility between the bulk cholesteric layers and the anchoring condition.

## VI. SMECTIC SHELLS

In Sec. V, we introduced the concept of the HH instability in the context of cholesteric shells, where the instability arises as

a way of reconciling antagonistic boundary conditions. This is one of the multiple ways in which geometrical frustration can perturb the structure of a layered system embedded in a spherical shell. Local curvature and global topological constraints can also induce strain in the layers and set off an undulating response, exemplified by smectic shells with planar boundary conditions.

### A. Planar smectic shells in experiments

The first study of smectic shells involved bringing 4'-octyl-4-biphenylcarbonitrile (8CB) in a planar, spherical shell close to the nematic-smectic phase transition temperature, where the elastic ratio  $K_3/K_1$  diverges (Lopez-Leon, Fernandez-Nieves *et al.*, 2011; Liang *et al.*, 2012). This operation entails the formation of a bend-free state in which the nematic defects relocate to the equator. At the transition, a periodic pattern forms on the shell surface. In Figs. 15(a) and 15(b) we show cross-polarized micrographs of the lower and upper hemispheres of the same shell. We see four  $+1/2$  defects required by topology and inherited from the nematic state, as described in Sec. V.A. Here the four defects are equally spaced along the equator. Additionally, two sets of longitudinal stripes divide the shell into crescent domains. The first set of stripes connects defects ③ and ④ with semicircles that run along the upper hemisphere of the shell, while the second set of stripes connects defects ① and ② with semicircles that run along the lower hemisphere of the shell. The first set of stripes is visible on the upper hemisphere; see the highlighted crescent domain in Fig. 15(b). The second set of stripes is also visible in Fig. 15(a), especially in the top half of the photograph; see the inset in Fig. 15(a). This second set of stripes is faint because the bottom part of the shell is thinner than the top. The two sets of lines in each hemisphere are orthogonal to each other.

This stripe texture results from an intricate interplay of the curvature of the shell, the local energetic constraint of equally spaced layers, global topological constraints, and anchoring conditions. To understand this, first consider the limit of vanishing shell thickness where there is no frustration of the smectic layers between the inner and outer surfaces, as shown in Fig. 15(c). The condition of equal spacing results in the layers becoming lines of latitude (Blanc and Kleman, 2001). The director aligns along the lines of longitude, tracing out geodesics [depicted as dashed lines in Figs. 15(c)–15(f)] (Santangelo *et al.*, 2007; Kamien *et al.*, 2009). In this situation, there are two  $+1$  defects at the two poles. However, each  $+1$  defect can be split in half, and the upper and lower hemispheres can be rotated independently, as shown in Figs. 15(c) and 15(d) (Blanc and Kleman, 2001; Bates, 2008; Shin, Bowick, and Xing, 2008). The four  $+1/2$  defects resulting from this simple surgery sit on a great circle of the sphere [Fig. 15(e)]. The energy difference between the state with two  $+1$  defects and those with four  $+1/2$  defects comes from the defect core energies and is negligible for large system sizes. While there is a single state for two  $+1$  defects, there is an infinite number of states with four  $+1/2$  defects. Thus, generically we expect to see four  $+1/2$  defects in the smectic shell, lying along a great circle. Further minimization of the director energy yields a rotation angle of  $\pi/2$ ,

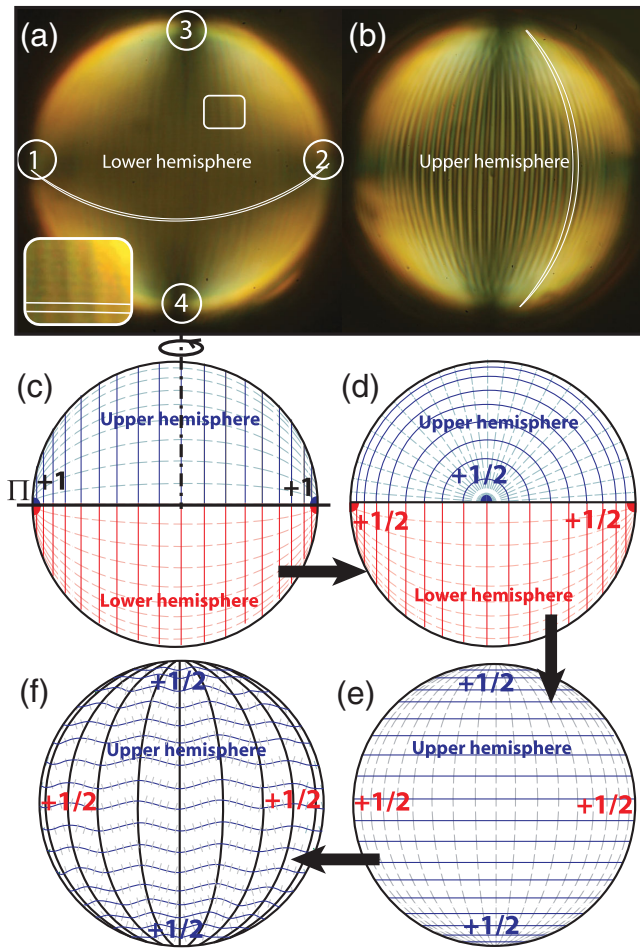


FIG. 15. Cross-polarized images of a smectic shell of radius  $R = 98 \mu\text{m}$  and mean thickness  $h = 1.96 \mu\text{m}$ . (a) The birefringent texture at the bottom of the shell is different from (b) the birefringent texture at the top of the shell due to the different thickness of these two regions from a density mismatch between the inner water phase and the smectic. Inset: stripes on the lower hemisphere after image enhancement. Two stripes are outlined at the bottom of the inset as a guide for the eye. (c) Schematic of director arrangements in a two-dimensional smectic shell. Theory predicts a configuration with two  $s = +1$  defects organized in a bipolar fashion. (d) This configuration is energetically equivalent to any other one that results from splitting the bipolar shell into two halves using a plane  $\Pi$  that contains the two  $s = +1$  defects and then rotating one half with respect to the other one by an angle that can have any value. (e) All the configurations resulting from this transformation have four  $s = +1/2$  defects lying on a great circle. (f) This smooth texture is only a first-order description of the configuration observed experimentally, where a periodic modulation of the smectic layers is observed.

as depicted in Fig. 15(d). This configuration maximizes the distances between the  $+1/2$  defects.

In experiments, however, the shells are three dimensional and have a thickness that leads to a frustration between the surface anchoring and the layer spacing. This frustration involves creating dislocations, layer dilation, or anchoring violation due to the different curvatures of the inner and outer boundaries (Lopez-Leon *et al.*, 2012). In a configuration without dislocations, imposing planar anchoring at the

boundaries necessarily implies layer dilation. Again, this frustration is precisely the type that leads to the HH mechanism: the smooth texture sketched in Fig. 15(e) is disturbed by the presence of a set of periodic lines and the rapid variation of  $\mathbf{n}$  across these lines. By examining the birefringent texture of the experimental shells under rotation, it has been observed that  $\mathbf{n}$  is tilted by an almost constant angle  $\pm\beta$  [by a few degrees for the shell in Fig. 15(a)] with respect to the two-dimensional director field sketched in Fig. 15(e). Since  $\mathbf{n}$  is tilted in opposite directions in two adjacent crescent domains, the visible lines that separate them roughly correspond to symmetric curvature walls (Blanc and Kleman, 1999). The sawtooth periodic undulation of the smectic layers schematically represented in Fig. 15(f) is yet another HH mechanism pattern observed at large strains and is connected to the three-dimensional nature of the shells.

A zero-strain, smectic texture is possible in thick smectic shells provided that the director tilts away from the outer shell surface, incurring an anchoring penalty; see Lopez-Leon *et al.* (2012). A first approach to relax this additional surface energy was developed by Manyuhina and Bowick (2015). They examined the influence of a finite anchoring strength  $W$  on a nematic shell texture with large bending modulus  $K_3 \gg K_1$  that is expected to mimic the smectic behavior. Within the frame of nematic elasticity, they adopted a perturbative approach for thick shells, starting with the ideal two-dimensional structure in Fig. 15(d), while imposing infinitely strong anchoring at the shell's inner surface, as well as allowing the director to tilt with respect to the tangent plane and to vary along the shell thickness. Manyuhina and Bowick proposed a plausible criterion for the onset of director tilting, which should occur when the shell's mean curvature  $\kappa = 1/R$  becomes larger than  $W/K_3$ . Moreover, they showed that the axisymmetric texture is unstable beyond this same threshold, where a spontaneous herringbone texture develops.

This first approach can be complemented with geometrical considerations based on the elasticity of smectic layers, which is more in line with the HH model. Indeed, the experimental results suggest that, in shells with strong planar anchoring, the strain associated to layer dilation  $\gamma$  is released by undulations of the smectic layers related to a mechanical HH mechanism (Lopez-Leon, Fernandez-Nieves *et al.*, 2011).

## B. Strain from boundary curvature

Before delving into the specifics of the HH mechanism in smectic shells, we take a step back and consider more generally how boundary curvature can strain smectic layers. Consider an interface with some spatially varying surface normal  $\hat{\mathbf{v}} \equiv \hat{\mathbf{v}}(x, y)$ , written in terms of the height field  $h$  as  $\hat{\mathbf{v}} = (-\partial_x h, -\partial_y h, 1)/\sqrt{1 + (\nabla h)^2}$ , as depicted schematically in Fig. 16. For illustrative purposes, consider a simple surface shape  $h(x, y) = d + (2\kappa)^{-1}[\sqrt{1 - (2\kappa y)^2} - 1]$ , where  $\kappa$  is the mean curvature of the surface and  $d$  is the film thickness at  $y = 0$ . For  $|y| \ll 1/\kappa$  the surface has a parabolic profile  $h \approx d - \kappa y^2$  along the  $y$  direction. Therefore, near the maximum of the parabola we expand in powers of  $y$  and consider the interaction between the surface and the smectic layers in the bulk.

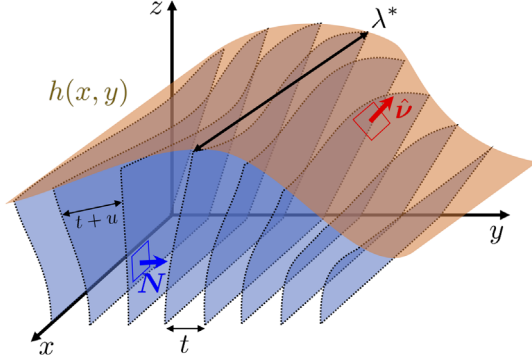


FIG. 16. A schematic of an interface-induced instability in which a curved, deformable interface (orange) described by a height field  $h(x, y)$  induces undulations with a characteristic wavelength  $\lambda^*$  in the blue layered system. At the interface, the layer normals  $N$  prefer to be perpendicular to the interface normal  $\hat{\nu}$ . As described in the main text, a curved interface like this will dilate or compress the layers relative to their preferred spacing  $t$ . The resultant strain may be relieved via layer buckling in a perpendicular direction.

Using the phase field  $\phi \equiv \phi(\mathbf{x})$ , the layered structure is recovered by solving  $\phi = na$  for  $\mathbf{x}$ , where  $n \in \mathbb{Z}$  labels the layer and  $a$  is the layer spacing; see Fig. 16. Suppose that in an unperturbed configuration the layers are stacked along the  $y$  direction such that  $\phi = y$ . The layer normal is therefore  $N = \nabla\phi/|\nabla\phi| = \hat{y}$ . If we have perturbations in the layer spacing, this may be captured by a small deformation:  $\phi = y + \delta\phi$ . In this case, the layers are still roughly stacked along the  $y$  direction (as sketched in Fig. 16), but with deviations described by  $\delta\phi$ . Assuming planar boundary conditions at the interface that prefer an orientation  $N \perp \hat{\nu}$ , the surface free energy  $f_s$  at the interface for small  $\delta\phi$  and small  $\nabla h$  is given by

$$\begin{aligned} f_s &\approx \frac{W}{2} \int dx dy (\hat{\nu} \cdot N)^2|_{z=d} \\ &\approx \frac{W}{2} \int dx dy [\partial_z(\delta\phi) - \partial_y h]^2|_{z=d}, \end{aligned} \quad (17)$$

where  $W$  is the anchoring strength. We have substituted  $\hat{\nu} \approx \hat{z} - \nabla h$  for the interface normal and  $N \approx \hat{y} + \nabla(\delta\phi)$  for the layer normal. This surface free energy is minimized for  $\delta\phi(y, z) = -2\kappa yz$ , representing a layer dilation with increasing  $z$ . Therefore, at the top edge of the film, the layer spacing experiences a dilating strain  $\gamma \approx 2\kappa d$  (relative to the spacing on the bottom of the film), with  $d$  the film thickness at  $y = 0$ . This dilation will be energetically costly due to the bulk layer compression elasticity. The system may relieve this energetic cost in a variety of ways, including disrupting the layer structure via dislocations or developing layer undulations, as illustrated for a generic curved surface in Fig. 16. There one sees layers mostly stacked along the  $\hat{y}$  direction, but undulating along  $\hat{x}$  to relieve the strain imposed by the curvature of the interface.

The details of the layer relaxation are generally complex since the undulations will coexist with defects and the details of their interactions are subtle. Analogous issues are seen in

smectic systems confined to wedge geometries (Bartolino and Durand, 1977a). Yet we can make a basic estimate of the critical strain  $\gamma^*$  (applied along the layer normal  $N$ ) required to induce an undulation.

First, note that the layer compression and bending moduli  $K$  and  $B$ , respectively, combine to yield a characteristic length  $\lambda = \sqrt{K/B}$ , which governs the size of the deformations. This length scale is again the smectic penetration depth, first introduced in Sec. III.B. Second, the undulation instability occurs when the layer strain  $\gamma$  exceeds a critical value  $\gamma^* \approx 2\pi\lambda/\ell$  (or, equivalently, if the layer stress exceeds  $B\gamma^*$ ), with  $\ell$  a characteristic sample size in the direction of the applied strain. In the case of our simple example of an interface  $h(x, y) \approx d - \kappa y^2$  with the layer normals along the  $\hat{y}$  direction and the dilation induced by an interface curvature,  $\ell$  would be the extent of the bent region in the  $\hat{y}$  direction. However, the critical strain would also depend on the anchoring strength  $W$  and would generally have a complicated form. Alternatively, if the layers are arranged such that  $N \parallel \hat{\nu}$  and are dilated by a strain along that same direction (similar to the classic instability shown in Fig. 1), then  $\ell$  would be the film thickness  $d$  and  $\gamma^* = 2\pi\lambda/d$ , as expected. Furthermore, depending on the nature of the mechanical deformation, there may be some modifications to  $\gamma^*$  (Napoli and Nobili, 2009). For instance, the surface tension at a fluid interface may modify  $\lambda$ , introducing an additional length  $\lambda \rightarrow \lambda + \lambda_s$ , with  $\lambda_s \sim \sigma/B$  and  $\sigma$  the surface tension (Williams, 1995). Nevertheless, the basic scaling  $\gamma^* \sim \lambda/\ell$  is predictive in a wide range of cases in which this mechanical instability is observed.

Note that the critical strain  $\gamma^*$  may be connected to the usual HH critical field  $H_c$  since the strain  $\gamma$  introduces an energy penalty due to the compression term being proportional to  $B$ . The coefficient  $|\chi_a|H_c^2$  is completely analogous to the stress  $\gamma B$  (Delaye, Ribotta, and Durand, 1973; Fukuda and Onuki, 1995). The critical field then is directly related to  $\gamma^*$  as

$$|\chi_a|H_c^2 = \gamma^* B = \frac{2\pi K}{\lambda\ell}, \quad (18)$$

which reduces to the  $\gamma^* = 2\pi\lambda/\ell$  result. The connection to the usual HH scenario (described in Sec. III.A.1) also allows us to extract the characteristic wavelength  $\lambda^*$  of the undulations, given by

$$\lambda^* = 2\sqrt{\pi\lambda\ell}, \quad (19)$$

which is consistent with Eq. (11). The mechanism has the same character in smectics and cholesterics (Clark and Meyer, 1973), and the discussion in Sec. III.A.1 can be directly mapped to these strain-induced undulations.

The strain  $\gamma$  may be imposed externally due to a particular confinement, applied force, or thermal expansion. If the strain occurs near a curved interface, the interface geometry will modify the character of the undulations. For instance, in a smectic with concentric cylindrical layers, a layer dilation induces an undulation along the cylinder axis. Unlike a flat geometry, the curvature makes the onset of the undulations

more complex, with the shape of the layer playing an important role (de Gennes and Pincus, 1976).

Now that we understand how boundary curvature can strain smectic layers enough to trigger the HH mechanism, we return to smectics in a shell geometry. In the following, we consider the simpler case of a cylindrical shell and build on that to interpret the spherical shell data.

### C. Cylindrical smectic shells

Consider a smectic slab confined between two cylinders of radii  $R$  and  $R_0 = R + h$ , with  $h \ll R$  and strong planar anchoring; i.e.,  $\mathbf{n}$  lies parallel to the inner and outer cylinders along  $\hat{\mathbf{e}}_\theta$  [Fig. 17(a)]. The equilibrium layer thickness is  $a$ , and the appropriate smectic free energy is given by Eq. (3), with  $N$  the layer normal, which maps to  $\mathbf{n}$  for smectic-A phases, and  $1 - |\nabla\phi|^{-1} = 1 - d/a$ , where  $d$  is the actual layer thickness. If the layers were dilated but not curved [ $\nabla \cdot \mathbf{n} = 0$ , as schematically represented in Fig. 17(a)], their thickness would increase as  $d(r) = rc_R a/R$ , where  $c_R$  is the layer thickness at the inner boundary. Note that the constant  $c_R$  is close to 1 and can be chosen to minimize the energy for the bend-free state derived from Eq. (3). For  $h \ll R$ , we have  $c_R \approx 1 - h/2R$ , with a smectic free energy per unit length of  $f_e \approx \pi B h^3/12R$ .

Even with an infinite anchoring strength, the elastic energy decreases when we consider a more general scenario, where the smectic layers are allowed to curve into an **S** shape to maintain the layer spacing, as depicted in Fig. 17(b). Treating the system as two dimensional with no variation along the cylinder, we consider the axially symmetric director field  $\mathbf{n}(r, \theta) = \cos \vartheta(r) \hat{\mathbf{e}}_r + \sin \vartheta(r) \hat{\mathbf{e}}_\theta$ , where  $\vartheta(r)$  is the tilt of the director and the normal of the layers with respect to the unit radial vector  $\hat{\mathbf{e}}_r$  [Fig. 17(b)]. The width of the layers is  $d(r) = \sin \vartheta(r) rc_R a/R$  [Fig. 17(b)], and the free energy per unit length is

$$f_e = \frac{B}{2} \left( 1 - \frac{c_R r \sin \vartheta(r)}{R} \right)^2 + \frac{K}{2} (\nabla \cdot \mathbf{n})^2. \quad (20)$$

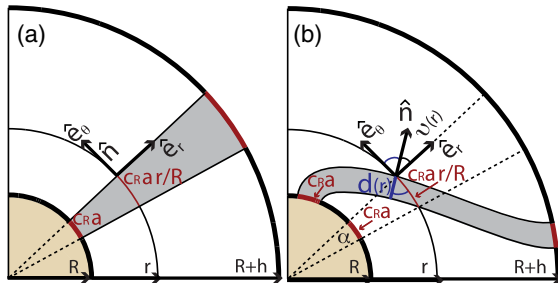


FIG. 17. Schematics of a smectic confined between two cylinders of radii  $R$  and  $R + h$ . The anchoring is planar on the confining boundaries. (a) In the absence of dislocations, a radial texture necessarily induces some dilation in the thickness of a smectic layer (gray shaded region). (b) The absence of dilation in the bulk implies that the “orthoradial” thickness of a layer  $d$  varies with the radial coordinate  $r$ . However, some dilation is necessarily ejected to the outer surface.

To solve for the tilt angle,  $\vartheta$ , we write the Euler-Lagrange equation, which reads

$$\frac{d^2 \vartheta}{dr^2} = \frac{c_R^2 r^4 - R^2 \lambda^2 - c_R r^3 R / \sin \vartheta}{r^2 R^2 \lambda^2 \tan \vartheta} - \frac{d\vartheta}{dr} \left( \frac{1}{r} + \frac{d\vartheta}{dr} \frac{1}{\tan \vartheta} \right), \quad (21)$$

where we impose the boundary conditions  $\vartheta(R) = \vartheta(R + h) = \pi/2$  and  $\lambda$  is again the smectic penetration depth  $\lambda = \sqrt{K/B}$ . The tilt angle  $\vartheta(r)$  and the shape of layers can then be obtained by numerically solving Eq. (21) using standard two point boundary value methods and optimizing the resulting elastic energy  $f_e(c_R)$  as a function of  $c_R$ . Figure 18(a) shows the numerical solution  $\vartheta(r)$  for  $R = 100 \mu\text{m}$  and  $h = 2 \mu\text{m}$ , which are typical values for the shell radius and thickness of the experimental shells. The relative dilation of the layers  $d/a$  and the free energy density  $f_e(r)$  of the ground-state configuration are shown in Fig. 18. Three different regions can be distinguished: the layers are slightly compressed in the thin inner region (highlighted in blue), while dilation is mostly confined to the outer surface (highlighted in red). The dilation nearly vanishes in the yellow region between the two boundary layers.

The fact that dilation is expelled from the bulk is a well-known phenomenon for layered systems (Blanc and Kleman, 1999). Indeed, comparing the two terms of Eq. (3) reveals that dilation can be present only in regions where the curvature of the layers ( $\nabla \cdot \mathbf{n}$ ) is of the order of  $\lambda^{-1}$ , i.e., where the layers rapidly reorient, or near the common focal surfaces of a set of equidistant layers. That is why the macroscopic textures of layered systems can be described by an extended geometrical description based on a combination of domains with

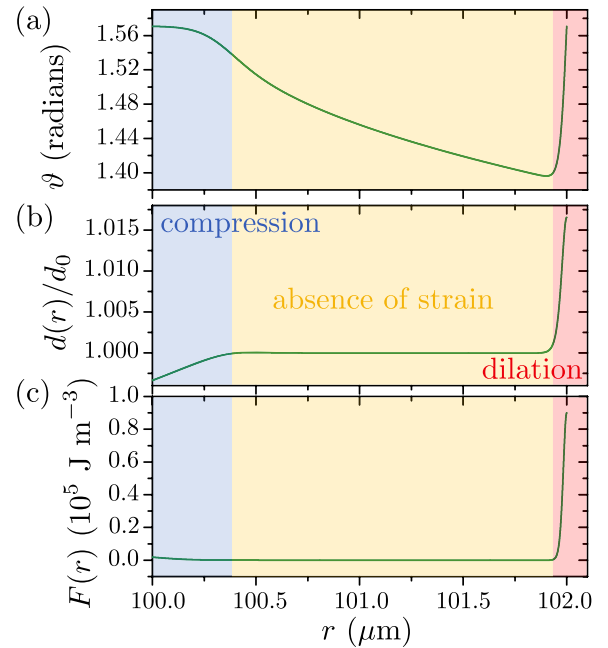


FIG. 18. (a) Tilt, (b) relative dilation, and (c) free energy density of a smectic layer as a function of the radial coordinate  $r$  for a shell of  $2 \mu\text{m}$  thickness and inner radius  $R = 100 \mu\text{m}$ , using  $\lambda = 3 \text{ nm}$ .

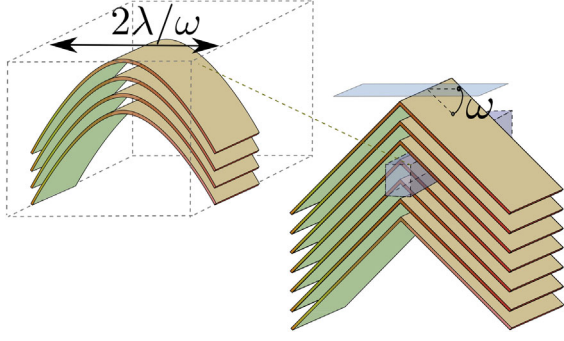


FIG. 19. Schematic of smectic layers with curvature walls separating domains in which  $\mathbf{n}$  displays opposite orientations  $\pm\omega$ . If  $\omega$  is not too high, the smectic layers undergo a continuous bend across the wall.

equidistant layers separated by curvature walls of varying shapes, as illustrated in Fig. 19 (Blanc and Kleman, 1999). If the “misorientation” angle  $2\omega$  of a curvature wall is not too high, the layers remain continuous. The width of a wall is thereby  $2\lambda/\omega$ , and its free energy per unit area is

$$f_w \approx \frac{2K}{\lambda} (\tan \omega - \omega) \approx \frac{2K\omega^3}{3\lambda}. \quad (22)$$

In Eq. (22) the geometrical construction driven by a strong planar anchoring at the inner surface yields  $\sin \vartheta(r) = R/r$  in the bulk and a tilt  $\omega_0 = \pi/2 - \vartheta(R+h) \approx \sqrt{2h/R}$  at the outer cylinder. The dilation is thus expelled in a curvature wall that contains most of the elastic energy per unit length,

$$f_e = \frac{4K\pi h}{3\lambda} \sqrt{\frac{2h}{R}}. \quad (23)$$

With this two-dimensional approach, dilation is confined to the neighborhood of the outer cylinder. However, three-dimensional distortions of the director field are expected to further lower the resulting elastic energy. For example, with degenerate planar anchoring on both cylinders, the elastic energy can be entirely relaxed when the director is oriented along the other principal curvature direction, where curvature is null (Fig. 20).

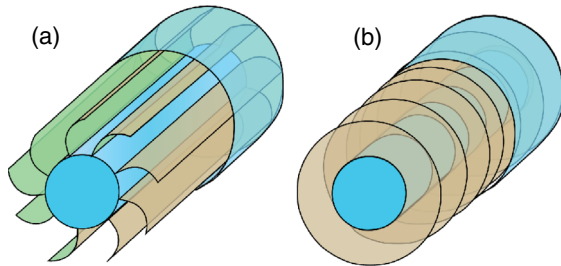


FIG. 20. Schematic of smectic layer arrangements in a cylindrical shell. In three dimensions, the distortion of the smectic layers is efficiently relaxed by an overall rotation of the layers, which is allowable when the anchoring is planar degenerate.

#### D. Spherical smectic shells

Geometrical frustration is even more evident in spherical smectic shells of finite thickness. Contrary to the cylindrical case considered in Sec. VI C, the elastic energy cannot be globally relaxed in a spherical shell. Unlike on a cylinder, which bends in only one direction, the two principal curvatures on a sphere are nonvanishing (and equal). Thus, the geometrical strain remains, regardless of the layer orientation with respect to the surface.

We first examine the vanishing thickness limit shown in Fig. 15(c). Such an ideal smectic sphere has two +1 defects located at the north and south poles, and the surface director is given by  $\mathbf{n} = \hat{\mathbf{e}}_\theta$ , written with the usual spherical coordinates  $r, \theta$ , and  $\varphi$  and the corresponding unit vectors  $\hat{\mathbf{e}}_r, \hat{\mathbf{e}}_\theta$ , and  $\hat{\mathbf{e}}_\varphi$ . As in the cylindrical case shown in Fig. 17(b), a geometrical construction from the inner sphere of radius  $R$  for shells with finite thickness is also possible, giving rise to a director field  $\mathbf{n} = \sin \vartheta(r) \hat{\mathbf{e}}_\theta \pm \cos \vartheta(r) \hat{\mathbf{e}}_r$ , where  $\sin \vartheta(r) = R/r$ . The resulting angular misfit of the smectic layer tilt at the outer surface of a shell of thickness  $h$  is still  $\omega_0 = \arccos R/(R+h) \approx \sqrt{2h/R}$ , as it was in the cylindrical shell. Therefore, the resulting half-curvature wall located at the outer sphere has an elastic energy

$$F_e \approx \frac{4\pi(R+h)^2 K}{3\lambda} \omega_0^3. \quad (24)$$

However, this azimuthally homogeneous geometry is not optimal, since it still has significant elastic distortion with high energetic costs. Taking inspiration from the experimental images of Figs. 15(a) and 15(b), we now consider other textures where the smectic layers are no longer rotationally invariant around the  $z$  axis. These textures can be geometrically constructed, and we show here that they have lower elastic energies than in the homogeneous case.

Consider the texture sketched in Fig. 21(a). This texture is one of the simplest geometric constructions that shares several features with the experimental shells shown in Fig. 15. It consists of pairs of crescent domains repeated along the azimuthal angle  $\varphi$  with a period  $\Delta\varphi = 4\chi$ . The crescent domains are separated by  $\pi/\chi$  curvature walls, denoted as  $\Pi_\chi$  in Fig. 21(c), which account for the layers roughly tilted by an angle  $\beta$  with respect to the latitude lines. The elementary texture in  $-\chi \leq \varphi \leq \chi$  is issued from a director field defined at  $\varphi = 0$  (arbitrarily chosen) for  $R \leq r \leq R+h$ :

$$\mathbf{n}(r, \theta, \varphi = 0) = \frac{R \cos \beta}{r} \hat{\mathbf{e}}_\theta + \sqrt{1 - \frac{R^2 \cos^2 \beta}{r^2}} \hat{\mathbf{e}}_\varphi. \quad (25)$$

This field shows several attractive features at  $\varphi = 0$ . (See the Appendix for additional details.) First, this construction exactly ensures planar anchoring on the inner and outer spheres. Second, the director field’s dependence on  $r$  maintains that the smectic layers are fully perpendicular to the spherical shell’s surfaces (Lopez-Leon *et al.*, 2012) at the  $\varphi = 0$  meridian. The cross-section width  $w$  of the smectic layers in the plane  $\varphi = 0$  increases with  $r$  [Fig. 21(c), blue plane], which is similar to Fig. 17(a) for the cylindrical case.

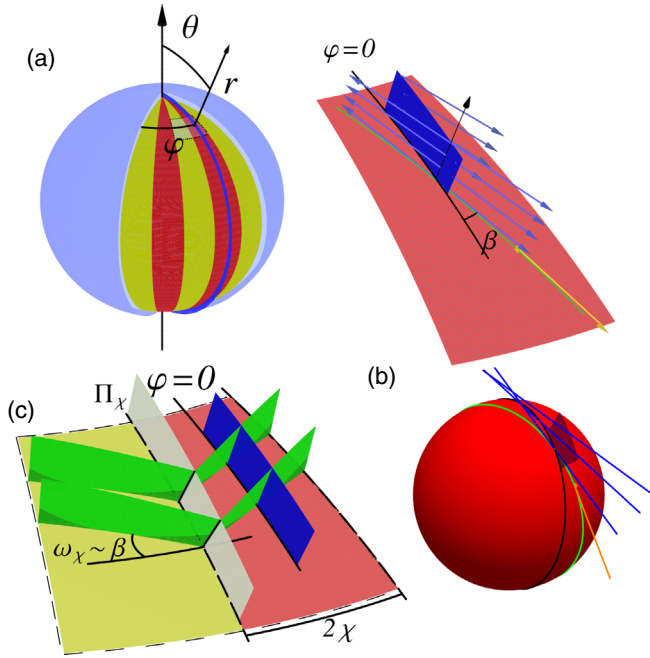


FIG. 21. (a) Spherical coordinates used to describe the smectic textures of a shell. (b) The director field  $\mathbf{n}(r, \theta, \varphi = 0)$  defined on the  $\varphi = 0$  plane is used to construct the director field in its vicinity (blue lines). The region of the shell near the inner surface is complemented with a set of lines (yellow) tangent to each great circle (denoted as a green line) issued from  $\mathbf{n}(r = R, \theta, \varphi = 0)$ . For clarity, the same construction is later shown for an oversized shell. (c) The field of normals thus constructed defines parallel smectic layers (green surfaces) that are devoid of defects in a limited neighborhood  $-\chi < \varphi < \chi$ , but the process can be iterated periodically along the azimuthal direction (shown here for the region  $-3\chi < \varphi < -\chi$ ) at the cost of additional curvature walls  $\Pi_\chi$  of tilt misorientation  $\omega_\chi$ . The latter tilt misorientation remains close to  $\beta$  in following our experimental conditions.

Yet the actual thickness of the layers  $w\hat{\mathbf{e}}_\theta \cdot \mathbf{n}$  is constant with  $r$ . (See Fig. 37 in the Appendix.)

Is a neighboring set of parallel layers compatible with the smectic-A elastic field in a spherical shell? How far can the layers extend along  $\varphi$  without defects? To answer these questions, first note that the director field unambiguously defines straight lines made of the smectic layer normals in a neighborhood of  $\varphi = 0$ , as long as  $\beta \neq 0$ ; see the Appendix. These lines defining the smectic layer normals can remain straight in a significant part of the shell thickness, but not within a region above the inner sphere, beyond some critical  $r_c$  and  $\varphi_c$ . In this subregion, to accommodate the spherical curvature the set of straight layer normals has to be adjusted to follow tangents of great circles in the sphere. These tangent lines are the ones issued from  $(R, \theta, 0)$ , tangent to the director  $\mathbf{n}(R, \theta, 0)$ ; see Fig. 21(b). Since great circles are geodesics of the sphere, this construction ensures that the corresponding layers remain parallel to each other while being perpendicular to the inner sphere (Blanc and Kleman, 2001).

The field defined from  $\varphi = 0$  depends solely on the angle  $\beta$ . However, the field cannot be extended to the entire shell without additional defects. The closest singularity point in the azimuthal direction can be analytically determined; see

the Appendix. It has the following spherical coordinates:  $r_c$ ,  $\pi/2$ , and  $\varphi_c$ , with  $r_c = R/\cos\beta$  and  $\sin\varphi_c = \sin^2\beta$ . The bulk elastic energy diverges at such singularities. These singularities can only be safely neglected if the crescent angle  $\chi$  is upper bounded by  $\varphi_c$ .

Taking this constraint into account, we consider the energy of this entire geometric construction as a function of two free parameters  $\beta$  and  $\chi$ . The total energy  $F_T$  accounts for the half-curvature walls present at the outer sphere, as well as for the  $\Pi_\chi$  walls between the crescent domains.  $F_T$  can be computed using the values of both the misfit angles at the outer shell surface and the angles of the  $\Pi_\chi$  walls using Eq. (22). The tilt of the layers  $\omega_e$  at the outer surface is zero at  $\varphi = 0$  (by construction) and increases with  $\varphi$ . This construction thereby favors low values of  $\chi$ , resulting in narrow crescent domains. However, narrow crescent domains also require an increasing number of  $\Pi_\chi$  walls (whose misfit angle  $\omega_\chi \sim \beta$  depends only weakly on  $\chi$ ). At a given  $\beta$  value, the total energy  $F_T$  therefore decreases with  $\chi$ , which tends to favor  $\chi \sim \varphi_c$ .

For the experimental values  $R$  and  $h$  of the shells that we examined, the minimization of  $F_T(\beta, \chi)$  shows a large reduction in the elastic energy compared to Eq. (24); see Fig. 40 in the Appendix. Moreover, we can obtain from our experiments the period and amplitude of the smectic texture, which are highly dependent on the shell thickness. As the shell becomes thicker, the angular period decreases and the wavelength of the undulations increases, resulting in fewer crescent domains. This effect can be qualitatively seen in Figs. 22(a)–22(c), where the number of crescent domains dividing a shell decreases as the normalized thickness  $h/R$  increases. Additionally, the tilt angle  $\beta$  inside the domains concomitantly increases with the thickness. Figure 22(d) shows the evolution of these parameters as a function of the normalized thickness  $h/R$ . The experimental measurements compare well with the numerical values obtained by the minimization of  $F_T(\beta, \chi)$ .

Note finally that these geometric considerations are appropriate for studying the ground state of a thick smectic shell for which  $h/R > \gamma^*$  is much above the critical strain to induce the initial mechanical HH instability. It would also be interesting to study thin shells and to observe the onset of the instability. The wavelength  $\lambda^*$  of the initial instability should be given by Eq. (19). For example, at the equator the relevant length scale over which the mechanical deformation occurs is simply the shell circumference  $2\pi R$ , so we would expect  $\lambda^* \approx 5 \mu\text{m}$  for the  $\lambda \approx 30 \text{ \AA}$  layer spacing of 8CB confined to a shell with radius  $R = 100 \mu\text{m}$ , for example. This is consistent with the spacing of the initial curvature walls; see Fig. 22(a).

In addition to the quantitative changes observed for the amplitude and period of the instability, a further increase of the shell thickness entails deeper structural changes. In thin shells, only the primary curvature walls previously considered can be distinguished, and the modulation is simple [Fig. 22(a)]. However, in thicker shells primary curvature walls with a large tilt angle ( $\beta > 10^\circ$ ) are filled in with secondary curvature walls having a few degrees of tilt to form a herringbone texture [Fig. 22(b)], and the secondary curvature walls can be further patterned by tertiary curvature walls with increasing shell

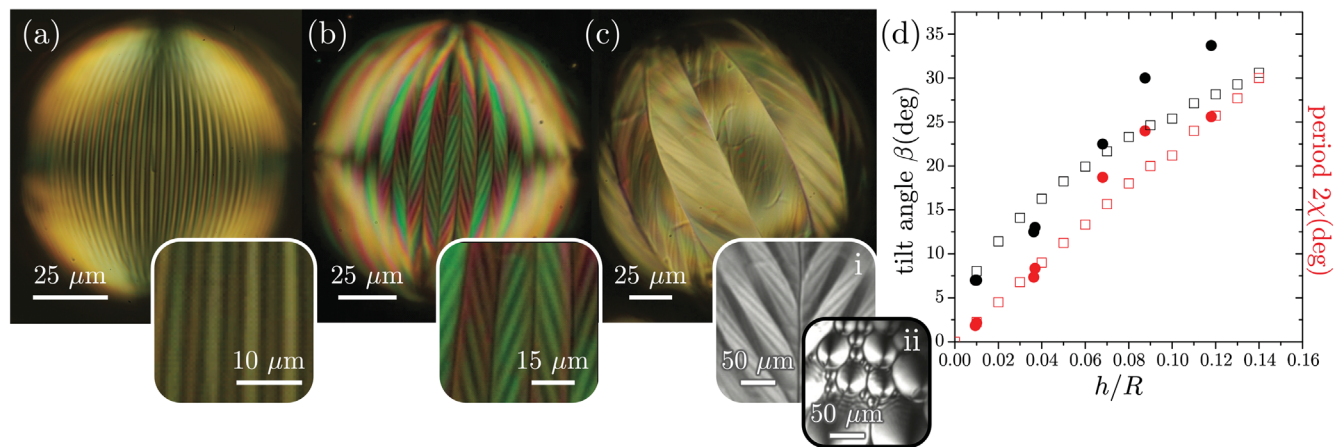


FIG. 22. Effect of the shell thickness in the smectic texture. (a)–(c) Cross-polarized images of smectic shells with a normalized mean thickness  $h/R = 0.020, 0.036,$  and  $0.145,$  respectively. The focus is set on the top of the shell (the thickest region). The insets highlight (a) primary curvature walls ( $h/R = 0.020$ ), (b) secondary curvature walls ( $h/R = 0.036$ ), (c)(i) tertiary curvature walls ( $h/R = 0.145$ ), and (c)(ii) focal conics ( $h/R \approx 1$ ) in smectic shells. (d) Evolution of the angular width of the crescent domains  $2\chi$  and the tilt of the layers  $\beta$  of a smectic shell as a function of its relative thickness  $h/R$ . The experimental points (filled circles) are compared to the results of the minimization of  $F_T(\beta, \chi)$  (empty squares).

thickness [Fig. 22(c)]. Observations of the light extinction between crossed polarizers show that each set of walls is roughly perpendicular to the average orientation of the modulated layers. In thick shells, this hierarchical organization is broken and is replaced by a complex texture made of focal conic domains [Fig. 22(c)(ii)] reminiscent of the ones observed in large single spherical droplets with planar anchoring (Fournier and Durand, 1991; Blanc, 2001; Blanc and Kleman, 2001).

The appearance of the secondary and tertiary patterns in thick shells can be qualitatively understood in the previously discussed geometrical framework. After the first instability, the tilt  $\omega_e$  of the layers at the outer spheres has strongly decreased but is almost nowhere null. The layers are roughly tilted with an angle  $\pm\beta_1$  with respect to the latitude lines. Iterating the process with smaller angles  $\beta_2$  allows for the decrease of  $\omega_e$  once again, at the cost of additional curvature walls of smaller energy. The dilation that was localized only at the outer sphere in the rotational invariant construction is then strongly reduced, while a part of it is redistributed in the entire shell in the form of misorientation walls.

The smectic layers, antagonized by the system's spherical geometry, form periodic structures to maintain their preferred spacing, patterning the shell with curvature walls. The wavelength of these structures increases, and they are filled in by hierarchical patterns with increasing shell thickness, similar in spirit to the undulations observed in planar anchoring transitions of cholesteric shells. The incompatibility of the shell curvature with the smectic layers and the emergent, periodic textures that result exemplify how geometrical frustration is at the core of the HH mechanism.

## VII. OTHER CAUSES OF THE HH MECHANISM

The liquid crystal shells examined in this review underwent the HH instability due to frustration from topological constraints, changes in anchoring conditions, and boundary

curvature. Other systems have also been found to demonstrate different sources of frustration, including layer spacing changes due to phase transitions and sample thickness incompatibility with the layer spacing, which can be described by the classic strain response of HH. Before reviewing other phenomena that fall into the HH umbrella, we note that there are other possible contributions to the HH mechanism in lamellar systems.

A prominent example is the work of Loudet *et al.* (2011) on smectic- $C^*$  films. Recall that, unlike the smectic- $A$  phase, a smectic- $C$  phase has its nematic director canted at a nonzero angle with the layer normal, and the projection of the director onto the plane of the layers is referred to as the  $\mathbf{c}$  director. Finally, a smectic- $C^*$  phase has the same geometry as smectic- $C$  on each layer, but because of intrinsic chirality the  $\mathbf{c}$  director rotates from layer to layer. The period of the  $\mathbf{c}$  rotation is typically much longer than the period of the smectic layers and will not alter the ensuing discussion (Meyer *et al.*, 1975; Selmi *et al.*, 2017). A geometrical mismatch occurs at the smectic- $A$  to smectic- $C$  transition, where the molecules tilt relative to the smectic layer normal, thereby decreasing the layer thickness. Indeed, in thin films of the smectic- $C$  phase, the meniscus exhibited stripes that appeared to correlate to the interface shape, and Loudet *et al.* (2011) hypothesized that these structures were the result of the HH instability. The bright-field image in Fig. 23(a) shows the meniscus of a compound in the smectic- $C^*$  phase (SCE-9, from Merck in the UK, at 25 °C). Here the stripes are attributed to splay deformations of the  $\mathbf{c}$  director induced by frustration from the surface (Meyer and Pershan, 1973). Note that particles within smectic- $C$  thin films are also found to induce similar structures due to thickness gradients created by wetting of the inclusions (Conradi *et al.*, 2006; Harth and Stannarius, 2009; Gharbi *et al.*, 2018).

Another factor that can affect the HH mechanism is saddle splay. Saddle splay is an oft-neglected term in the Frank free energy because it is a total derivative that, by Stokes's

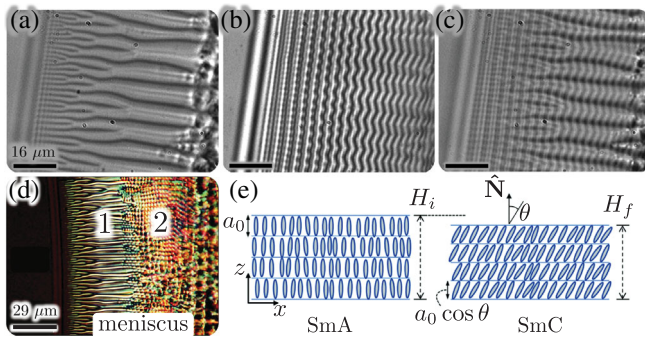


FIG. 23. (a) Bright-field (transmitted light) optical micrographs of the meniscus of a smectic- $C^*$  film (compound SCE-9,  $T = 25^\circ\text{C}$ ). (b) Interferogram of the sample at the same location as in (a). Obtained using phase shifting interferometry, it reveals distorted interference fringes. (c) Superposition of the micrographs in (a) and (b) showing how the  $\mathbf{c}$ -director splay distortions seen in the bright field correspond to the interface undulations captured by the interferogram. (d) Polarized micrograph of the smectic- $C^*$  meniscus reveals two regions: region 1 exhibits radial stripes that are also shown in (a), and region 2 shows a two-dimensional structure of focal conic domains. (e) Schematic depicting the HH instability as a possible origin of smectic layer undulations from the smectic-A–smectic-C phase transition (left-panel, before the transition; right panel, after the transition). After the phase transition, the director tilts with an angle  $\theta$ , causing the natural layer spacing of  $a_0$  to reduce to  $a_0 \cos \theta$ . Although the phase transition causes a decrease in the natural layer thickness, the gradient in meniscus thickness fixes in a certain number of dislocations in the system, thereby fixing in a certain number of layers and the thickness. A mechanical stress analogous to a dilation of the smectic-C layers results from this incompatibility, triggering undulations to accommodate the director tilt. Adapted from Selmi *et al.*, 2017.

theorem, contributes at the system's surface. However, when topological defects form, they also provide additional boundaries in the sample between the defect core and the ordered surrounding. Classic studies of the saddle-splay term in nematics use thin nematic films with hybrid anchoring, where there are homeotropic and degenerate planar conditions on the two confining surfaces. In this case, the saddle splay contributes to a stripe instability (Sparavigna *et al.*, 1992; Sparavigna, O. D. Lavrentovich, and Strigazzi, 1994). We would expect analogous contributions at, say, the interface of a cholesteric if the interface prefers a different orientation of the layers than the bulk. The saddle-splay contribution in the case of uniformly spaced smectic layers is proportional to the Gaussian curvature of the layers and, according to the Gauss-Bonnet theorem, becomes a purely topological contribution. As such, we do not expect it to be pertinent for small undulation instabilities (Ishikawa and O. D. Lavrentovich, 2001a), but it certainly contributes when the layered system develops cusps and folds (DiDonna and Kamien, 2003). The saddle-splay term also plays a role if the nematic order is distorted at a fluid interface. For instance, in the case of thin nematic films with deformable boundaries, the saddle splay is also involved in the onset of stripe instabilities, which have been of continued interest since the early 1990s (Sparavigna, O. D. Lavrentovich, and Strigazzi, 1994; Delabre *et al.*, 2008;

Manyuhina, Cazabat, and Ben Amar, 2010; Manyuhina and Ben Amar, 2013; Barbero and Lelidis, 2015).

Finally, an incompatibility between the layer number and the sample thickness can also trigger undulations. The boundary condition may force the system to have an integer number of layers between the top and bottom of a film. This creates an intrinsic strain on the layers if the film thickness  $d$  is not an integer multiple of the preferred layer size  $t$ . If the sample has a deformable surface, the surface itself will undulate and the surface tension  $\sigma$  will play a role in determining the onset of the instability, as shown in a study of a block copolymer system by Williams (1995). Layer strain induced by the incompatibility of the system thickness with the number of layers was also simulated in cholesterics (Machon, 2017). The induced corrugations on the interface from undulation instabilities are ubiquitous across systems with periodic ground states.

In summary, the interface plays an essential role in the undulation of layered systems, as it provides a mechanism for applying strains to the system through anchoring conditions, surface tension, and boundary curvature, among other sources. The HH mechanism in turn typically modulates the shape of a deformable interface, thereby introducing corrugations. These features may be understood by taking into account the basic elastic properties of the layered system (i.e., layer bending and compression), along with the anchoring energy and surface tension at the interface. In any individual case, the energetic contributions from the anchoring conditions, the surface tension, and the bulk elasticity must be accounted for. The complex interplay between the various contributions generates a great number of variations on this theme of geometrical-frustration-induced undulations.

## VIII. HELFRICH-HURAUULT MECHANISM: HERE, THERE, AND EVERYWHERE

As seen in the systems we have reviewed thus far, undulations in smectics and cholesterics are induced by geometrical frustration, with important and often neglected contributions from deformable boundaries, interfacial curvature, and surface anchoring conditions. However, similar responses to bulk and surface incompatibilities are also prevalent in other materials with periodic ground states. The same mechanisms can be extended to account for phenomena seen in both biological and other synthetic systems. We now demonstrate the ubiquity and utility of the HH mechanism by reviewing undulating responses across a wide array of materials that extends beyond the traditional smectic and cholesteric phases.

### A. Twist-bend nematic phases

Liquid crystal phases formed by banana-shaped, bent-core mesogens undergo the HH instability through undulation of their structures in response to mechanical stress, such as the application of electric and magnetic fields or a reduction in layer spacing with decreasing temperature. Depending upon their rigidity and the presence of system chirality, bent-core molecules can form more than 50 types of liquid crystal phases, including a wide range of layered liquid crystals,

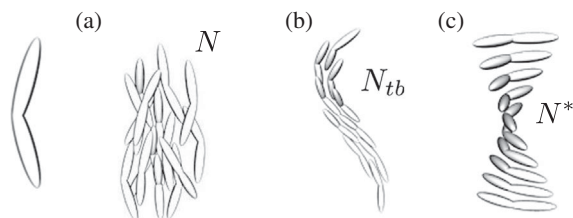


FIG. 24. Schematics of bent-core molecules (leftmost) forming (a) a nematic, uniaxial liquid crystal ( $N$ ), (b) a twist-bend nematic with an oblique helicoid ( $N_{tb}$ ), and (c) a cholesteric (chiral nematic  $N^*$ ) liquid crystal with a right helicoid. The pitch for  $N_{tb}$  phases is typically on the order of 10 nm. Adapted from Mandle, 2016.

among them smectic and cholesteric phases (Fig. 24) (Jákli, O. D. Lavrentovich, and Selinger, 2018). Strains on the periodic structure of these smectic and cholesteric phases will undergo the HH mechanism, similar to the previously discussed systems. However, banana-shaped molecules can also form a twist-bend nematic phase [Fig. 24(b)] in which the director follows a helicoid at a constant oblique angle with respect to the helical axis, resulting in twist and bend deformations throughout the system. Twist-bend nematics have a nanoscopic, molecular-scaled pitch but can create periodic textures on the micron scale, depending on the system thickness. We focus here on the HH mechanism exhibited in twist-bend nematics.

The model bent-core molecule first studied is 1'', 7''-bis(4-cyanobiphenyl-4'-yl)heptane (CB7CB). CB7CB within a glass cell treated for planar anchoring can form focal conic domains that are reminiscent of those observed in smectic phases [depicted in Fig. 25(b)]. Friedel and Grandjean (1910) established that the presence of focal conic domains represents a phase with one-dimensional positional ordering. However, x-ray diffraction and deuterium magnetic resonance measurements of CB7CB reveal no density modulation while suggesting some form of chirality in the system (Cestari *et al.*, 2011). These findings led Cestari *et al.* to be the first to conclude that CB7CB is a twist-bend nematic. Like cholesterics, twist-bend nematics can form a pseudolayer structure defined by the pitch [Figs. 24(b) and 24(c)].

Both CB7CB and KA(0.2) [another twist-bend nematic material, composed of 20 mol % 1'', 9''-bis(4-cyano-2'-fluorobiphenyl-4'-yl)nonane added to a mixture of five odd-membered liquid crystal dimers with ether linkages containing substituted biphenyl mesogenic groups (Adlem *et al.*, 2013)] can generate optically detectable stripes within planar glass cells [Fig. 25(a)]. The stripe periodicity is micron scaled, at least an order of magnitude larger than the measured pitch of the twist-bend nematic's conical helix. The stripe periodicity also depends on the system thickness, and the stripes are not thermodynamically stable. For samples with nonzero dielectric anisotropy, the stripes could be eliminated by applying an electric or magnetic field. Only upon decreasing the temperature of the system afterward would the stripes return (Borshch *et al.*, 2013; Challa *et al.*, 2014). That this periodicity is larger than the phase's intrinsic periodicity and that the stripes are not thermodynamically stable are both

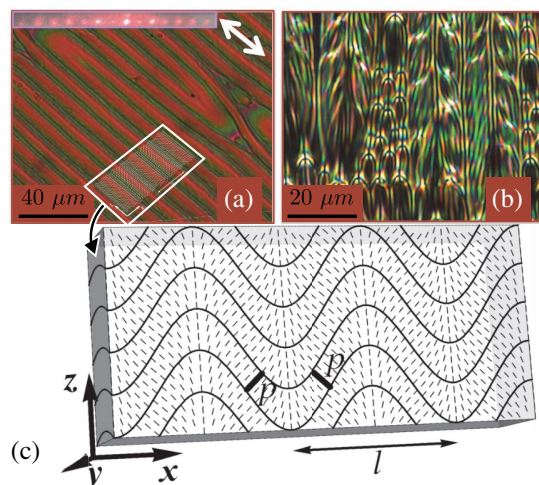


FIG. 25. (a),(b) Micrographs and (c) schematic of stripes formed by bent-core molecules in the nematic twist-bend phase, sandwiched between a 10- $\mu\text{m}$ -thick planar cell. The micrographs in (a) and (b) are KA(0.2) and CB7CB, respectively. (a) KA(0.2) has stripes shown through cross-polarized light microscopy that are also distinguishable by the diffraction pattern in the top inset. The white arrow indicates the direction of rubbing. Bottom inset: modulation of the helical axis of KA(0.2), which is enlarged in (c). (b) The stripes in CB7CB are more complex, generating arrays of focal conic domains. The period of stripes in (a) and (b) are proportional to the cell thickness. (c) The thickness-dependent stripes in twist-bend phases are well captured by the HH model illustrated in the schematic. The thickness of the pseudolayer  $p$  is the pitch of the conical helix. The direction of the helical axes (short lines) undulate in the  $x$  direction, with a period  $\ell$ . Adapted from Challa *et al.*, 2014.

properties reminiscent of the HH instability in smectics and cholesterics.

Stripes and focal conic domains dependent upon system thickness or process history are signatures of the HH instability, as exemplified by the previously discussed smectic and cholesteric shells. Challa *et al.* (2014) used a coarse-grained model of twist-bend phases to describe the optical stripes seen for both CB7CB and KA(0.2). The framework of the HH instability is then applied [Fig. 25(c)] to capture the critical magnetic field strength necessary for stripe elimination and to estimate the elastic properties of CB7CB and KA(0.2) (Challa *et al.*, 2014). Notably, the undulations in twist-bend phases are hypothesized to be created by the shrinking of pseudolayers from decreasing the system temperature, reminiscent of the stripe formation in smectic- $C$  menisci.

Last, we note that twist-bend nematics are also the first example of a fluid with local polar order without density modulation, and measurements on structures generated by the HH mechanism confirm this. Pardaev *et al.* (2016) performed light scattering on a twist-bend nematic sample exhibiting parabolic focal conic domains that nucleated from the HH instability to detect the existence of this local polar order, evidenced by a second harmonic signal that is absent in the parabolic focal conic domains of smectic- $A$  phases. Again structures attributed to the HH instability since the 1970s, such as parabolic focal conic domains in smectics and cholesterics,

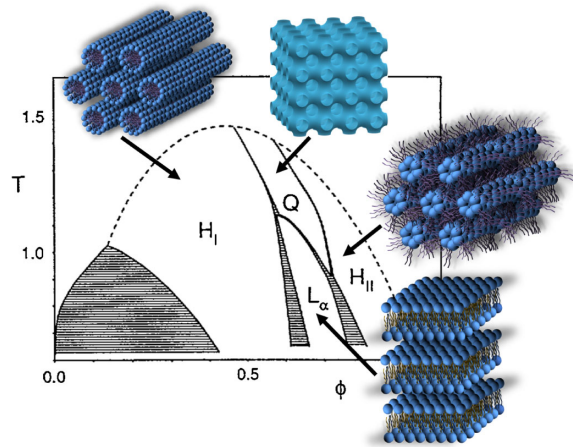


FIG. 26. Mean-field phase diagram of amphiphilic molecules in solution. The various ordered phases are indicated. The dark regions have two-phase coexistence. We focus particularly on undulations in the  $L_\alpha$  lamellar phase and in the hexagonal columnar phase  $H_{II}$ . Adapted from Gompper and Klein, 1992.

are being found in recent phases, like the twist-bend nematic phase, illustrating the pervasiveness and relevance of this mechanism in partially ordered systems.

### B. Lyotropic liquid crystals

A significant class of materials that also exhibits spatially modulated phases including cylindrical, layered, and foamlike configurations is lyotropic liquid crystals, which are collections of amphiphilic molecules in a solvent. The mixtures can involve multiple components but often include surfactant molecules and a solvent mixture that may contain salts or organic compounds, such as cyclohexane or alcohols. The thermodynamic phase of these materials is controlled by the concentration of the solute (typically the surfactant molecule), along with the temperature. A good phase diagram is shown in Fig. 26. Note that at sufficiently low temperatures  $T$  we transition between a series of various ordered phases as we increase the concentration  $\phi$  of the amphiphile in solution. The typical sequence of phases starts with a dilute micellar solution at low concentrations transitioning to a hexagonal arrangement of micellar cylinders at higher concentrations, then to a lamellar arrangement (or a bicontinuous phase  $Q$ , shown in Fig. 26), until finally transitioning to an inverted micellar cylinder phase at high concentrations. All of these ordered phases are spatially modulated structures with some characteristic length of spacing  $\lambda$ . As such, frustration imposed on the system that competes with the spacing  $\lambda$  may lead to undulation instabilities.

The aqueous nature of lyotropics allows one to strain the system in myriad ways, including via shear flows and doping with nanoparticles, which may in turn be controlled with electric or magnetic fields. Many of these perturbations result in the HH mechanism because the lamellar phase ( $L_\alpha$  in Fig. 26) is for all intents and purposes equivalent to the previously described layered smectics and cholesterics. For the lyotropic lamellae, shear flow may be applied to induce layer undulations (Diat, Roux, and Nallet, 1993; Marlow and

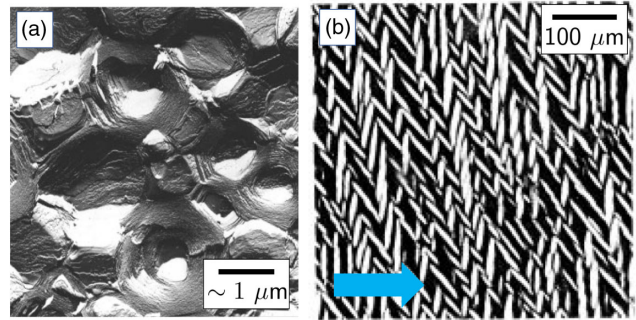


FIG. 27. (a) Freeze fracture electron microscopy section of a lyotropic lamellar phase after an applied shear. The lamellae turn into a dense packing of multilamellar “vesicles.” Adapted from Gulik-Krzywicki *et al.*, 1996. (b) Polarized microscopy image of a lyotropic columnar phase ( $H_I$  in Fig. 26) undergoing an instability to a herringbone pattern. This is achieved by doping the material with magnetic nanoparticles and applying a field  $\mathbf{B}$  (blue arrow) that acts to reorient the cylinders. Adapted from Ramos, Fabre, and Fruchter, 1999.

Olmsted, 2002). At small shear rates, the buckling instability may be directly related to an undulation produced by a dilative strain, with a characteristic length given by  $\lambda_c \sim \sqrt{\lambda \ell}$ , where  $\lambda$  is the lamellar spacing and  $\ell$  is the sample thickness (Zilman and Granek, 1999). It is also possible to induce undulations in these smecticlike states via confinement that is incompatible with a particular number of layers, which then reduces the problem to essentially an identical analysis as a smectic liquid crystal in a cell (MacKintosh, 1994).

Under larger flows, the lamellar phase may break up into a packing of multilamellar vesicles (Diat, Roux, and Nallet, 1993; Gulik-Krzywicki *et al.*, 1996; Sierro and Roux, 1997) or analogs of focal conic domains (Pommella, Caserta, and Guido, 2013). An example of the resultant structure is shown in Fig. 27(a). Under these more extreme shear conditions, interesting intermediate phases may also form, including a phase in which multilamellar cylinders orient along the shear direction (Zipfel *et al.*, 2001). These multilamellar cylindrical structures may in turn also exhibit undulations via, for example, the alteration of the spacing between lamellae or an induced curvature (Santangelo and Pincus, 2002).

The cylindrical phases ( $H_I$  and  $H_{II}$  in Fig. 26) also have interesting ground states that can undergo the HH mechanism. The characteristic size  $\lambda$  between adjacent pairs of cylinders may be frustrated by an applied strain or cylinder reorientations under flow or applied fields. The cylinders may accommodate these strains by undulating or buckling. It is also possible to induce undulatory instabilities in the cylindrical phases by, for example, doping the phase with magnetic particles and then reorienting the phases with an applied magnetic field. At high fields, a herringbone structure is observed, as shown in Fig. 27(b) (Ramos, Fabre, and Fruchter, 1999), that is reminiscent of the herringbone structures we see in smectic shells (described in Sec. VI.A).

Given the multicomponent mixtures involved in forming the lyotropic phases and the complex set of interactions in forming the ground states with an associated characteristic length  $\lambda$ , it is difficult to model these systems without resorting

to a phenomenological description. One possibility is to use molecular dynamics simulations. However, even simple, single lipid bilayers present challenges, even with the rapid advancements in computational tools (Moradi, Nowroozi, and Shahlaei, 2019). To our knowledge, there are no existing detailed microscopic models of these HH-like responses in lyotropic materials.

### C. Diblock copolymers, polymer bundles, and sheets

Block copolymers also exhibit ordered lamellar phases similar to lyotropic liquid crystals (Fig. 26). However, unlike lyotropics, block copolymers typically have a fixed density. Therefore, tuning between different ordered phases is achieved by changing the structure of the constituent polymers themselves instead of varying the concentrations of system components, as is typically done for lyotropic systems. Here we focus primarily on *diblock* copolymers, where two polymers of *A*- and *B*-type monomers are grafted together.

The two *A* and *B* segments of the copolymer typically have some incompatibility, which is captured via a Flory-Huggins term in the free energy  $\chi \int \psi_A(\mathbf{r})\psi_B(\mathbf{r})d\mathbf{r}$ , where  $\psi_{A,B}$  are the local volume fractions of *A*- and *B*-type monomers [taken to satisfy  $\psi_A(\mathbf{r}) + \psi_B(\mathbf{r}) = 1$ ]. A self-consistent mean-field analysis of the total free energy does a reasonable job in predicting the observed phases of these materials, which include a lamellar phase, a hexagonally packed cylinder phase, and gyroid phases, among others (Bates and Fredrickson, 1990; Mai and Eisenberg, 2012). In the weak-segregation limit, where the *A* and *B* portions only weakly demix, the system is effectively described by a Brazovskii-type free energy (Brazovskii, 1975; Fredrickson and Helfand, 1987)

$$f_{\text{cp}} = \frac{1}{2} \int [r + (q - q^*)^2][\psi(\mathbf{q})]^2 d\mathbf{q} + \frac{\mu}{6} \int [\psi(\mathbf{x})]^3 d\mathbf{x} + \frac{u}{24} \int [\psi(\mathbf{x})]^4 d\mathbf{x}, \quad (26)$$

where  $\psi(\mathbf{x})$  [as well as its Fourier transform  $\psi(\mathbf{q})$ ] describes the deviation of the relative *A/B* monomer density from the well-mixed disordered phase. The unstable mode  $q^*$  is related to the wavelength  $\lambda^*$  of the *AB* domains via  $q^* = 2\pi/\lambda^*$ . In the strong-segregation limit, the  $(q - q^*)^2$  term has to be replaced with an appropriate interaction term that couples the Fourier transformed fields  $\psi(\mathbf{q})$  at different modes  $\mathbf{q}$  (Kawasaki and Kawakatsu, 1990).

The phases of block copolymers are analogous to the lyotropic phases highlighted in Fig. 26. Although the lyotropics typically have more dilute phases, such as a suspension of spherical vesicles, these phases are not achievable in a block copolymer. The major difference between the two systems is that the amphiphile concentration  $\phi$  is replaced by the relative density of the *A* and *B* monomers  $\psi$ , which always has some molecular variation due to the block copolymer molecular structure. We focus primarily on the lamellar and cylindrical phases to examine the HH instability in diblock copolymers. For these phases, perturbations of the

system away from the ground state can be examined in both the weak- and strong-segregation limits.

The lamellar phases of diblock copolymers exhibit the same undulatory instabilities as discussed for the other lamellar phases. Uniaxial strain applied perpendicular to the lamellae leads to the HH instability similar to that found in the classic smectic and cholesteric systems (Wang, 1994). At large strains, the copolymer can develop a herringbone structure reminiscent of that observed in the smectic shells of Sec. VI.D (Cohen *et al.*, 2000). An important difference is that the phases of diblock copolymers depend on an interaction parameter  $\chi$  and can exhibit a strong-segregation regime when the *A* and *B* portions of the copolymer are highly repulsive, or a weak-segregation regime when  $\chi$  is small. Yet it is possible to perform a perturbative analysis to examine the HH instability in both regimes. In the strong-segregation limit, the approach is the same as for magnetic systems, which we detail later in this section (Sornette, 1987; Asciutto, Roland, and Sagui, 2005). In the weak-segregation limit, a smecticlike free energy can be derived by perturbing away from a uniform stripe phase  $\psi(\mathbf{x}) = A \cos(2\pi\hat{\mathbf{d}} \cdot \mathbf{x}/\lambda)$ , with  $\hat{\mathbf{d}}$  the direction of the stripes or lamellae. The details of this analysis were given by Matsumoto *et al.* (2015). It is also possible to model the HH instability by simulating the relaxation of a system with the free energy in Eq. (26) under an appropriate perturbation.

For diblock copolymers, a possible perturbation that induces an undulation is a strain from an electric field applied normal to the lamellae. Since the lamellae prefer to lie along the field, the applied field rotates them. The resultant undulations may be phenomenologically described by a smecticlike free energy with an associated HH-like instability (Onuki and Fukuda, 1995). We note that such a phenomenological theory has some deviations that are better captured by a self-consistent field theory treatment (Matsen, 2005; Matsen, 2006), where the basic prediction  $\lambda^* \sim \sqrt{\lambda\ell}$  holds (Matsen, 2006) under certain conditions. However, it is also possible for the block copolymers to develop an instability at a wavelength that is close to the lamellar spacing itself ( $\lambda^* \sim \lambda$ ). The undulations may also occur in two dimensions, creating a square lattice of deformations that are reminiscent of the parabolic focal conic domains detailed in Sec. III.B (Xu *et al.*, 2005; Tsori and Andelman, 2008).

In general, the layer reorientation mechanism of diblock copolymer systems under an applied field is complex, and there is a sustained interest in elucidating all of the possible regimes (Orizaga and Glasner, 2016). One may observe some of the subtleties in Fig. 28(b), where three different regions are identified in a single sample, under the same applied field. Despite the variety in the morphology of the instability, in all cases we observe a frustration between some applied strain and the equal layer spacing of the ground state, as with the other systems considered in this review.

The columnar, or hexagonal, phases of diblock copolymers also exhibit HH-like instabilities. Applying a uniaxial strain perpendicularly to the length of the cylinders may induce undulations as the cylinders try to maintain the same spacing under strain [Fig. 29(a)]. The resultant instability in the cylinders, which is illustrated schematically in Fig. 29(b),

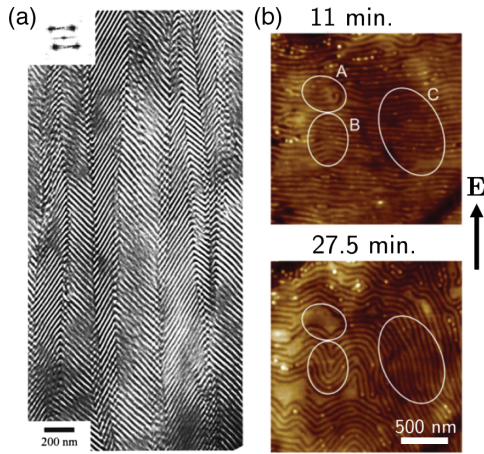


FIG. 28. (a) TEM micrograph of a diblock copolymer under a large uniaxial strain (300%) exhibiting a characteristic herringbone structure. This structure may develop from a HH mechanism. Adapted from [Cohen \*et al.\*, 2000](#). (b) Two snapshots of a diblock copolymer lamellar phase shown after the indicated number of minutes under an applied electric field  $\mathbf{E}$ . The lamellae are initially oriented horizontally, and the applied field reorients the layers. Three regions are indicated that have different reorientation behaviors, including an undulationlike mode, but with a sharp kink that is on the order of the lamellar spacing. Adapted from [Liedel \*et al.\*, 2015](#).

may be analyzed in the same fashion as the lamellar system ([Hamley, 1994](#); [Pereira, 2002](#)).

A related instability is also found in bundles of elastic filaments ([Bruss and Grason, 2018](#)). The instability arises there when one has a defect in the hexagonal packing of fibers. The packing defect, a disclination, is incompatible with the equal spacing of the cylinders in the packing. The cylinders then buckle to relieve this frustration ([Bruss and Grason, 2018](#)). Depending on the type of disclination, one can find various deformation modes, two of which are shown

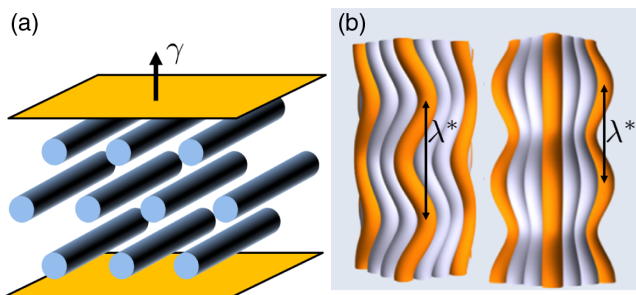


FIG. 29. Schematics of diblock copolymers under strain. (a) Uniaxial strain  $\gamma$  applied perpendicularly to the cylinders in a hexagonal phase of the diblock copolymer results in a HH undulatory instability of the cylinders, which is similar to that shown in (b) for bundles of elastic fibers. The bundles exhibit undulation instabilities as in the columnar phases of the diblock copolymer (and discotic liquid crystals). The buckling in the fiber bundles, with characteristic size  $\lambda^*$ , comes from geometrical frustration resulting from the incompatibility of disclinations in the cylindrical packing and the equal cylinder spacing. Adapted from [Bruss and Grason, 2018](#).

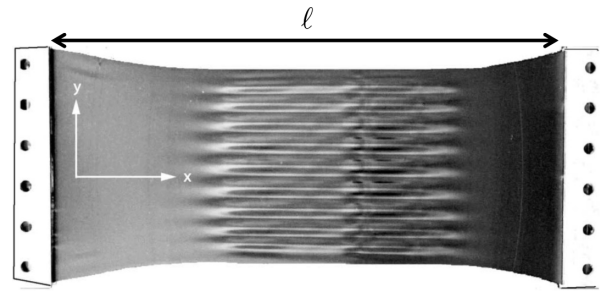


FIG. 30. Photographs of wrinkles in a stretched elastic sheet having a characteristic periodicity given by  $\lambda^* \approx 2\sqrt{\pi\lambda\ell}$ , with  $\ell$  the film length and  $\lambda \sim (B/T)^{1/2}$  an elastic characteristic length scale, where  $B$  is the bending stiffness and  $T$  is the tension in the film. Note how similar this wavelength is to the classic Helfrich-Hurault instability size given in Eq. (19). Adapted from [Cerdea and Mahadevan, 2003](#).

in Fig. 29(b). This is yet another example where geometrical frustration leads to a spatial modulation, the central theme of this review.

The Helfrich-Hurault mechanism can also be seen in thin polymeric sheets, with undulations shown in Fig. 30. The interfacial undulations of lamellar elastic fluids, detailed in Sec. VI.B, can be generalized to include the wrinkling of an elastic sheet. For a polymeric sheet to have undulations, the single layer of length  $\ell$  is stretched, creating wrinkles in the material with a characteristic size  $\lambda^* \approx 2\sqrt{\pi\lambda\ell}$  that is similar in form to Eq. (19) ([Cerdea and Mahadevan, 2003](#)). While the undeformed system in this case is isotropic, there is still the characteristic length scale  $\lambda \sim (B/T)^{1/2}$  provided by the bending stiffness  $B$  of the sheet and the applied tension  $T$ . In contrast to lamellar liquid crystals, the source of this length scale is not inherent to the material and requires external forces ([Cerdea and Mahadevan, 2003](#)) or geometrical frustration ([King \*et al.\*, 2012](#); [Paulsen \*et al.\*, 2016](#); [Aharoni \*et al.\*, 2017](#); [Tovkach \*et al.\*, 2020](#)) to arise. Despite these differences, the characteristic length in stretched polymeric sheets is analogous to the characteristic wavelength in Eq. (11) for either the cholesteric or the smectic penetration depth. The HH mechanism can thereby occur in both systems, resulting in corresponding undulation wavelengths.

After these wrinkles form in a single sheet, it is possible to get secondary undulations. Indeed, the original, primary wrinkles can be likened to a two-dimensional smectic. The wrinkles resist deformation and can be mapped to a smectic liquid crystal energy ([Aharoni \*et al.\*, 2017](#); [Tovkach \*et al.\*, 2020](#)). If they are subjected to additional forces or boundary frustration, these wrinkles can themselves undergo the HH mechanism in response to strain in the preferred wrinkle spacing. These secondary undulations would be reminiscent of those detailed in Secs. V.C and VI.D for cholesteric and smectic shells, respectively. The diversity of polymeric systems highlighted in this section demonstrate how the HH model applies to systems across length scales. Strain and geometrical incompatibilities can generate spatial modulations in systems varying in size from hundreds of nanometers to the centimeter scale.

#### D. Columnar liquid crystals

The HH instability has also been postulated as the striation mechanism for columnar phases. Cagnon, Gharbia, and Durand (1984) and Gharbia, Cagnon, and Durand (1985) were the first to observe an undulation instability in columns of a *thermotropic*, discotic liquid crystal forming stripes under both compression and dilation of the system, reminiscent of the HH instability of smectics under dilation. They used the HH model to discover that the curvature elastic modulus of thermotropic, columnar liquid crystals can be 6 orders of magnitude larger than that of thermotropic smectics and nematics, possibly due to column entanglements.

A decade after the work of Cagnon, Gharbia, and Durand, Oswald *et al.* (1996) observed similar undulatory behavior in hexagonal, *lyotropic* liquid crystals, with strain introduced by a directional growth apparatus, in which the sample, sandwiched between two glass plates, is pulled across a pair of hot and cold ovens. Compared to the dilation experiments, the lyotropic system of Oswald *et al.* underwent undulatory instabilities due to thermal effects, thereby experiencing mechanical stress in both vertical and in-plane directions. Their measurements and calculations further indicated that the columns in their system are not correlated at large distances. However, whether that conclusion can be drawn for thermotropic systems remains unknown due to experimental difficulty in obtaining thermally induced striations in thermotropic, discotic liquid crystals. Furthermore, isolating the formation of stripes through macroscopic dilation of lyotropic systems is challenging because of difficulties in mitigating water evaporation.

Water evaporation has been suggested as a source of frustration that could induce undulatory instabilities for lyotropic systems in more recent experiments. Kaznatcheev *et al.*, 2007 studied a lyotropic liquid crystal that forms columns in the chromonic phase. Lyotropic chromonic mesophases are typically formed by planklike molecules with aromatic cores surrounded by polar groups that can also form columns. In water, the molecules form charged columns by stacking face to face in order to hide their aromatic cores. Because the interdisk association is through weak, non-covalent interactions, the assembled columns are polydisperse, with their average lengths dependent upon the disk molecular concentration, the disk ionic strength, the depletant concentration, and the temperature (Tortora and O. D. Lavrentovich, 2011).

Kaznatcheev *et al.* (2007) used a sulfonated benzo[de]benzo[4,5]imidazo[2,1-a]isoquinoline[7,1] dye as the lyotropic, chromonic liquid crystal and observed stripes appearing after film deposition, exposed to air. The stripe direction was perpendicular to the column direction, indicating that the stripes resulted from buckling of the columns. They described the striations with a HH model, hypothesizing that the evaporation of water creates mechanical stress in the system by decreasing the separation between adjacent columns. The excess space caused by the evaporation must be filled by either adding new columns or tilting the columns. Creating new columns would generate dislocations that then propagate throughout the system, which is energetically costly and slow. However, tilting of the columns could occur rapidly

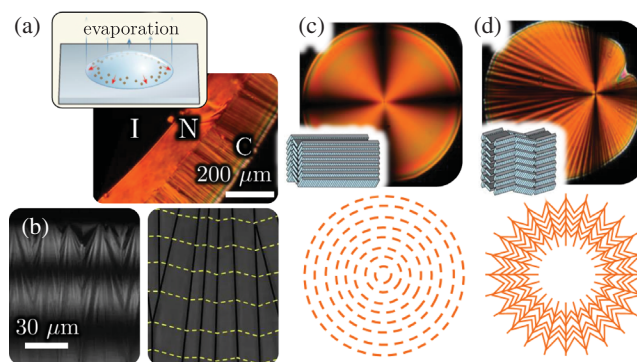


FIG. 31. (a) Schematic of the evaporation of a particle suspension within a sessile droplet occurs more rapidly at the droplet edges, driving particles to the contact line, resulting in the “coffee ring” effect. The coffee ring effect for an aqueous solution of Sunset Yellow results in phase coexistence, isotropic (*I*) near the center, then nematic (*N*), and finally columnar (*C*) when moving radially outward (bottom). Inset adapted from Larson, 2017. (b) Domain walls are formed, visible under polarizing microscopy (left image), resulting from the buckling of columns (yellow line, right schematic). Adapted from Davidson *et al.*, 2017. (c) The coffee ring effect is slowed when the droplet is immersed in oil instead of air, resulting in the columns forming a neat nematic phase. (d) Further evaporation leads to a controlled herringbone texture from the buckling of columns. Bottom schematics adapted from Lydon, 2010. Cross-polarized micrographs courtesy of Kunyun He.

and thus would be more favorable, which is again reminiscent of the classic HH instability.

Investigating lyotropic, chromonic systems with gradients of concentration from water evaporation is desirable to better validate the HH model as the mechanism of stripe formation. The so-called coffee ring effect achieves this, in which a sessile droplet of a particle suspension has an evaporation rate dependent upon the radial distance to the center of the droplet, with the highest evaporation rate at the droplet’s contact line [Fig. 31(a), inset]. This evaporation gradient drives particles toward the droplet’s outermost rim, subsequently generating a radial concentration gradient of particles. A sessile droplet of the lyotropic, chromonic dye, Sunset Yellow, undergoing the coffee ring effect exhibits a concentration gradient of the mesogen, resulting in the coexistence of phases within the droplet [Fig. 31(a), bottom panel]. The columnar phase near the contact line has radially aligned stripes. Davidson *et al.* (2017) measured the light adsorption due to linear dichroism, revealing that the average director orientation is parallel to the contact line [Fig. 31(b), right panel]. Domain walls of the columnar phase are also visible in the left panel of Fig. 31(b), indicating the presence of undulations that bend the columns during the evaporation process.

The evaporation of water can be slowed by replacing the surrounding air with oil. This is accomplished by introducing a nonionic triblock polymer surfactant with hydrophilic polyethylene oxide in the ends and a hydrophobic polypropylene oxide in the center, such as Pluronic 31R1. The surfactant aids the wetting of the aqueous Sunset Yellow droplet on glass within hexadecane. By slowing the water

evaporation rate, a smooth nematic phase of the columns can be obtained [Fig. 31(c)]. Further evaporation then generates a uniform herringbone texture in the droplet [Fig. 31(d)]. As the solution is progressively concentrated, the existing columns are extended, creating a differential strain in the mesophase that results in undulations and buckling of the columns [illustrated at the bottom of Fig. 31(d)]. The fracturing of the columns is likely a consequence of bend deformations being more energetically costly than discontinuities, suggesting stronger inter-columnar association at high dye concentrations.

The herringbone texture can also be found in phases of more complex molecules like biological polymers, including DNA. The polarized optical micrographs of condensed xanthan, poly( $\gamma$ -benzyl-L-glutamate) (PBLG), and DNA were investigated by Livolant and Bouligand (1986), who observed the transition from undulations to a herringbone pattern (shown for PBLG in Fig. 32). The formation of secondary domains of periodicity within the herringbone pattern

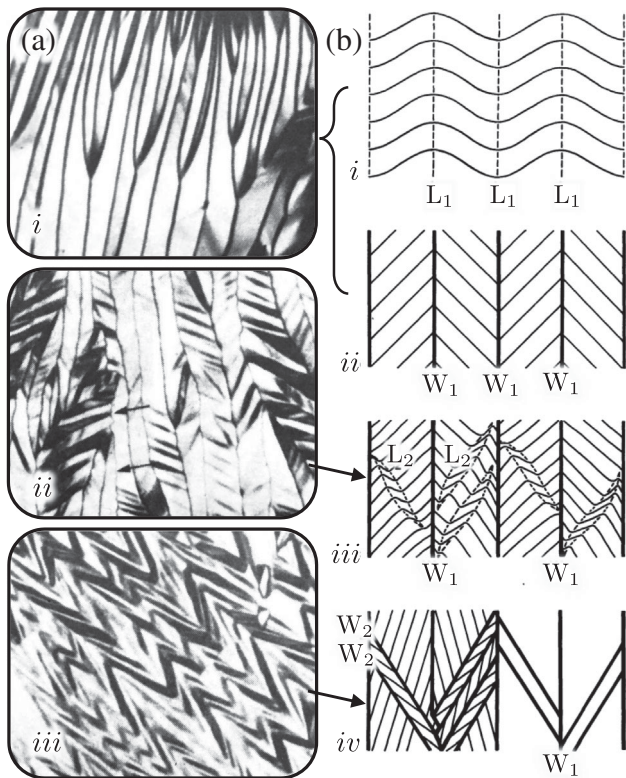


FIG. 32. (a) Textures of the hexagonal columnar phase of PBLG are shown in polarizing optical micrographs at 120 times magnification. (i)–(iii) Depiction of evolving texture from undulations to a herringbone pattern. In (ii), regions of maximum curvature of the PGLA become walls of discontinuity and new undulations appear within elongated domains. (b) Illustration of the textural transformation from (i) an undulating pattern to (iv) a herringbone pattern. Molecular orientations are represented by solid thin lines, walls of bend deformations ( $L$ ) are indicated by dashed lines, and walls of discontinuity ( $W$ ) are drawn as thick lines. Bend walls  $L_1$  transform into domain walls  $W_1$  as the molecular concentration increases. The process is repeated to form secondary domains, where bend walls  $L_2$  transform into secondary discontinuities  $W_2$ . Adapted from Livolant and Bouligand, 1986.

described by Livolant and Bouligand is evocative of the formation of secondary domains within smectic shells detailed in Sec. VI.A. Condensed DNA also exhibits the herringbone texture (Livolant *et al.*, 1989). Livolant *et al.* confirmed with electron microscopy and x-ray diffraction that highly concentrated, 50 nm DNA molecules have columnar longitudinal order and hexagonal lateral order and can also form undulating patterns (Livolant and Leforestier, 1996). Studies of the evaporation of DNA suspensions exemplified by Smalyukh *et al.* (2006) and Cha and Yoon (2017) produced DNA textures that should also be describable with the HH model. The HH instability is prevalent even in aqueous liquid crystals.

### E. Biological materials

Undulation instabilities can also be seen in biological systems at intermediate length scales, such as within systems of particlelike fibrils like chitin, found in the exoskeletons of beetles and crustaceans, and cellulose, found within plants. Both chitin and cellulose, as with the majority of biological materials, have chiral building blocks. When concentrated beyond a threshold value, these biopolymers can form particles that self-assemble into colloidal, cholesteric liquid crystals (Bouligand, 1972b; Rey, Herrera-Valencia, and Murugesan, 2014). The cholesteric pseudolayer reorientation and focal conic domain formation at a curved interface were seen on the surface of jeweled beetle shells due to the cholesteric ordering of the constituent chitin, which provides a mechanism for their structural coloring and optical response (Sharma *et al.*, 2009; Rey, Herrera-Valencia, and Murugesan, 2014). Cellulose nanocrystals, derivable via acid hydrolysis from bacteria, cotton, wood, tunicate, etc., can also be concentrated to form a cholesteric phase (Lagerwall *et al.*, 2014). Colloidal suspensions of cellulose nanocrystals can be spread and evaporated to form a solid, dry film with photonic properties, forming a polydomain, cholesteric structure with a pitch in the visible wavelength range. Parabolic focal conic domains reminiscent of those seen in smectics under mechanical strain have been observed in cellulose nanocrystal films [Sec. III.B (Roman and Gray, 2005; Parker *et al.*, 2018)]. Large magnetic fields can be used during evaporation to form a single domain with the pitch aligned along the direction of the magnetic field, as shown in Fig. 33 (Frka-Petesic *et al.*, 2017). When Frka-Petesic *et al.* applied a horizontal magnetic field during drying, with the cholesteric helix aligned perpendicularly to the plane of evaporation, they found a zigzag pattern in the film [Fig. 33(b)]. Although mechanical stress in the system is applied parallel to the layers in this case, the zigzag pattern can also be thought of as the result of a HH-type mechanism. Evaporation during the processing of cellulose nanocrystal films could further introduce hydrodynamic stresses that can undulate and strain the cholesteric pseudolayers (Chu *et al.*, 2018; Chan *et al.*, 2019), as with the lyotropic systems of Sec. VIII.B. Cellulose nanocrystals can additionally be evaporated within spherical confinement, resulting in HH-like buckling (Parker *et al.*, 2016, 2022).

Generally, biological systems are not only often *chiral* but also *active*, and therefore out of equilibrium (Bouligand, 1972b; Roland, Reis, and Vian, 1992; Sharma *et al.*, 2009; Rey, 2010; Mitov, 2017; Beliaev *et al.*, 2021). Undulations

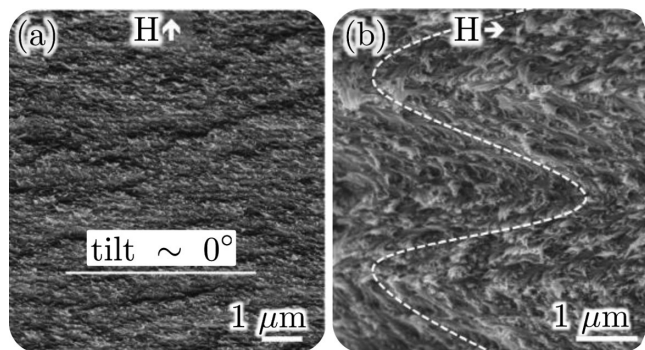


FIG. 33. Scanning electron micrographs of cross sections from evaporated cellulose nanocrystal films. (a) Applying a vertical magnetic field (indicated by  $\mathbf{H}$ ) upon drying yields a single-domain, homogeneous cellulose nanocrystal film, with the pitch axis parallel to the magnetic field direction. (b) Applying a magnetic field to align the pitch axis horizontally generates a zigzag pattern after evaporation, thereby indicating buckling of the cholesteric pseudolayers. Adapted from Frka-Petescic *et al.*, 2017.

seen in the development of the primary cell walls of plants is a striking example of a dynamic HH mechanism (shown in Fig. 34). Activity, including forces generated during growth processes, introduces hydrodynamic stresses that strain the chiral ordering of the system [Fig. 35(a)]. Whitfield *et al.* (2017) investigated cholesterics from the framework of active liquid crystals, integrating force-dipole stresses into a passive, chiral nematic formulation. They found that extensile stresses can trigger HH layer undulations in cholesterics. The steady state director fields and their



FIG. 34. Transmission electron micrograph of the elongating zone of mung bean seedlings (*Vigna radiata*). The cholesteric pseudolayers of the cell wall, which are visible through the Bouligand arches of the cross section, undulate near the interface where growth of the cell wall takes place (bottom). From Roland, Reis, and Vian, 1992.

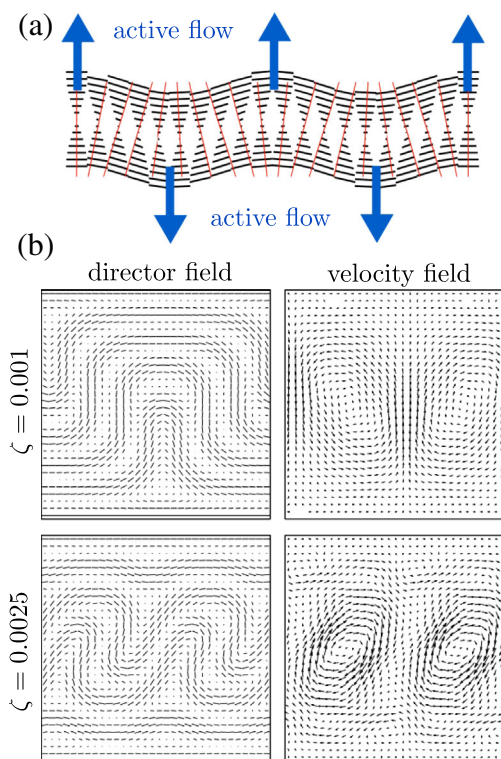


FIG. 35. (a) Sketch of the HH mechanism in extensile, active cholesterics. The black lines show the projection of the director field onto the plane, while the red lines represent the splayed pitch axis. The blue arrows show the active flow direction, which increases the distortion and drives the undulation instability. (b) Simulation results for an extensile, active cholesteric confined in a quasi-two-dimensional geometry with flat walls. Homogeneous planar anchoring is set for both the top and bottom surfaces. The right column plots projections of the director field onto the plane, and the left column plots the corresponding velocity fields. Here  $\zeta$  is proportional to the concentration of active particles and is positive for extensile materials and negative in contractile ones. For both  $\zeta = 0.001$  and  $0.0025$ , the profiles are steady states of the system. Adapted from Whitfield *et al.*, 2017.

corresponding velocity fields for varying extensile activity levels are plotted in Fig. 35(b). Both director fields exhibit pairs of  $\lambda^\pm$  pitch defects that are reminiscent of defects in cholesterics shells. Pairs of  $\lambda^\pm$  defects often result from the HH instability in cholesterics, as detailed in Sec. V. Kole *et al.* (2021) advanced this work by showing how active stresses in cholesterics couple uniquely to the chirality of the material, thereby generating elastic forces tangent to the layers. This “odder than odd” elasticity from chiral activity leads to HH-like undulations that produce a two-dimensional array of hydrodynamic vortices. Whether passive or active, the HH mechanism is a viable mechanism of pattern formation in biological materials.

## F. Magnetic systems

Thin magnetic films present an interesting two-dimensional version of the HH instability. These films can be fabricated from epitaxial garnet or a thin cobalt slice (Demand *et al.*,

2002). In certain cases, these films have magnetic domains in the form of stripes or hexagonal arrays of bubbles with a characteristic size  $\lambda$  that is analogous to the smectic layer spacing or the spacing between cylinders in a hexagonal phase of a block copolymer. These domains form when long-range dipolar magnetic interactions, which favor antiparallel alignment of magnetic spins, compete with the usual short-range ferromagnetic interaction, which tends to align neighboring spins. This is a typical scenario of short-range attractive and long-range repulsive interactions necessary to form systems that exhibit modulated phases. The spatial modulations may then take the form of stripes, with properties analogous to smectic liquid crystals or block copolymers. As previously summarized, such modulated phases exist in a wide range of systems including phase-segregating lipids, block copolymers, and ferrofluids (Seul and Andelman, 1995; Andelman and Rosensweig, 2009).

To understand the instability in a ferromagnetic film, consider a coarse-grained magnetization field  $M(\mathbf{x})$  describing the magnetization in the thin film at some spatial coordinate  $\mathbf{x} = (x, y)$ . The free energy for  $M(\mathbf{x})$  will have the general form

$$f_M = \int d^2\mathbf{x} \left[ \frac{D}{2} |\nabla M|^2 + \frac{r}{2} M^2 + \frac{u}{4} M^4 + \mu \int d^2\mathbf{x}' M(\mathbf{x}) g(\mathbf{x} - \mathbf{x}') M(\mathbf{x}') \right], \quad (27)$$

where  $g(\mathbf{x} - \mathbf{x}')$  is a Green's function for the dipolar interactions and  $D$ ,  $r$ ,  $u$ , and  $\mu$  are phenomenological constants related to the material properties. We generally expect its Fourier transform to be  $g(\mathbf{q}) \approx -g_1|\mathbf{q}|$ , which gives us the necessary instability for the formation of a modulated phase with a characteristic wavelength  $t = 2\pi/q^* \approx 16\pi^3 D/g_1\mu$  (Andelman and Rosensweig, 2009). In general, there are two types of patterns: an array of circular domains and

uniform stripes. In the case of the stripe ground state, the free energy in Eq. (27) can be shown to be equivalent to the smectic free energy in two dimensions (Sornette, 1987; Asciutto, Roland, and Sagui, 2005). There is then an analog of the HH mechanism when a magnetic field is applied since a magnetic field has the tendency to change the characteristic size  $t$  of the domains. Cycling this field or heating the system has the same dilational effect as a mechanical strain in a smectic system (reviewed in Sec. III.B). Thus, the HH instability can also be realized in thin magnetic films. Examples of the domain shapes that one finds under such perturbations are shown in Fig. 36.

## IX. CONCLUSION

In this review, we spotlight the applicability of the HH mechanism to a broad range of materials with periodic ground states. By surveying phenomena in cholesteric and smectic liquid crystals, we illustrate geometrical frustration in lamellar systems as a result of sources ranging from applied fields to boundary conditions. The frustration is then relieved by the HH mechanism, where undulations produce periodic structures with wavelengths orthogonal to and larger than that of the ground state.

By considering examples of cholesteric and smectic shells, where the liquid crystal is confined between two concentric and spherical fluid interfaces, we highlight the role of topological constraints, anchoring conditions, boundary deformability, and curvature. These factors can both trigger the HH mechanism and shape the resulting patterns. While topological frustration necessitates the existence of discontinuities from the global curvature, the HH mechanism cares only about how the system looks locally. Topological constraints can dictate that a frustration exists, but the exact reaction to the frustration is a question of energetics and local geometrical incompatibilities. The HH mechanism is then, in its nature, a response to local geometrical frustration.

The generality of the HH mechanism is evident from undulation instabilities appearing in periodic systems beyond the classic thermotropic lamellar phases. These include twist-bend nematics, lyotropic liquid crystals, and polymers, as well as biological and magnetic materials. After accounting for fluid boundaries, the HH mechanism can also describe phenomena in living matter, where fluid interfaces are pervasive and activity can strain lamellar structures.

We anticipate that the HH mechanism will become increasingly valuable for understanding the organization of layered materials. The phases formed by bent-core rods are an enduring area of investigation, newly invigorated by the experimental realizations of the splay-bend nematic (Fernández-Rico *et al.*, 2020; Meyer *et al.*, 2020; Chiappini and Dijkstra, 2021). Future studies on the structures formed by these spatially modulated phases will almost certainly rely upon the HH model, as exemplified by the striations of twist-bend nematics. Moreover, as the field of active liquid crystals progresses, experimental realizations of active cholesterics and active smectics will emerge. The latest theoretical frameworks already invoke the HH mechanism to characterize lamellar distortions from active stresses (Whitfield *et al.*, 2017; Kole *et al.*, 2021). Furthermore, cholesteric liquid crystals remain widely employed in optical

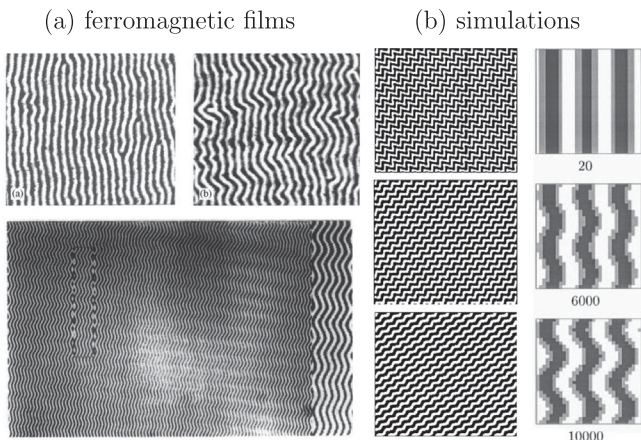


FIG. 36. (a) Micrographs of undulating magnetic domains under the influence of a cycled magnetic field (top two panels) and a temperature change (bottom panel). Changing the field or the temperature effectively dilates the magnetic stripe domains, inducing a HH-like instability. Top two panels from Demand *et al.*, 2002. Bottom panel from Seul and Wolfe, 1992. (b) Simulations of thin ferromagnetic films and two-dimensional block copolymers with an analogous free energy. Left three panels from Asciutto, Roland, and Sagui, 2005. Right three panels from Kodama and Doi, 1996.

and elastomeric materials. With undulations common in the dynamics of cholesterics, the HH mechanism has the potential to be leveraged for tunable properties in advanced technologies. Indeed, recent work has exploited the field-induced undulations of cholesterics to develop dynamic and switchable diffraction gratings and surface coatings (Ryabchun *et al.*, 2015, 2019; Ryabchun and Bobrovsky, 2018; Ryabchun, Lancia, and Katsonis, 2021). The HH mechanism is a generic but often overlooked method of pattern formation that has been and will continue to be integral to the structuring of periodic systems.

## ACKNOWLEDGMENTS

This work would not have been possible without Maurice Kleman's significant contributions to the field of liquid crystals. C. B. thanks Maurice Kleman for introducing him to this exciting area of research. We thank Kunyun He and Daeseok Kim for their micrographs and useful discussions. G. D. and T. L.-L. were supported by the French National Research Agency (JCJC Program, Grant No. 13-JS08-0006-01). T. L.-L. acknowledges funding from the French National Research Agency (AAPG Program, Grant No. 18-CE09-0028-02). L. T. and R. D. K. were supported in part by NSF Grants No. DMR-1262047 and No. DMR-1720530. This work was supported by a Simons Investigator grant from the Simons Foundation to R. D. K. L. T. acknowledges funding from the Simons Society of Fellows of the Simons Foundation (Grant No. 579910) and the European Commission Marie Curie Individual Fellowship project EXCHANGE\_inLCs (Grant No. 892354). M. O. L. acknowledges partial funding from the Neutron Sciences Directorate (Oak Ridge National Laboratory), sponsored by the U.S. Department of Energy, Office of Basic Energy Sciences.

## APPENDIX: SPHERICAL SMECTIC SHELLS: FURTHER DETAILS

In this appendix, we discuss a few additional points and provide further details on the geometrical and energetic properties of the smectic textures considered in Sec. VI.D.

### 1. Construction of the layers

In this section, we derive the parametrization of a smectic texture that is fully perpendicular to the inner and outer surfaces of the smectic shell in the plane  $\varphi = 0$ . In this plane, the geometry of the smectic layers have cross sections that are shown as blue regions or lines in Fig. 37. As illustrated in this sketch, the uniform thickness of the layers constrains the form of the orthonormal director  $\mathbf{n}_0$  defined at the points  $\mathbf{P}(r, \theta)$  of the region  $\mathcal{V}$  of the shell ( $R \leq r \leq R + h$ ,  $0 \leq \theta \leq \pi$ , and  $\varphi = 0$ , with the same notations as in Fig. 21):

$$\mathbf{n}_0(r, \theta) = \frac{R \cos \beta}{r} \hat{\mathbf{e}}_\theta + \sqrt{1 - \frac{R^2 \cos^2 \beta}{r^2}} \hat{\mathbf{e}}_\varphi. \quad (\text{A1})$$

The director  $\mathbf{n}_0$  at  $\varphi = 0$  also defines the field  $\mathbf{n}$  in a neighborhood since the normals of smectic layers are straight lines. This constructs a two-parameter family  $\mathcal{L}_{r, \theta}$  of lines

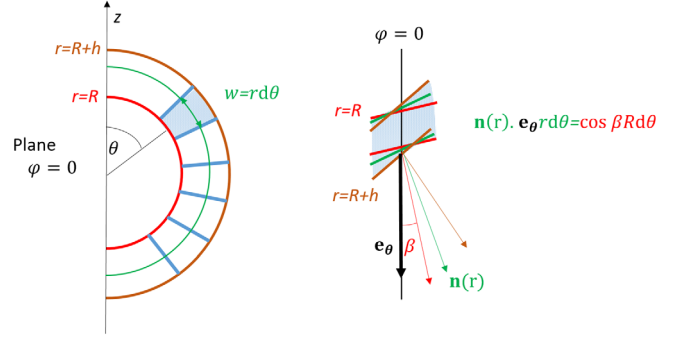


FIG. 37. Left graphic: cross section of a smectic shell in the plane  $\varphi = 0$ . We consider layers (in blue) that are perpendicular to the inner and outer spheres (located at  $r = R$  and  $r = R + h$ , respectively). The apparent thickness of the layers in plane  $w$  linearly increases with the radius  $r$ . Right graphic: because the actual thickness of the layers  $w \hat{\mathbf{e}}_\theta \cdot \mathbf{n}$  is uniform, this constrains the form of the director to Eq. (A1).

issued from the points  $\mathbf{P}(r, \theta)$  and of equations in Cartesian coordinates,

$$\begin{aligned} X_{r, \theta}(k) &= r \sin \theta + k \frac{R \cos \beta}{r} \cos \theta, \\ Y_{r, \theta}(k) &= k \sqrt{1 - \frac{R^2 \cos^2 \beta}{r^2}}, \\ Z_{r, \theta}(k) &= r \cos \theta - k \frac{R \cos \beta}{r} \sin \theta, \end{aligned} \quad (\text{A2})$$

where  $k \in \mathbb{R}$ , which can be used to parametrize the region around  $\varphi = 0$ .

The straight lines of the family  $\mathcal{L}_{r, \theta}$  are the normals of a one-parameter family  $\mathcal{S}_{\theta_0}$  of parallel surfaces that can be written as

$$\begin{aligned} X_{\theta_0}(r, \theta) &= r \sin \theta + \frac{R^2 \cos^2 \beta}{r} (\theta_0 - \theta) \cos \theta, \\ Y_{\theta_0}(r, \theta) &= R \cos \beta (\theta_0 - \theta) \sqrt{1 - \frac{R^2 \cos^2 \beta}{r^2}}, \\ Z_{\theta_0}(r, \theta) &= r \cos \theta - \frac{R^2 \cos^2 \beta}{r} (\theta_0 - \theta) \sin \theta. \end{aligned} \quad (\text{A3})$$

Each surface is indexed by  $\theta_0$ , which is also the zenithal angle at which each surface intersects  $\mathcal{V}$  (the blue lines in Fig. 37). It is straightforward to verify that the normals of these surfaces are indeed given by the director field  $\mathbf{n}$  and that the equations can be obtained by considering the surfaces as level sets of  $\Psi = \theta R \cos \beta + k$  in the parametrization of Eq. (A2).

### 2. Extension of the smectic texture along the azimuthal direction

When two straight lines of  $\mathcal{L}_{r, \theta}$  intersect, the director is not defined (i.e., defects are present). When  $\beta = 0$ , defects are already present at  $\mathcal{V}$  since the lines issued from the points  $\mathbf{P}(R, \theta)$  are all contained in  $\mathcal{V}$  (which is not compatible with the definition of  $\mathbf{n}_0$  when  $r > R$ ). On the other hand, when  $\beta \neq 0$  this is not the case, and a smectic region around  $\varphi = 0$  is

well defined and devoid of defects. How far can this defectless region extend? For this, we consider a point  $\mathbf{M}$  of the shell of coordinates  $X$ ,  $Y$ , and  $Z$  and of radial distance  $H = \sqrt{X^2 + Y^2 + Z^2}$  with  $R \leq H \leq R + h$ , and we look for the lines of  $\mathcal{L}_{r,\theta}$  to which it belongs. Equation (A2) gives

$$\begin{aligned} r^2 + k^2 &= X^2 + Y^2 + Z^2, \\ k &= Y / \sqrt{1 - \frac{R^2 \cos^2 \beta}{r^2}}, \\ Z &= r \cos \theta - k \frac{R \cos \beta}{r} \sin \theta. \end{aligned} \quad (\text{A4})$$

This yields the quadratic equation (in  $r^2$ )

$$r^4 - (X^2 + Z^2 + \cos^2 \beta R^2) r^2 + \cos^2 \beta R^2 H^2 = 0, \quad (\text{A5})$$

which gives two distinct solutions  $r_{\pm}$  when the discriminant  $\Delta = (X^2 + Z^2 + \cos^2 \beta R^2)^2 - 4 \cos^2 \beta R^2 H^2$  is positive. However, it is only when both solutions are in  $[R, R + h]$  that two actual lines issued from the two points  $\mathbf{P}(r_+, \theta_+)$  and  $\mathbf{P}(r_-, \theta_-)$  intersect at  $\mathbf{M}$ .

For simplicity and without losing generality, we consider from now on points located at  $Z = 0$ , where  $X = H \cos \varphi$  and  $Y = H \sin \varphi$ . When  $\varphi$  is small, only the largest value  $r_+$  is in  $[R, R + h]$ , which defines the director at  $\mathbf{M}$ . For example, for  $\varphi = 0$  we find  $\Delta = (H^2 - \cos^2 \beta R^2)^2$ , the trivial value  $r_+ = H$ , and the other value  $r_- = R \cos \beta$ , which is strictly less than  $R$ . On the other hand, these solutions no longer hold when  $\varphi$  is large, above some critical value: two lines emanating from different points of  $\mathcal{V}$  can intersect at  $\mathbf{M}$ . The smallest value of  $\varphi$ , i.e.,  $\varphi_c$ , where this situation occurs corresponds to the limiting case of a double root ( $\Delta = 0$ ) with  $r_+ = r_- = R$ . Equation (A4) then yields

$$\begin{aligned} \frac{H}{R} &= \frac{1}{\cos \beta}, \\ \sin \varphi_c &= \sin^2 \beta. \end{aligned} \quad (\text{A6})$$

The smectic texture originating from Eq. (A1), therefore, shows some prohibitive defects beyond  $\varphi_c$  in thick shells, and

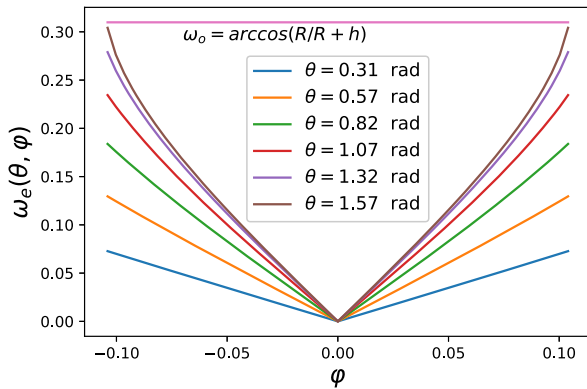


FIG. 38. Computation of the tilt angle  $\omega_e(\theta, \varphi)$  of the layers at the external sphere of a shell (inner radius  $R = 100 \mu\text{m}$ , thickness  $h = 5 \mu\text{m}$ , and  $\beta = 20^\circ$ ) near  $\varphi = 0$ . The tilt angle  $\omega_0$  of the rotationally invariant texture is also given for comparison. See the main text for additional context.

$\varphi_c$  is an upper bound value for the parameter  $\chi$  (which defines the size of the crescent domains). The presence of  $\Pi_\chi$  walls is energetically costly, but such a texture greatly decreases the tilt angle  $\omega_e$  of the smectic layers at the outer sphere of the shell; see Fig. 38.

Finally, note that if the straight lines of  $\mathcal{L}_{r,\theta}$  issued from  $\mathbf{n}_0$  are sufficient to compute  $\omega_e$  everywhere, they span only the upper part of the shell when departing from  $\varphi = 0$  (since  $H^2 = r^2 + k^2$  [Eq. (A4)] and  $r \geq R$ ). However, the director in the lower region of the shell is also imposed by  $\mathbf{n}_0(r = R, \theta)$  when the condition that the smectic layers must be perpendicular to the inner spherical shell surface is maintained. Geodesics on a sphere indeed play the same role for the inner surface as straight lines in Euclidean space. The director then has to lie on the great circles issued from  $\mathbf{n}_0(R, \theta)$ ; see Fig. 39. Thus completed, the director field  $\mathbf{n}(r, \theta, \varphi)$  and the corresponding smectic layers can be computed everywhere in

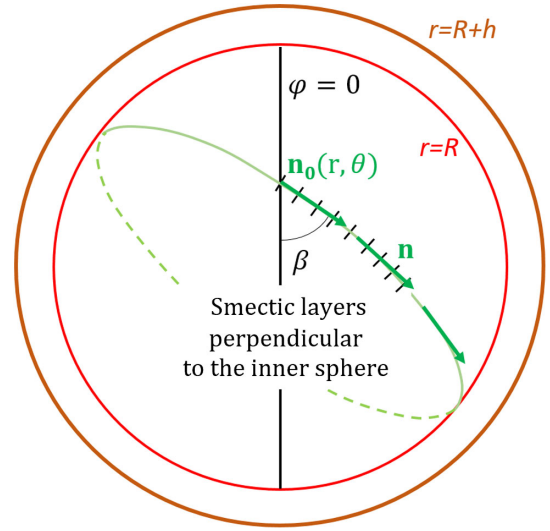


FIG. 39. Smectic layers perpendicular to the inner sphere define 2D smectic bands on this surface. The director has to follow the geodesics of the sphere (i.e., great circles).

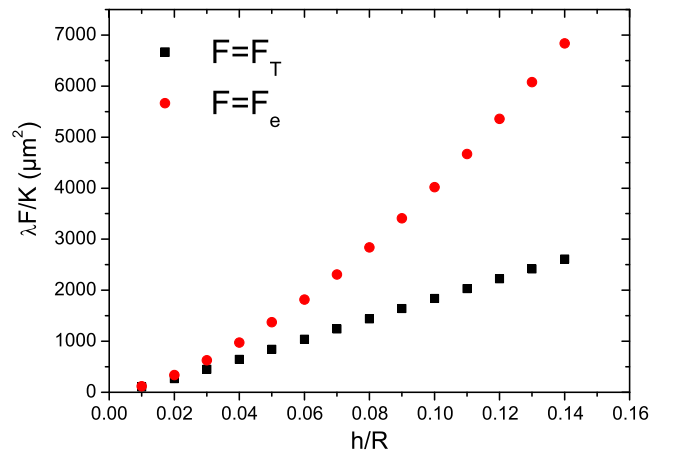


FIG. 40. Comparison of the energy  $F_e$  of the rotationally invariant texture [see Eq. (24)] with the minimization of the energy  $F_T$  for a shell of inner radius  $R = 100 \mu\text{m}$  and increasing thickness  $h$ .

the shell for a given pair of values  $(\beta, \chi)$ . The tilt angles of the layers  $\omega_e(\theta, \varphi)$  and  $\omega_\chi(r, \theta)$  are respectively obtained from

$$\begin{aligned}\sin \omega_e(\theta, \varphi) &= |\mathbf{n}(r = R + h, \theta, \varphi) \cdot \hat{\mathbf{e}}_r|, \\ \sin \omega_\chi(r, \theta) &= |\mathbf{n}(r, \theta, \varphi = \chi) \cdot \hat{\mathbf{e}}_\varphi|,\end{aligned}\quad (\text{A7})$$

and the total energy  $F_T(\beta, \chi)$  is obtained by integrating  $f_e = K\omega_e^3/3\lambda$  on the outer sphere and  $f_\chi = 2K\omega_\chi^3/3\lambda$  at the  $\Pi_\chi$  walls. Figure 40 shows that the minimized value of this energy is much smaller than the energy  $F_e$  of the rotationally invariant shell [Eq. (24)]. The corresponding  $(\beta, \chi)$  parameters are given in Fig. 22(d).

## REFERENCES

- Adlem, K., M. Čopič, G. R. Luckhurst, A. Mertelj, O. Parri, R. M. Richardson, B. D. Snow, B. A. Timimi, R. P. Tuffin, and D. Wilkes, 2013, *Phys. Rev. E* **88**, 022503.
- Agez, G., R. Bitar, and M. Mitov, 2011, *Soft Matter* **7**, 2841.
- Aharoni, H., D. V. Todorova, O. Albarrán, L. Goehring, R. D. Kamien, and E. Katifori, 2017, *Nat. Commun.* **8**, 15809.
- Andelman, D., and R. E. Rosensweig, 2009, *J. Phys. Chem. B* **113**, 3785.
- Anderson, P. W., 2005, Ed., *A Career in Theoretical Physics*, 2nd ed., World Scientific Series in 20th Century Physics Vol. 7 (World Scientific, Hackensack, NJ), pp. 543–553.
- Asciutto, E., C. Roland, and C. Sagui, 2005, *Phys. Rev. E* **72**, 021504.
- Ball, J. M., R. D. James, and F. T. Smith, 1992, *Phil. Trans. R. Soc. A* **338**, 389.
- Barbero, G., and I. Lelidis, 2015, *Liq. Cryst.* **42**, 1370.
- Bartolino, R., and G. Durand, 1977a, *Mol. Cryst. Liq. Cryst.* **40**, 117.
- Bartolino, R., and G. Durand, 1977b, *Phys. Rev. Lett.* **39**, 1346.
- Bates, F. S., and G. H. Fredrickson, 1990, *Annu. Rev. Phys. Chem.* **41**, 525.
- Bates, M. A., 2008, *J. Chem. Phys.* **128**, 104707.
- Beliaev, M., D. Zöllner, A. Pacureanu, P. Zaslansky, and I. Zlotnikov, 2021, *Nat. Phys.* **17**, 410.
- Beller, D. A., T. Machon, S. Čopar, D. M. Sussman, G. P. Alexander, R. D. Kamien, and R. A. Mosna, 2014, *Phys. Rev. X* **4**, 031050.
- Bevilacqua, G., and G. Napoli, 2005, *Phys. Rev. E* **72**, 041708.
- Bidaux, R., N. Boccarda, G. Sarma, L. De Seze, P.-G. de Gennes, and O. Parodi, 1973, *J. Phys. (Paris)* **34**, 661.
- Blanc, C., 2001, *Phys. Rev. E* **64**, 011702.
- Blanc, C., and M. Kleman, 1999, *Eur. Phys. J. B* **10**, 53.
- Blanc, C., and M. Kleman, 2001, *Eur. Phys. J. E* **4**, 241.
- Blanc, C., N. Zuodar, I. Lelidis, M. Kleman, and J.-L. Martin, 2004, *Phys. Rev. E* **69**, 011705.
- Borshch, V., *et al.*, 2013, *Nat. Commun.* **4**, 2635.
- Bouligand, Y., 1972a, *J. Phys. (Paris)* **33**, 525.
- Bouligand, Y., 1972b, *Tissue Cell* **4**, 189.
- Bouligand, Y., and F. Livolant, 1984, *J. Phys. (Paris)* **45**, 1899.
- Bouligand, Y., M. O. Soyer, and S. Puiseux-Dao, 1968, *Chromosoma* **24**, 251.
- Bradshaw, M., E. Raynes, J. Bunning, and T. Faber, 1985, *J. Phys. (Paris)* **46**, 1513.
- Brake, J. M., and N. L. Abbott, 2002, *Langmuir* **18**, 6101.
- Brake, J. M., A. D. Mezera, and N. L. Abbott, 2003a, *Langmuir* **19**, 8629.
- Brake, J. M., A. D. Mezera, and N. L. Abbott, 2003b, *Langmuir* **19**, 6436.
- Brand, H. R., and H. Pleiner, 1981, *J. Phys. (Paris), Lett.* **42**, 327.
- Brazovskii, S. A., 1975, *Sov. Phys. JETP* **41**, 85, [https://www.researchgate.net/publication/253018601\\_Phase\\_Transition\\_of\\_an\\_Isotropic\\_System\\_to\\_a\\_Nonuniform\\_State\\_-\\_JETP\\_41\\_85\\_1975](https://www.researchgate.net/publication/253018601_Phase_Transition_of_an_Isotropic_System_to_a_Nonuniform_State_-_JETP_41_85_1975).
- Brouwer, L. E. J., 1911, *Math. Ann.* **71**, 97.
- Bruss, I. R., and G. M. Grason, 2018, *Phys. Rev. X* **8**, 031046.
- Bukusoglu, E., M. Bedolla Pantoja, P. C. Mushenheim, X. Wang, and N. L. Abbott, 2016, *Annu. Rev. Chem. Biomol. Eng.* **7**, 163.
- Cagnon, M., M. Gharbia, and G. Durand, 1984, *Phys. Rev. Lett.* **53**, 938.
- Capasso, V., 2018, *An Introduction to Random Currents and Their Applications* Springer Briefs in Mathematics (Springer International Publishing, Cham, Switzerland), pp. 3–19.
- Carlton, R. J., J. T. Hunter, D. S. Miller, R. Abbasi, P. C. Mushenheim, L. N. Tan, and N. L. Abbott, 2013, *Liq. Cryst. Rev.* **1**, 29.
- Carlton, R. J., C. D. Ma, J. K. Gupta, and N. L. Abbott, 2012, *Langmuir* **28**, 12796.
- Cerda, E., and L. Mahadevan, 2003, *Phys. Rev. Lett.* **90**, 074302.
- Cestari, M., *et al.*, 2011, *Phys. Rev. E* **84**, 031704.
- Cha, Y. J., and D. K. Yoon, 2017, *Adv. Mater.* **29**, 1604247.
- Chaikin, P. M., and T. C. Lubensky, 1995, *Principles of Condensed Matter Physics* (Cambridge University Press, Cambridge, England).
- Challa, P. K., V. Borshch, O. Parri, C. T. Imrie, S. N. Sprunt, J. T. Gleeson, O. D. Lavrentovich, and A. Jákli, 2014, *Phys. Rev. E* **89**, 060501(R).
- Chan, C. L. C., M. M. Bay, G. Jacucci, R. Vadrucchi, C. A. Williams, G. T. van de Kerkhof, R. M. Parker, K. Vynck, B. Frka-Petesic, and S. Vignolini, 2019, *Adv. Mater.* **31**, 1905151.
- Chatterjee, S., and S. L. Anna, 2012, *Phys. Rev. E* **85**, 011701.
- Chiappini, M., and M. Dijkstra, 2021, *Nat. Commun.* **12**, 2157.
- Chu, G., R. Vilensky, G. Vasilyev, P. Martin, R. Zhang, and E. Zussman, 2018, *J. Phys. Chem. Lett.* **9**, 1845.
- Clark, N. A., and A. Hurd, 1982, *J. Phys. (Paris)* **43**, 1159.
- Clark, N. A., and R. B. Meyer, 1973, *Appl. Phys. Lett.* **22**, 493.
- Clark, N. A., and P. S. Pershan, 1973, *Phys. Rev. Lett.* **30**, 3.
- Cohen, Y., R. J. Albalak, B. J. Dair, M. S. Capel, and E. L. Thomas, 2000, *Macromolecules* **33**, 6502.
- Conradi, M., P. Zihlerl, A. Šarlah, and I. Mušević, 2006, *Eur. Phys. J. E* **20**, 231.
- Crawford, G. P., and S. Zumer, 1996, *Liquid Crystals in Complex Geometries: Formed by Polymer and Porous Networks* (CRC Press, Boca Raton).
- Darmon, A., M. Benzaquen, S. Čopar, O. Dauchot, and T. Lopez-Leon, 2016, *Soft Matter* **12**, 9280.
- Darmon, A., M. Benzaquen, D. Seč, S. Čopar, O. Dauchot, and T. Lopez-Leon, 2016, *Proc. Natl. Acad. Sci. U.S.A.* **113**, 9469.
- Darmon, A., O. Dauchot, T. Lopez-Leon, and M. Benzaquen, 2016, *Phys. Rev. E* **94**, 062701.
- Davidson, Z. S., Y. Huang, A. Gross, A. Martinez, T. Still, C. Zhou, P. J. Collings, R. D. Kamien, and A. G. Yodh, 2017, *Nat. Commun.* **8**, 15642.
- de Gennes, P.-G., and P. Pincus, 1976, *J. Phys. (Paris)* **37**, 1359.
- de Gennes, P.-G., and J. Prost, 1993, *The Physics of Liquid Crystals* (Clarendon Press, Oxford).
- Delabre, U., C. Richard, G. Guéna, J. Meunier, and A.-M. Cazabat, 2008, *Langmuir* **24**, 3998.
- Delage, M., R. Ribotta, and G. Durand, 1973, *Phys. Lett.* **44A**, 139.
- Delrieu, J. M., 1974, *J. Chem. Phys.* **60**, 1081.
- Demand, M., S. Padovani, M. Hehn, K. Ounadjela, and J. Bucher, 2002, *J. Magn. Mater.* **247**, 147.
- Diat, O., D. Roux, and F. Nallet, 1993, *J. Phys. II (France)* **3**, 1427.

- DiDonna, B. A., and R. D. Kamien, 2003, *Phys. Rev. E* **68**, 041703.
- Doane, J. W., 1990, in *Liquid Crystals: Applications and Uses*, Vol. 1, edited by B. Bahadur (World Scientific, Singapore), p. 361.
- Doane, J. W., 1991, *MRS Bull.* **16**, 22.
- Dogishi, Y., Y. Sakai, W. Y. Sohn, and K. Katayama, 2018, *Soft Matter* **14**, 8085.
- Drzaic, P. S., and T. J. Scheffer, 1997, *J. Soc. Inf. Disp.* **5**, 413.
- Durey, G., Y. Ishii, and T. Lopez-Leon, 2020, *Langmuir* **36**, 9368.
- Durey, G., H. R. O. Sohn, P. J. Ackerman, E. Brasselet, I. I. Smalyukh, and T. Lopez-Leon, 2020, *Soft Matter* **16**, 2669.
- Faetti, S., and V. Palleschi, 1984, *Phys. Rev. A* **30**, 3241.
- Fernandez-Nieves, A., V. Vitelli, A. S. Utada, D. R. Link, M. Márquez, D. R. Nelson, and D. A. Weitz, 2007, *Phys. Rev. Lett.* **99**, 157801.
- Fernández-Rico, C., M. Chiappini, T. Yanagishima, H. de Sousa, D. G. A. L. Aarts, M. Dijkstra, and R. P. A. Dullens, 2020, *Science* **369**, 950.
- Fournier, J.-B., and G. Durand, 1991, *J. Phys. II (France)* **1**, 845.
- Frank, F. C., 1958, *Discuss. Faraday Soc.* **25**, 19.
- Frank, F. C., and J. S. Kasper, 1958, *Acta Crystallogr.* **11**, 184.
- Fredrickson, G. H., and E. Helfand, 1987, *J. Chem. Phys.* **87**, 697.
- Friedel, G., 1922, *Ann. Phys. (Paris)* **9**, 273.
- Friedel, G., and F. Grandjean, 1910, *Bull. Soc. Fr. Mineral.* **33**, 409.
- Friedel, J., and M. Kleman, 1970, in *Fundamental Aspects of Dislocation Theory*, edited by J. A. Simmons, R. de Wit, and R. Bullough (National Bureau of Standards, Gaithersburg, MD), pp. 607–636.
- Frka-Petescic, B., G. Guidetti, G. Kamita, and S. Vignolini, 2017, *Adv. Mater.* **29**, 1701469.
- Fukuda, J.-i., and A. Onuki, 1995, *J. Phys. II (France)* **5**, 1107.
- Gerritsma, C. J., and P. Van Zanten, 1971a, *Mol. Cryst. Liq. Cryst.* **15**, 257.
- Gerritsma, C. J., and P. Van Zanten, 1971b, *Phys. Lett.* **37A**, 47.
- Gharbi, M. A., D. A. Beller, N. Sharifi-Mood, R. Gupta, R. D. Kamien, S. Yang, and K. J. Stebe, 2018, *Langmuir* **34**, 2006.
- Gharbia, M., M. Cagnon, and G. Durand, 1985, *J. Phys. (Paris)*, Lett. **46**, 683.
- Giraud-Guille, M.-M., 1998, *Curr. Opin. Solid State Mater. Sci.* **3**, 221.
- Gompper, G., and S. Klein, 1992, *J. Phys. II (France)* **2**, 1725.
- Gulik-Krzywicki, T., J. C. Dedieu, D. Roux, C. Degert, and R. Laversanne, 1996, *Langmuir* **12**, 4668.
- Gupta, V. K., and N. L. Abbott, 1997, *Science* **276**, 1533.
- Hamley, I. W., 1994, *Phys. Rev. E* **50**, 2872.
- Harth, K., and R. Stannarius, 2009, *Eur. Phys. J. E* **28**, 265.
- Helfrich, W., 1969, *J. Chem. Phys.* **51**, 4092.
- Helfrich, W., 1970, *Appl. Phys. Lett.* **17**, 531.
- Helfrich, W., 1971, *J. Chem. Phys.* **55**, 839.
- Hervet, H., J. P. Hurault, and F. Rondelez, 1973, *Phys. Rev. A* **8**, 3055.
- Hopf, H., 1927, *Math. Ann.* **96**, 225.
- Hurault, J. P., 1973, *J. Chem. Phys.* **59**, 2068.
- Ishikawa, T., and O. D. Lavrentovich, 2001a, in *Defects in Liquid Crystals: Computer Simulations, Theory and Experiments*, NATO Science Series II: Mathematics, Physics and Chemistry Vol. 43, edited by O. D. Lavrentovich, P. Pasini, C. Zannoni, and S. Žumer (Springer, New York), p. 271.
- Ishikawa, T., and O. D. Lavrentovich, 2001b, *Phys. Rev. E* **63**, 030501.
- Jákli, A., O. D. Lavrentovich, and J. V. Selinger, 2018, *Rev. Mod. Phys.* **90**, 045004.
- Kamien, R. D., 2002, *Rev. Mod. Phys.* **74**, 953.
- Kamien, R. D., and T. C. Lubensky, 1999, *Phys. Rev. Lett.* **82**, 2892.
- Kamien, R. D., D. R. Nelson, C. D. Santangelo, and V. Vitelli, 2009, *Phys. Rev. E* **80**, 051703.
- Kawasaki, K., and T. Kawakatsu, 1990, *Macromolecules* **23**, 4006.
- Kaznatcheev, K. V., P. Dudin, O. D. Lavrentovich, and A. P. Hitchcock, 2007, *Phys. Rev. E* **76**, 061703.
- Kim, J.-W., H. Kim, M. Lee, and J. J. Magda, 2004, *Langmuir* **20**, 8110.
- King, H., R. D. Schroll, B. Davidovitch, and N. Menon, 2012, *Proc. Natl. Acad. Sci. U.S.A.* **109**, 9716.
- Kleman, M., 1989, *Adv. Phys.* **38**, 605.
- Kleman, M., and O. D. Lavrentovich, 2004, *Soft Matter Physics: An Introduction* (Springer, New York).
- Kleman, M., and O. Parodi, 1975, *J. Phys. (Paris)* **36**, 671.
- Kleman, M., and J. F. Sadoc, 1979, *J. Phys. (Paris)*, Lett. **40**, 569.
- Kodama, H., and M. Doi, 1996, *Macromolecules* **29**, 2652.
- Kole, S. J., G. P. Alexander, S. Ramaswamy, and A. Maitra, 2021, *Phys. Rev. Lett.* **126**, 248001.
- Koning, V., T. Lopez-Leon, A. Darmon, A. Fernandez-Nieves, and V. Vitelli, 2016, *Phys. Rev. E* **94**, 012703.
- Koning, V., T. Lopez-Leon, A. Fernandez-Nieves, and V. Vitelli, 2013, *Soft Matter* **9**, 4993.
- Kwon, J.-Y., M. Khan, and S.-Y. Park, 2016, *RSC Adv.* **6**, 55976.
- Lagerwall, J. P. F., C. Schütz, M. Salajkova, J. Noh, J. Hyun Park, G. Scalia, and L. Bergström, 2014, *NPG Asia Mater.* **6**, e80.
- Larson, R. G., 2017, *Nature (London)* **550**, 466.
- Lavrentovich, M. O., and L. Tran, 2020, *Phys. Rev. Res.* **2**, 023128.
- Lavrentovich, O. D., 1998, *Liq. Cryst.* **24**, 117.
- Lee, B.-w., and N. A. Clark, 2001, *Science* **291**, 2576.
- Liang, H.-L., J. Noh, R. Zentel, P. Rudquist, and J. P. F. Lagerwall, 2013, *Phil. Trans. R. Soc. A* **371**, 20120258.
- Liang, H.-L., S. Schymura, P. Rudquist, and J. P. F. Lagerwall, 2011, *Phys. Rev. Lett.* **106**, 247801.
- Liang, H.-L., R. Zentel, P. Rudquist, and J. P. F. Lagerwall, 2012, *Soft Matter* **8**, 5443.
- Liarte, D. B., M. Bierbaum, R. A. Mosna, R. D. Kamien, and J. P. Sethna, 2016, *Phys. Rev. Lett.* **116**, 147802.
- Liedel, C., C. Lewin, L. Tsarkova, and A. Böker, 2015, *Small* **11**, 6058.
- Livolant, F., and Y. Bouligand, 1986, *J. Phys. (Paris)* **47**, 1813.
- Livolant, F., and A. Leforestier, 1996, *Prog. Polym. Sci.* **21**, 1115.
- Livolant, F., A. M. Levelut, J. Doucet, and J. P. Benoit, 1989, *Nature (London)* **339**, 724.
- Lockwood, N. A., J. K. Gupta, and N. L. Abbott, 2008, *Surf. Sci. Rep.* **63**, 255.
- Lopez-Leon, T., M. A. Bates, and A. Fernandez-Nieves, 2012, *Phys. Rev. E* **86**, 030702.
- Lopez-Leon, T., and A. Fernandez-Nieves, 2009, *Phys. Rev. E* **79**, 021707.
- Lopez-Leon, T., and A. Fernandez-Nieves, 2011, *Colloid Polym. Sci.* **289**, 345.
- Lopez-Leon, T., A. Fernandez-Nieves, M. Nobili, and C. Blanc, 2011, *Phys. Rev. Lett.* **106**, 247802.
- Lopez-Leon, T., A. Fernandez-Nieves, M. Nobili, and C. Blanc, 2012, *J. Phys. Condens. Matter* **24**, 284122.
- Lopez-Leon, T., V. Koning, K. B. S. Devaiah, V. Vitelli, and A. Fernandez-Nieves, 2011, *Nat. Phys.* **7**, 391.
- Loudet, J.-C., P. V. Dolganov, P. Patrício, H. Saadaoui, and P. Cluzeau, 2011, *Phys. Rev. Lett.* **106**, 117802.
- Lydon, J., 2010, *J. Mater. Chem.* **20**, 10071.
- Machon, T., 2017, *New J. Phys.* **19**, 113030.
- MacKintosh, F. C., 1994, *Phys. Rev. E* **50**, 2891.
- Mai, Y., and A. Eisenberg, 2012, *Chem. Soc. Rev.* **41**, 5969.

- Mandle, R. J., 2016, *Soft Matter* **12**, 7883.
- Manyuhina, O. V., and M. Ben Amar, 2013, *Phys. Lett. A* **377**, 1003.
- Manyuhina, O. V., and M. J. Bowick, 2015, *Int. J. Nonlinear Mech.* **75**, 87.
- Manyuhina, O. V., A.-M. Cazabat, and M. Ben Amar, 2010, *Europhys. Lett.* **92**, 16005.
- Marcus, M., 1981, *J. Phys. (Paris)* **42**, 61.
- Marlow, S., and P. Olmsted, 2002, *Eur. Phys. J. E* **8**, 485.
- Matsen, M. W., 2005, *Phys. Rev. Lett.* **95**, 258302.
- Matsen, M. W., 2006, *Soft Matter* **2**, 1048.
- Matsumoto, E. A., D. A. Vega, A. D. Pezzutti, N. A. García, P. M. Chaikin, and R. A. Register, 2015, *Proc. Natl. Acad. Sci. U.S.A.* **112**, 12639.
- Meister, R., H. Dumoulin, M.-A. Hallé, and P. Pieranski, 1996, *J. Phys. II (France)* **6**, 827.
- Meister, R., M.-A. Hallé, H. Dumoulin, and P. Pieranski, 1996, *Phys. Rev. E* **54**, 3771.
- Mermin, N. D., 1979, *Rev. Mod. Phys.* **51**, 591.
- Meyer, C., C. Blanc, G. R. Luckhurst, P. Davidson, and I. Dozov, 2020, *Sci. Adv.* **6**, eabb8212.
- Meyer, R. B., 1973, *Philos. Mag.* **27**, 405.
- Meyer, R. B., L. Liebert, L. Strzelecki, and P. Keller, 1975, *J. Phys. (Paris)*, *Lett.* **36**, 69.
- Meyer, R. B., and P. S. Pershan, 1973, *Solid State Commun.* **13**, 989.
- Mitov, M., 2017, *Soft Matter* **13**, 4176.
- Moradi, S., A. Nowroozi, and M. Shahlaci, 2019, *RSC Adv.* **9**, 7687.
- Mosseri, R., 2008, *C.R. Chim.* **11**, 192.
- Napoli, G., and A. Nobili, 2009, *Phys. Rev. E* **80**, 031710.
- Noh, J., K. Reguengo De Sousa, and J. P. F. Lagerwall, 2016, *Soft Matter* **12**, 367.
- Noh, J., Y. Wang, H.-L. Liang, V. S. R. Jampani, A. Majumdar, and J. P. F. Lagerwall, 2020, *Phys. Rev. Res.* **2**, 033160.
- Onuki, A., and J.-i. Fukuda, 1995, *Macromolecules* **28**, 8788.
- Orizaga, S., and K. Glasner, 2016, *Phys. Rev. E* **93**, 052504.
- Oswald, P., and S. Ben-Abraham, 1982, *J. Phys. (Paris)* **43**, 1193.
- Oswald, P., J. C. Géminard, L. Lejcek, and L. Sallen, 1996, *J. Phys. II (France)* **6**, 281.
- Oswald, P., and P. Pieranski, 2005, *Smectic and Columnar Liquid Crystals* (CRC Press, Boca Raton).
- Pardaev, S. A., *et al.*, 2016, *Soft Matter* **12**, 4472.
- Parker, R. M., B. Frka-Petesic, G. Guidetti, G. Kamita, G. Consani, C. Abell, and S. Vignolini, 2016, *ACS Nano* **10**, 8443.
- Parker, R. M., G. Guidetti, C. A. Williams, T. Zhao, A. Narkevicius, S. Vignolini, and B. Frka-Petesic, 2018, *Adv. Mater.* **30**, 1704477.
- Parker, R. M., T. H. Zhao, B. Frka-Petesic, and S. Vignolini, 2022, *Nat. Commun.* **13**, 3378.
- Paulsen, J. D., E. Hohlfield, H. King, J. Huang, Z. Qiu, T. P. Russell, N. Menon, D. Vella, and B. Davidovitch, 2016, *Proc. Natl. Acad. Sci. U.S.A.* **113**, 1144.
- Pereira, G. G., 2002, *J. Chem. Phys.* **117**, 1878.
- Poincaré, H., 1885, *J. Math. Pures Appl.* **1**, 167, <http://eudml.org/doc/235596>.
- Pommella, A., S. Caserta, and S. Guido, 2013, *Soft Matter* **9**, 7545.
- Poulin, P., and D. A. Weitz, 1998, *Phys. Rev. E* **57**, 626.
- Ramezani-Dakhel, H., M. Rahimi, J. Pendery, Y.-K. Kim, S. Thayumanavan, B. Roux, N. L. Abbott, and J. J. de Pablo, 2018, *ACS Appl. Mater. Interfaces* **10**, 37618.
- Ramos, L., P. Fabre, and L. Fruchter, 1999, *Eur. Phys. J. B* **8**, 67.
- Rapini, A., and M. Papoular, 1969, *J. Phys. (Paris)*, *Colloq.* **30**, C4.
- Rey, A. D., 2010, *Soft Matter* **6**, 3402.
- Rey, A. D., E. Herrera-Valencia, and Y. K. Murugesan, 2014, *Liq. Cryst.* **41**, 430.
- Ribotta, R., and G. Durand, 1977, *J. Phys. (Paris)* **38**, 179.
- Rofouie, P., D. Pasini, and A. D. Rey, 2015, *Soft Matter* **11**, 1127.
- Roland, J.-C., D. Reis, and B. Vian, 1992, *Tissue Cell* **24**, 335.
- Roman, M., and D. G. Gray, 2005, *Langmuir* **21**, 5555.
- Rondelez, F., and H. Arnould, 1971, *C.R. Seances Acad. Sci., Ser. B* **273**, 549.
- Rondelez, F., H. Arnould, and C. J. Gerritsma, 1972, *Phys. Rev. Lett.* **28**, 735.
- Rondelez, F., and J. Hulin, 1972, *Solid State Commun.* **10**, 1009.
- Rosenblatt, C. S., R. Pindak, N. A. Clark, and R. B. Meyer, 1977, *J. Phys. (Paris)* **38**, 1105.
- Ryabchun, A., and A. Bobrovsky, 2018, *Adv. Opt. Mater.* **6**, 1800335.
- Ryabchun, A., A. Bobrovsky, J. Stumpe, and V. Shibaev, 2015, *Adv. Opt. Mater.* **3**, 1462.
- Ryabchun, A., F. Lancia, and N. Katsonis, 2021, *ACS Appl. Mater. Interfaces* **13**, 4777.
- Ryabchun, A., D. Yakovlev, A. Bobrovsky, and N. Katsonis, 2019, *ACS Appl. Mater. Interfaces* **11**, 10895.
- Sadoc, J.-F., and R. Mosseri, 1999, *Geometrical Frustration* (Cambridge University Press, Cambridge, England).
- Sakai, Y., W. Y. Sohn, and K. Katayama, 2019, *Soft Matter* **15**, 7159.
- Santangelo, C. D., and P. Pincus, 2002, *Phys. Rev. E* **66**, 061501.
- Santangelo, C. D., V. Vitelli, R. D. Kamien, and D. R. Nelson, 2007, *Phys. Rev. Lett.* **99**, 017801.
- Saupe, A., 1969, *Mol. Cryst.* **7**, 59.
- Scheffer, T. J., 1972, *Phys. Rev. Lett.* **28**, 593.
- Seč, D., S. Čopar, and S. Žumer, 2014, *Nat. Commun.* **5**, 3057.
- Seč, D., T. Lopez-Leon, M. Nobili, C. Blanc, A. Fernandez-Nieves, M. Ravnik, and S. Žumer, 2012, *Phys. Rev. E* **86**, 020705.
- Seč, D., T. Porenta, M. Ravnik, and S. Žumer, 2012, *Soft Matter* **8**, 11982.
- Selmi, M., J.-C. Loudet, P. V. Dolganov, T. Othman, and P. Cluzeau, 2017, *Soft Matter* **13**, 3649.
- Senyuk, B., I. I. Smalyukh, and O. D. Lavrentovich, 2005, *Opt. Lett.* **30**, 349.
- Senyuk, B., I. I. Smalyukh, and O. D. Lavrentovich, 2006, *Phys. Rev. E* **74**, 011712.
- Sethna, J. P., D. C. Wright, and N. D. Mermin, 1983, *Phys. Rev. Lett.* **51**, 467.
- Seul, M., and D. Andelman, 1995, *Science* **267**, 476.
- Seul, M., and R. Wolfe, 1992, *Phys. Rev. A* **46**, 7519.
- Sharma, A., V. S. R. Jampani, and J. P. F. Lagerwall, 2019, *Langmuir* **35**, 11132.
- Sharma, A., and J. P. F. Lagerwall, 2018, *Liq. Cryst.* **45**, 2319.
- Sharma, V., M. Crne, J. O. Park, and M. Srinivasarao, 2009, *Science* **325**, 449–451.
- Shin, H., M. J. Bowick, and X. Xing, 2008, *Phys. Rev. Lett.* **101**, 037802.
- Sierro, P., and D. Roux, 1997, *Phys. Rev. Lett.* **78**, 1496.
- Silvestre, N. M., M. C. Figueirinhas Pereira, N. R. Bernardino, and M. M. Telo da Gama, 2016, *Eur. Phys. J. E* **39**, 13.
- Singer, S. J., 1993, *Phys. Rev. E* **48**, 2796.
- Singer, S. J., 2000, *Phys. Rev. E* **62**, 3736.
- Smalyukh, I. I., O. V. Zribi, J. C. Butler, O. D. Lavrentovich, and G. C. L. Wong, 2006, *Phys. Rev. Lett.* **96**, 177801.
- Sornette, D., 1987, *J. Phys. (Paris)* **48**, 151.
- Sparavigna, A., L. Komitov, O. D. Lavrentovich, and A. Strigazzi, 1992, *J. Phys. II (France)* **2**, 1881.
- Sparavigna, A., O. D. Lavrentovich, and A. Strigazzi, 1994, *Phys. Rev. E* **49**, 1344.

- Tortora, L., and O. D. Lavrentovich, 2011, *Proc. Natl. Acad. Sci. U.S.A.* **108**, 5163.
- Tovkach, O., J. Chen, M. M. Ripp, T. Zhang, J. D. Paulsen, and B. Davidovitch, 2020, *Proc. Natl. Acad. Sci. U.S.A.* **117**, 3938.
- Tran, L., and K. J. M. Bishop, 2020, *ACS Nano* **14**, 5459.
- Tran, L., H.-N. Kim, N. Li, S. Yang, K. J. Stebe, R. D. Kamien, and M. F. Haase, 2018, *Sci. Adv.* **4**, eaat8597.
- Tran, L., M. O. Lavrentovich, G. Durey, A. Darmon, M. F. Haase, N. Li, D. Lee, K. J. Stebe, R. D. Kamien, and T. Lopez-Leon, 2017, *Phys. Rev. X* **7**, 041029.
- Tsori, Y., and D. Andelman, 2008, *Macromolecules* **41**, 2968.
- Tu, F., and D. Lee, 2012, *Langmuir* **28**, 9944.
- Urbanski, M., C. G. Reyes, J. Noh, A. Sharma, Y. Geng, V. Subba Rao Jampani, and J. P. F. Lagerwall, 2017, *J. Phys. Condens. Matter* **29**, 133003.
- Utada, A. S., E. Lorenceau, D. R. Link, P. D. Kaplan, H. A. Stone, and D. A. Weitz, 2005, *Science* **308**, 537.
- Vitelli, V., and D. R. Nelson, 2006, *Phys. Rev. E* **74**, 021711.
- Volovik, G. E., and O. D. Lavrentovich, 1983, *Sov. Phys. JETP* **58**, 1159, <http://www.jetp.ras.ru/cgi-bin/e/index/e/58/6/p1159?a=list>.
- Wang, Z., 1994, *J. Chem. Phys.* **100**, 2298.
- Whitfield, C. A., T. C. Adhyapak, A. Tiribocchi, G. P. Alexander, D. Marenduzzo, and S. Ramaswamy, 2017, *Eur. Phys. J. E* **40**, 50.
- Williams, D. R. M., 1995, *Phys. Rev. Lett.* **75**, 453.
- Wright, D. C., and N. D. Mermin, 1989, *Rev. Mod. Phys.* **61**, 385.
- Xia, Y., and G. M. Whitesides, 1998, *Annu. Rev. Mater. Sci.* **28**, 153.
- Xu, T., A. V. Zvelindovsky, G. J. A. Sevink, K. S. Lyakhova, H. Jinnai, and T. P. Russell, 2005, *Macromolecules* **38**, 10788.
- Yada, M., J. Yamamoto, and H. Yokoyama, 2003, *Langmuir* **19**, 9613.
- Yu, M., H. Yang, and D.-K. Yang, 2017, *Soft Matter* **13**, 8728.
- Zhou, Y., A. Guo, R. Zhang, J. C. Armas-Perez, J. A. Martínez-González, M. Rahimi, M. Sadati, and J. J. de Pablo, 2016, *Soft Matter* **12**, 8983.
- Zilman, A., and R. Granek, 1999, *Eur. Phys. J. B* **11**, 593.
- Zipfel, J., F. Nettesheim, P. Lindner, T. D. Le, U. Olsson, and W. Richtering, 2001, *Europhys. Lett.* **53**, 335.